MODELING OF DISTRIBUTED FEEDBACK SEMICONDUCTOR LASERS

By

MENG-MU SHIH

A DISSERTATION PRESENTED TO THE GRADUATE SCHOOL
OF THE UNIVERSITY OF FLORIDA IN PARTIAL FULFILLMENT
OF THE REQUIREMENTS FOR THE DEGREE OF
DOCTOR OF PHILOSOPHY

UNIVERSITY OF FLORIDA
2010

To my parents Mr. Shi-Chen Shih and Mrs. Ai-Chiao Chen Shih and those who have helped me

ACKNOWLEDGMENTS

First and foremost, I sincerely appreciate my academic advisor, Prof. Peter Zory for his guidance and encouragement. His two classes of photonics and laser electronics initiated my strong interest and fundamental background for my Ph. D. dissertation. He provides the physics background with intuitive but deeper insights for my mathematical modeling. Dr. Zory is also my life mentor. His experiences in engineering and management in enterprises and academia has shaped into a unique life of philosophy. I have cultured from his unique advantages which have helped me to think and solve academic and life problems from multi-faceted perspectives. I really enjoy extensive and intensive discussions with Dr. Zory from research topics to life of philosophy, not only solving my problems wisely but also helping me explore views more. With his patient and enthusiastic efforts for improving both my written and oral communication skills, I can pass the oral exam and also optimistically face unexpected challenging life issues.

I would like to thank all the other members of my supervisory committee: Dr. Toshikazu Nishida, Dr. Huikai Xie, and Dr. Angela Lindner. Dr. Xie taught me the semiconductor physical electronics and provided many suggestions during my oral proposal based on his optics specialty. Dr. Nishida and Dr. Angela also provided substantial suggestions.

Some University of Florida staff have worked behind the scene. Dr. Linder, as Associate Dean of Students Affairs, helped me deal with life issues. Ms. Debra Anderson at International Center has provided extensive help far beyond that which I can express. Ms. Shannon Chillingworth, my departmental graduate advisor, has

directed me to follow requirement details. Mr. Keith Rambo provides labs and equipments.

I would like to thank Dr. Zory's previous students Dr. Horng-Jye Luo for his help in the Chapter 3 of my dissertation. His mathematical modeling and manipulation techniques inspired my desire for further modeling process. I also thank colleagues from Interdisciplinary Microsystems Group: Dr. Lei Wu and Sean under Dr. Xie. They helped me conduct experiments on semiconductor lasers and quantum cascade lasers. This work was partly funded by the Defense Advanced Research Projects Agency (DARPA contract no. 00062850) conducted by Dr. Dan Botez in University of Wisconsin.

Friends from different countries have enriched my life in this college town. I have priceless opportunities to interact with people from different cultures. Through them, I comprehend the world of diversity. Dr. Wang, my high school classmate, has encouraged me since my graduate study in the U.S although he has been quite busy in performing long-hour surgeries. Dr. Along and Dr. Shiau provide me with good suggestions about doing research. Mr. Chu provides friendly support. Mr. Ray, Mr. Justin and Mr. Toby often find interesting topics to broaden my view toward American culture. Last but definitely not the least, I want to thank my parents for their endless support and deepest love throughout the life journey, sometimes quite challenging to me. No matter where I would be, they would be with me.

TABLE OF CONTENTS

LIST OF TABLES

LIST OF FIGURES

Abstract of Dissertation Presented to the Graduate School
of the University of Florida in Partial Fulfillment of the
Requirements for the Degree of Doctor of Philosophy

MODELING OF DISTRUBUTED FEEDBACK SEMICONDUCTOR LASERS

By

Meng-Mu Shih

August 2010

Chair: Peter Zory
Major: Electrical and Computer Engineering

This work demonstrates the multi-parameter modeling processes of calculating coupling coefficients of the optical waveguide structures for various distributed feedback (DFB) semiconductor lasers. These lasers operate on Near/Mid-IR and TE/TM modes. Substrate-emitting DFB quantum cascade laser analyzed and performance improvement are discussed.

CHAPTER 1
INTRODUCTION

1.1 Study Motivation

Semiconductor lasers were first demonstrated in 1962 [1][2]. Since these devices have built-in p-n junctions, they are called diode lasers. In the 1960s and 1970s, most applications were defense-related, and only small volumes of diode lasers were required. They became high volume products in the 1980s and 1990s with the advent of application areas such as fiber-optic communications and information technology. In many of these application areas, the diode lasers used have built-in diffraction gratings that provide narrow-band spectral output. This type of diode laser is now called a distributed feedback (DFB) laser.

In 1994, a new type of semiconductor laser that did not have a built-in p-n junction was demonstrated [3]. These lasers, called Quantum Cascade Lasers (QCLs) operate on intersubband transitions and utilize electron tunneling to achieve population inversion in the conduction band of the semiconductor material. These QCLs are now starting to replace cryogenic diode lasers and gas lasers that have been used for many years in molecular spectroscopy applications in the mid to far infra-red region of the spectrum [4]. To date, the narrow-band spectral output required in such applications has been achieved using diffraction-grating techniques in resonator configurations external to the semiconductor laser chip. In order to reduce the cost of such systems, there has been considerable research activity in the last few years to develop QCLs with integrated diffraction gratings (DFB-QCLs). Since narrow-band operation can be achieved using first-order DFB, most of the research activity in this area has been concentrated on this type of DFB-QCL. In order to eliminate the expensive optics required to capture and

collimate the high divergence beams emitted from these first-order DFB-QCLs while retaining narrow-band output, a more complex design incorporating second-order DFB is now being researched [5].

1.2 Basic Semiconductor Laser Concepts

The multi-layer dielectric slab waveguide (WG) structure shown in Figure 1-1 (a) is the basic structure used for all semiconductor lasers (either diode or QCL). Current (I) through the laser chip produces optical gain in the active region. Cleaved facets on the longitudinal edges provide optical feedback. Figure 1-1 (b) shows a typical output power (P_0) vs. I diagram. When I is greater than the threshold current (I_{th}), laser action is initiated in the semiconductor chip.

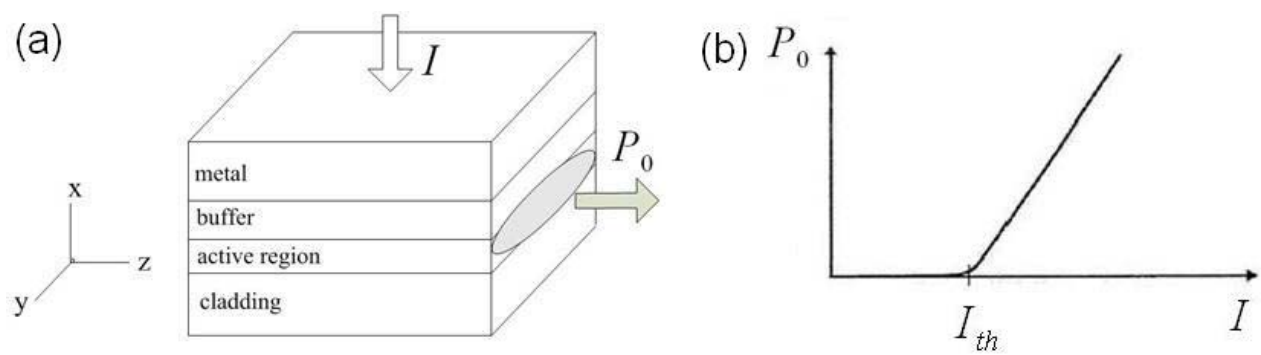

Figure 1-1. Semiconductor laser A) Schematic structure of semiconductor laser B) Power vs. current diagram

Figure 1-2 shows the schematic structure and energy-band diagram. If we rotate the laser chip shown in Figure 1-1 (a) clockwise by 90 degrees and expand the area in the vicinity of the active region, we see that current I is equivalent to electrons moving to the positive metal contact and the active region is a quantum well (QW) designed to trap electrons. In the energy band diagram, conduction band (CB) electrons (e^-) are trapped in the QW and recombine with valence band (VB) holes. During this process,

photons are produced with energy $h\nu = E_{C1} - E_{H1}$, where E_{C1} and E_{H1} represent certain energy states in the CB and VB, respectively. This process whereby electrons move from the CB to the VB is called an interband transition.

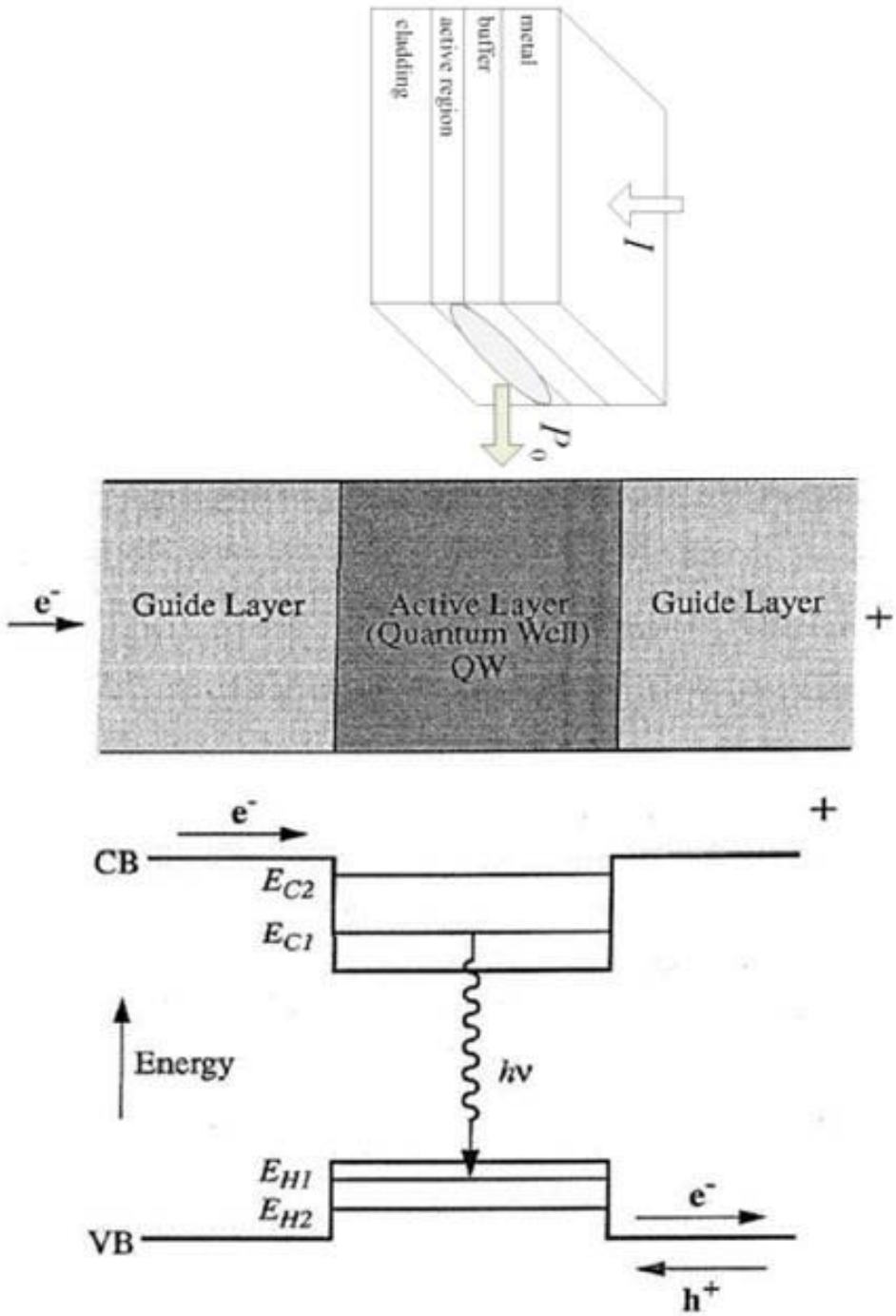

Figure 1-2. Structure and energy-band diagram of diode lasers

Figure 1-3 shows the schematic structure and energy-band diagram of the basic unit in a quantum cascade laser (QCL). In a typical QCL, there will be about 20 to 30 basic units in the active region. Electrons are attracted to the positive metal contact as in the diode case, but the basic process used here to achieve gain is quite different. Electrons in the CB states of the injector region tunnel into E_{C2} states in the QW. These electrons then make transitions to E_{C1} states in the QW and produce photons with energy $h\nu = E_{C2} - E_{C1}$. Since these transitions occur within the CB of the QW rather than between the CB and VB of the QW, they are called intersubband transitions.

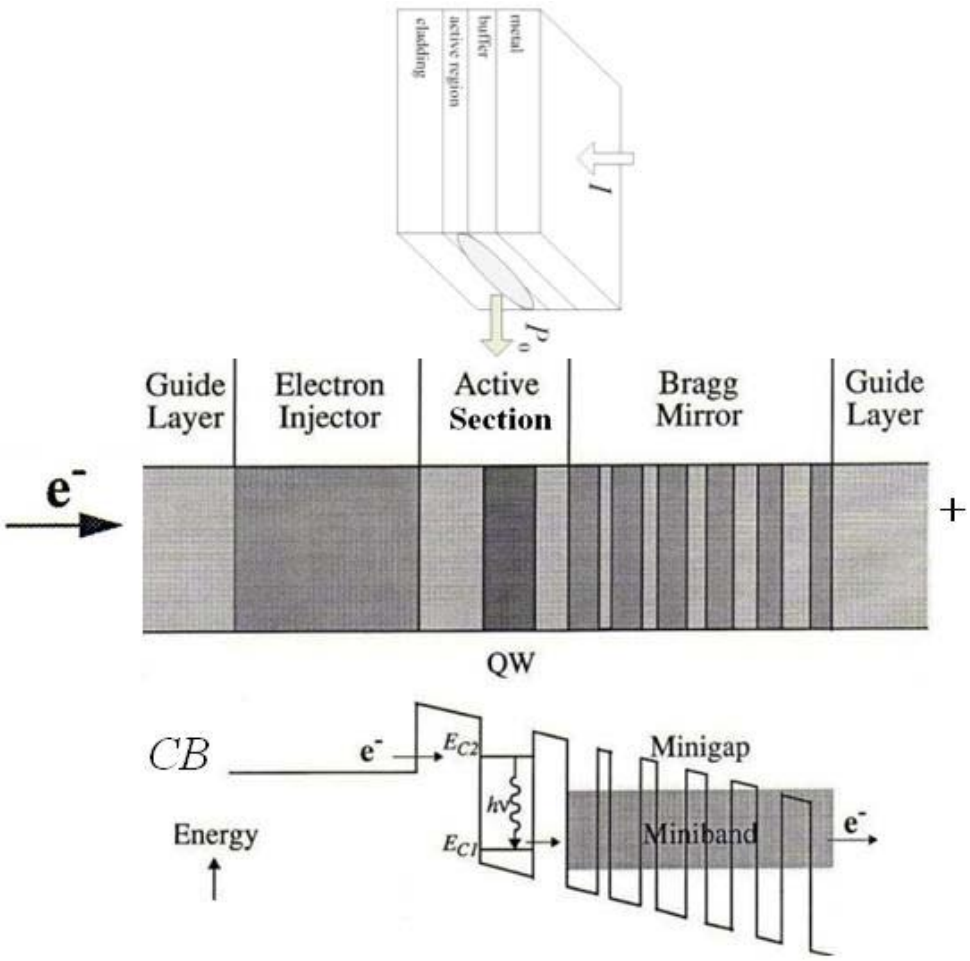

Figure 1-3. Structure and energy-band diagram of the basic unit in quantum cascade lasers

1.3 Thesis Problem Background

As discussed in Section 1.1, the method use to obtain narrow-band spectral width and low divergence beams from semiconductor lasers is to incorporate a diffraction grating into the multi-layered structure. A schematic diagram of this type of structure where the grating is defined by a corrugated metal/dielectric interface is shown in Figure 1-4.

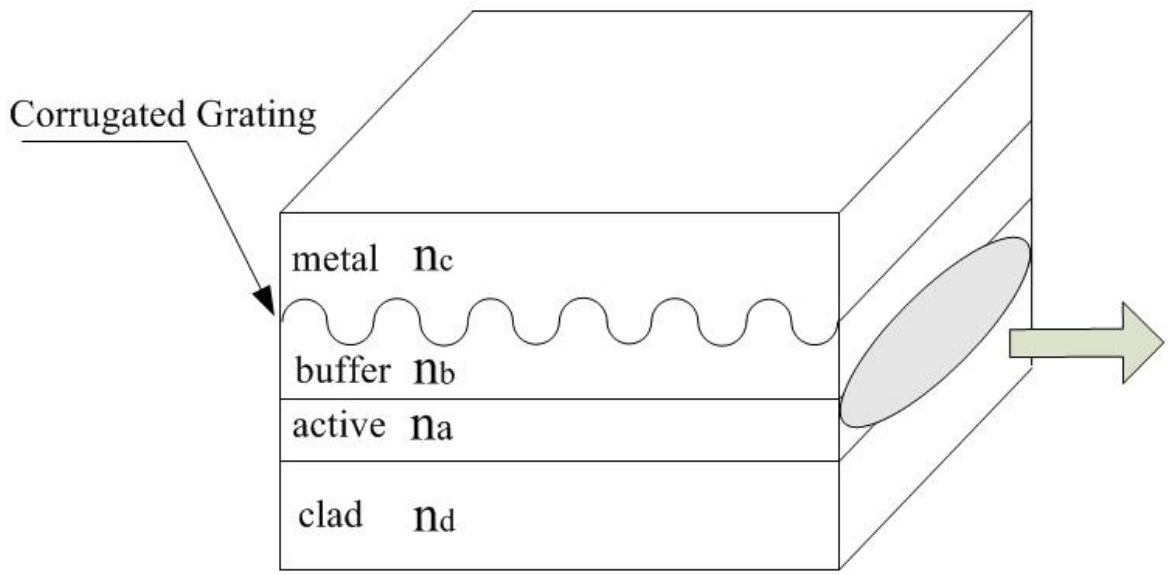

Figure 1-4. A schematic diagram of semiconductor waveguide with metal grating

If the corrugated waveguide shown in Figure 1-4 is designed correctly, light waves with a specific wavelength traveling to the right and left inside the guide will be coupled to each other by backward diffraction. This mechanism is called distributed feedback (DFB), and, if sufficient gain is provided to the light in the guide, laser action at that specific wavelength takes place. Two parameters associated with the metal layer that are required for low current density operation are the reflectivity of the metal at the lasing wavelength and the electrical resistance at the metal-dielectric interface. Reflectivity should be high in order to minimize absorption of the beam in the metal and

electrical resistance should be low in order to minimize heat due to electrical power dissipation. Since these two requirements are sometimes difficult to achieve with the same metal, the corrugation is often defined in the interior of the epitaxial structure where one obtains a dielectric/dielectric interface. In order to achieve this result, a complex epitaxial re-growth step is required after grating fabrication. This option has been successfully utilized in the production of first-order DFB diode lasers used in fiber-optic communication applications. The corrugation fabrication technique that will ultimately be used in the production of DFB-QCLs has yet to be decided.

For first-order DFB operation, the grating period must be about 1/6 the vacuum wavelength of the laser light. If second-order DFB is desired, then the grating period must be about 1/3 the laser light wavelength. If the laser operates based on facet-reflection or first-order DFB, the laser beam is emitted from the cleaved facet(s) of the laser chip. If the laser operates on second-order DFB, the low divergence beam of interest is emitted from the chip through the surface adjacent to the grating (the epi-side) or through the surface on the other side of the chip (the substrate side). A sketch of a laser chip operating in the substrate emission mode is shown in Figure 1-5 [5].

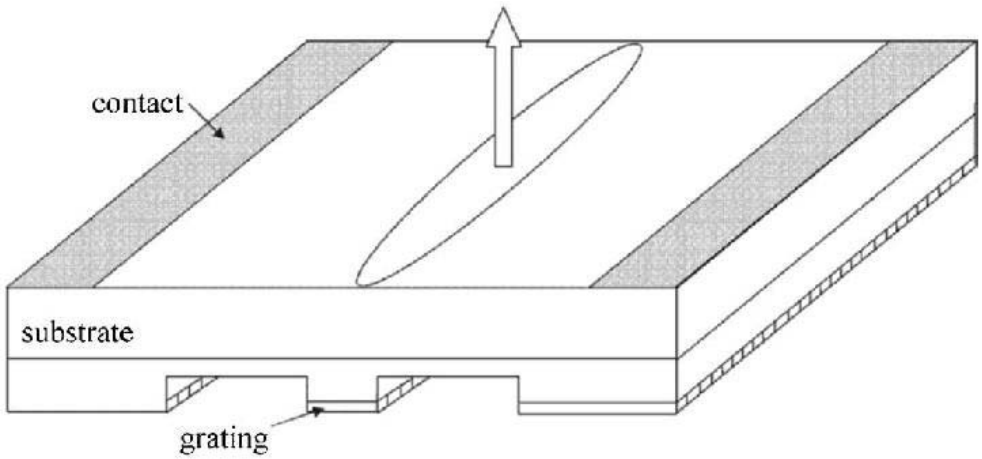

Figure 1-5. Schematic structure of a substrate-emitting DFB-QCL [5]

If laser beam absorption in the substrate material is small, substrate emission is preferred over epi-side emission because active region temperature can be minimized in this configuration. This is particularly important in QCLs where the efficiency for converting electrical power to laser power in the active region is about 10%.

In 2006, it was realized here at UF that a DFB-QCL operating in the substrate emission mode had never been reported in the literature. As a consequence it was decided to see if a device of this type could be made. By early 2007, a successful prototype was demonstrated, and the work published in that year [5]. While narrow spectral band and low divergence beams were obtained, the devices did not operate at room temperature. Since room temperature operation is highly desirable for most applications, we asked the question what could we change in the design to make this possible? One obvious possibility was to improve the material so that more optical gain was obtained for a given current density. Another was the possibility to increase the DFB coupling coefficient κ. In designing the prototype device, κ was determined using a rough estimate since this parameter is very difficult to compute exactly. This difficulty arises because one component of the electric field in QCL beams in the waveguide configuration shown in Figure 1-4 is constrained to be perpendicular to the plane of the layers. In this case, the laser beam intensity builds up at the metal interface rather than going to zero as it does in conventional diode lasers operating with their electric field parallel to the plane of the layers. The reason that the beam must have an electric field component normal to the plane of the layers in QCLs is due to the fact that the intersubband photon transitions required for optical gain can only be stimulated by electric fields normal to the plane of the active quantum wells within these layers [3][6].

In the semiconductor laser literature, lasers of this type are said to have transverse magnetic (TM) polarization because the only magnetic field component in the beam is transverse to the beam direction. If the only electric field component in the beam is parallel to the plane of the layers, the laser is said to have transverse electric (TE) polarization.

1.4 Dissertation Organization

The goal of this work is to discuss in detail the method(s) used to determine the DFB coupling coefficients for light traveling on the fundamental TM and TE modes of metal/dielectric corrugated waveguides of the type shown in Figure 1-4. In the first part of Chapter 2 and Appendix A, electromagnetic wave theory is used to explain the concept of modes in planar (non-corrugated) multi-layer waveguide structures and provide the foundation for the more complex mathematical treatments in later chapters. In the second part of Chapter 2, the ray optics and wave vector pictures of mode propagation in planar guides are introduced and then used to explain the basics of first and second order DFB. In Chapter 3, the planar or zero-order DFB model used in Chapter 2 is extended to first and second order DFB models using the Truncated Floquet-Boch Formalism. It is shown that by satisfying the magnetic and electric field tangential boundary conditions at the waveguide interfaces, one obtains a linear algebra problem involving the product of two matrices. One of these matrices is expressed in terms of the amplitudes of the magnetic field in the various layers. The other matrix is expressed in terms of the coefficients of the magnetic field amplitudes. The derivation of the eigenmode equations associated with setting the determinant of the coefficient matrices equal to zero are given in Appendices B and C. In Chapter 4, the computational techniques used to find the DFB coupling coefficients are discussed and

the numerical results for various waveguide configurations presented. In Chapter 5, the model used in Chapter 3 (ModA) is extended to a more exact model (ModB) in which the electromagnetic fields in the metal are no longer assumed to be zero. Comparisons between Mod A and Mod B are shown using various figures. Explanations and discussions about the figures are included. Chapter 6 discusses the DFB-QCL shown in Figure 1-5, and ModB is used to determine the DFB coupling coefficient. This work is summarized in Chapter 7 and suggestions for future work will be discussed.

CHAPTER 2
FUNDAMENTAL OF WAVEGUIDES

In this chapter, key concepts and terminology about planar and corrugated waveguides will be defined and discussed. The three-layer planar waveguide will serve as an example. Maxwell equations are used to derive the wave equations for TE and TM fundamental guided modes. The beam intensity profile which relates to Poynting vector will be derived and numerically plotted. The second part of this chapter will discuss the basic concepts of corrugated waveguides. Two special cases: first-order distributed feedback and second-order distributed feedback will be further discussed.

2.1 Planar Waveguide Concepts

A basic three-layer semiconductor laser planar waveguide is shown in Figure 2-1. In general, the optical properties of each layer are specified by a complex refractive index n_j, where the imaginary part determines the gain or loss coefficient of an electromagnetic wave traveling in that layer. If the real part of n_a is greater than n_b and n_d, light traveling in the z-direction can be trapped in the vicinity of the active layer by total internal reflection at the a-b, a-d interfaces. If the imaginary part of n_a is such that light traveling in the z-direction sees optical gain, the light will be amplified and laser action becomes possible.

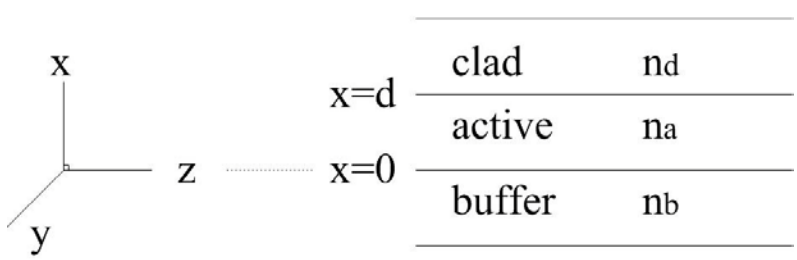

Figure 2-1. Basic 3-layer semiconductor laser one-dimensional waveguide

To actually form a laser beam in a waveguide, there must be a variation in the refractive index in the y-direction (lateral direction) as well as the x-direction (transverse direction) shown in Figure 2-1 One such structure producing a lateral refractive index variation is shown in Figure 2-2 where the stripe layer defines the section of layered material in which the active layer underneath has optical gain. If the effective refractive index above the stripe layer is greater than the effective refractive indices on either side, then light traveling in the z-direction will be trapped in the vicinity of the region above the stripe layer as shown in Figure 2-2.

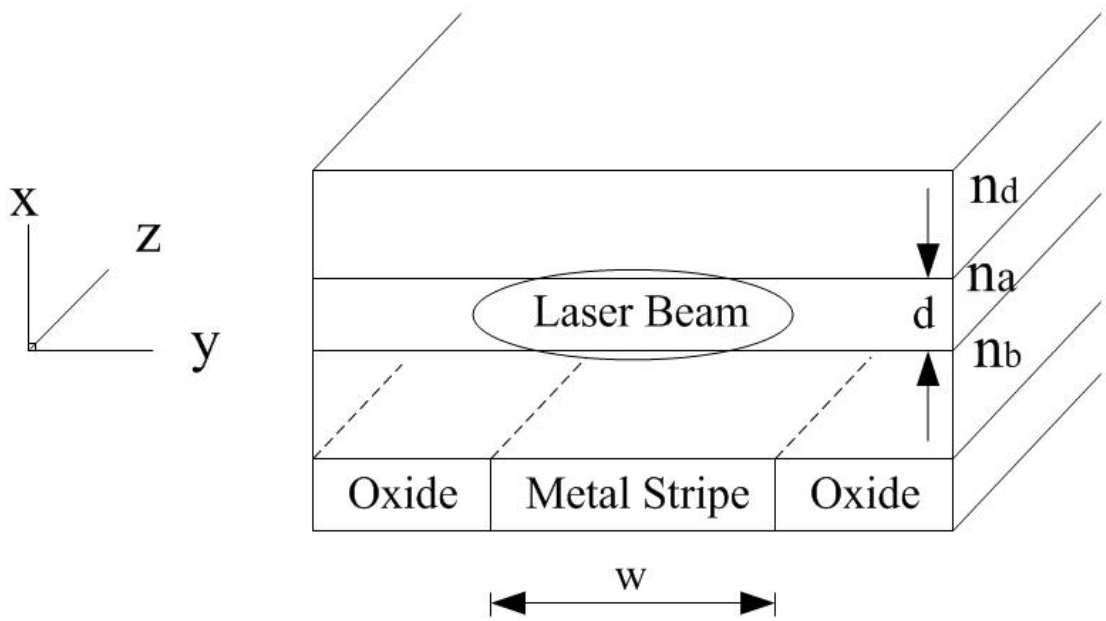

Figure 2-2. Basic two-dimensional semiconductor laser waveguide

The electric field amplitude associated with the elliptical beam cross section (transverse section) sketched in Figure 2-2 can be defined in general by a complex vector function $\boldsymbol{E}\left(x, y, \phi_{xy}\right)$, where ϕ_{xy} defines the relative phase of each point on the beam wave front. Since this possible phase variation has no bearing on the concepts to

be discussed, it will be assumed in further discussion that ϕ_{xy} is zero and in general that $\mathbf{E}(x, y, \phi_{xy})$ = $\mathbf{E}(x, y)$ is given by:

$$\mathbf{E}(x, y) = E_x(x, y)\hat{i} + E_y(x, y)\hat{j} + E_z(x, y)\hat{k} \tag{2-1a}$$

The corresponding magnetic field function $\mathbf{H}(x, y, \phi'_{xy})$ = $\mathbf{H}(x, y)$ is given by:

$$\mathbf{H}(x, y) = H_x(x, y)\hat{i} + H_y(x, y)\hat{j} + H_z(x, y)\hat{k} \tag{2-1b}$$

where $\hat{i}$, $\hat{j}$, $\hat{k}$ are the unit vectors in x, y and z directions.

Assuming the laser beam is traveling in the + z-direction, the general expressions for the two vector functions defining the whole beam, electric field $\mathbf{E}(x, y, z, t)$ and magnetic field $\mathbf{H}(x, y, z, t)$, can be written in the form:

$$\mathbf{E}(x, y, z, t) = \mathbf{E}(x, y) \cdot \exp\left[i(\beta z - \omega t)\right] \tag{2-2a}$$

$$\mathbf{H}(x, y, z, t) = \mathbf{H}(x, y) \cdot \exp\left[i(\beta z - \omega t)\right] \tag{2-2b}$$

As shown in detail in Appendix A, each of four transverse components of the beam functions, $E_x(x, y)$, $E_y(x, y)$, $H_x(x, y)$ and $H_y(x, y)$ can be expressed as linear combinations of the spatial derivatives of the longitudinal components, $E_z(x, y)$ and $H_z(x, y)$. As a consequence, the general transverse field of a beam in a waveguide can be written as a linear combination of a transverse electric (TE) beam and a transverse magnetic (TM) beam. As shown in equations A in Appendix A, the TE beam has in general 4 non-zero terms involving spatial derivatives of $H_z(x, y)$ and the TM beam has in general 4 non-zero terms involving spatial derivatives of $E_z(x, y)$.

Experimentally, the beams from semiconductor lasers are either TE or TM. Our major interest, quantum cascade semiconductor lasers (QCLs), always generate TM beams because of the selection rules governing intersubband radiative transitions [6]. As a consequence, the only non-zero transverse field terms are those involving the spatial derivatives of $E_z(x, y)$, viz.

$$E_x = \frac{i\beta}{k_t^2}\frac{\partial E_z}{\partial x} \tag{2-3}$$

$$E_y = \frac{i\beta}{k_t^2}\frac{\partial E_z}{\partial y} \tag{2-4}$$

$$H_x = \frac{-i\omega\varepsilon}{k_t^2}\frac{\partial E_z}{\partial y} \tag{2-5}$$

$$H_y = \frac{i\omega\varepsilon}{k_t^2}\frac{\partial E_z}{\partial x} \tag{2-6}$$

The beam cross-section sketched in Figure 2-2 represents what is called the fundamental TM mode of the waveguide. Although in principle a QCL can oscillate on many TM modes simultaneously, modes other than the fundamental are usually suppressed in such waveguides by making the active layer thickness d and stripe width w sufficiently small. In the remainder of this work, we will assume that the laser mode under discussion is a fundamental TM mode.

It is customary to compare the near field measurement at the laser output facet to the calculated time-average of the Poynting vector $\boldsymbol{S}(x, y)$ in the propagation or z-direction. Since $\boldsymbol{S}$ is a function of $\mathbf{E}$ and $\mathbf{H}$, it's time dependence is sinusoidal as shown in Equations 2-2a and 2-2b and the expression for $S_{z,ave}$ is [7]

$$S_{z,ave} = \frac{1}{2}\mathrm{Re}\left[\left(\mathrm{E}\times\mathrm{H}^*\right)\cdot\hat{k}\right] \tag{2-7}$$

To the TM case, Equation 2-7 can be reduced:

$$S_{z,ave} = \frac{1}{2}\mathrm{Re}\left[\begin{vmatrix} \hat{i} & \hat{j} & \hat{k} \\ E_x & E_y & E_z \\ H_x^* & H_y^* & 0 \end{vmatrix}\cdot\hat{k}\right] \tag{2-8}$$

The effective refractive index method shows that computations can be greatly simplified without loss of accuracy by setting $\partial/\partial y = 0$ in the above equations representing E_x, E_y, H_x and H_y.

There are two reasons for this assumption. The aspect ratio of the elliptical beam at the laser output facet is usually 5:1, as shown in Figure 2-2, so the field variation in y-direction is relatively small compared with the variation in x-direction. The small effective refractive index, in lateral direction, results in weak lateral beam confinement.

In TM modes, E_y in equation 2-4 and H_x in equation 2-5 vanish, the only non-zero wave components in equation 2-8 are. E_x, E_z and H_y.

$$S_{z,ave} = \frac{1}{2}\mathrm{Re}\left[\begin{vmatrix} \hat{i} & \hat{j} & \hat{k} \\ E_x & 0 & E_z \\ 0 & H_y^* & 0 \end{vmatrix}\cdot\hat{k}\right]$$

$$= \frac{1}{2}\mathrm{Re}\left[E_x H_y^*\right] \tag{2-9}$$

Substituting Equations 2-3 and 2-6 into Equation 2-9, $S_{z,ave}$ becomes:

$$S_{z,ave} = \frac{1}{2}\mathrm{Re}\left[\left(\frac{\beta}{\omega\varepsilon_0 n_j^2}H_y\right)H_y^*\right]$$

$$= \frac{\beta}{2\omega\varepsilon_0}\left(\frac{1}{n_j^2}\right)\cdot\left|H_y\right|^2 \tag{2-10}$$

where n_j is the refractive index in each layer j

To calculate the $S_{z,ave}$ in Equation 2-10, H_y needs to be derived in the following.

E_z can be obtained from Equation A-16 in Appendix A.

$$E_z = \frac{1}{(\sigma - i\omega\varepsilon)}\frac{\partial H_y}{\partial x} \tag{2-11}$$

Take the derivative of Equation 2-11

$$\frac{\partial E_z}{\partial x} = \frac{1}{(\sigma - i\omega\varepsilon)}\frac{\partial^2 H_y}{\partial x^2} \tag{2-12}$$

From equation 2-6, replacing $\frac{\partial E_z}{\partial x}$ with $\frac{\partial^2 H_y}{\partial x^2}$ from equation (2-12) to obtain the wave equation in each layer j for TM modes

$$\frac{\partial^2 H_{y,j}(x,0)}{\partial x^2} + \left(1 - \frac{\sigma}{i\omega\varepsilon}\right)\left[\left(k^2 n_j^2 - \beta^2\right) + i\omega\mu\sigma\right]H_{y,j}(x,0) = 0 \tag{2-13a}$$

If $\sigma = 0$ for each dielectric layer, Equation 2-13a will become:

$$\frac{\partial^2 H_{y,j}(x,0)}{\partial x^2} + \left(k^2 n_j^2 - \beta^2\right)H_{y,j}(x,0) = 0 \tag{2-13b}$$

Solving the differential Equations 2-13b for the waveguide in Figure 2-1, we obtain the following form for H_y in each layer [7][20]:

$$H_{y,j} = \begin{Bmatrix} H_d \\ H_a \\ H_b \end{Bmatrix} = \begin{cases} G_d \cdot \exp\left[-q(x-d)\right] & , \quad x \geq d \\ F \cdot \cos(k_x x) + G \cdot \sin(k_x x) & , \quad 0 \leq x \leq d \\ F_b \cdot \exp\left[-p\left(-(x-0)\right)\right] & , \quad x \leq 0 \end{cases} \tag{2-14}$$

where $k_x^{\ 2} = n_a^2 k^2 - \beta^2$, $p^2 = \beta^2 - n_b^2 k^2$, $q^2 = \beta^2 - n_d^2 k^2$ are transverse wave constants. F, G, F_b and G_d are constants. In the next section, we will use wave vector diagram to show the relationship between the transverse wave constants and β.

For TM modes, the tangential component of the magnetic field (H_y) in Equation 2-14 and the tangential component of the electric field (E_z) in Equation 2-11 must be continuous at the following two layer interfaces at: (1) x=0; (2) x=d, as shown in Figure 2-1.

(1) At x = 0, application of the boundary conditions $H_{y,b}(0) = H_{y,a}(0)$ and $E_{z,b}(0) = E_{z,a}(0)$ leads to:

$$F_b - F = 0 \tag{2-15}$$

$$\frac{p}{\varepsilon_b} F_b - \frac{k_x}{\varepsilon_a} G = 0 \tag{2-16}$$

(2) At x = d, application of the boundary conditions $H_{y,a}(d) = H_{y,d}(d)$ and $E_{z,a}(d) = E_{z,d}(d)$ leads to

$$\cos(k_x d) \cdot F + \sin(k_x d) \cdot G - G_d = 0 \tag{2-17}$$

$$-\frac{k_x}{\varepsilon_a} \cdot \sin(k_x d) \cdot F + \frac{k_x}{\varepsilon_a} \cdot \cos(k_x d) \cdot G + \frac{q}{\varepsilon_d} G_d = 0 \tag{2-18}$$

Equations 2-15 to 2-18 constitute a linear homogeneous matrix system with four variables F_b, F, G, G_d and can be written in the following matrix:

$$\begin{bmatrix} 1 & -1 & 0 & 0 \\ \frac{\varepsilon_a}{\varepsilon_b} p & 0 & -k_x & 0 \\ 0 & \cos(k_x d) & \sin(k_x d) & -1 \\ 0 & -k_x \cdot \sin(k_x d) & k_x \cdot \cos(k_x d) & \frac{\varepsilon_a}{\varepsilon_d} q \end{bmatrix} \begin{bmatrix} F_b \\ F \\ G \\ G_d \end{bmatrix} = 0 \tag{2-19}$$

The number of equations is equal to the number of variables. To have a nontrivial solution for the four variables F_b, F, G, G_d, the determinant of the 4 x 4 coefficient matrix should be zero.

$$\begin{vmatrix} 1 & -1 & 0 & 0 \\ \frac{\varepsilon_a}{\varepsilon_b} p & 0 & -k_x & 0 \\ 0 & \cos(k_x d) & \sin(k_x d) & -1 \\ 0 & -k_x \cdot \sin(k_x d) & k_x \cdot \cos(k_x d) & \frac{\varepsilon_a}{\varepsilon_d} q \end{vmatrix} = 0 \tag{2-20}$$

Manipulating Equation 2-20 leads to the following transcendental equation:

$$\tan(k_x d) = \frac{\left(\frac{\varepsilon_a}{\varepsilon_d} q + \frac{\varepsilon_a}{\varepsilon_b} p\right) k_x}{k_x^2 - \frac{\varepsilon_a}{\varepsilon_d} \frac{\varepsilon_a}{\varepsilon_b} pq} \tag{2-21}$$

It is customary to specify the refraction index of each layer (n_j) in these multi-layer structures. As a consequence, the medium permittivity ε_j in Equation 2-21 is replaced by $\varepsilon_0 \, n_j^{\,2}$, where ε_0 is the vacuum permittivity

$$\tan(k_x d) = \frac{\left(\frac{n_a^2}{n_d^2} q + \frac{n_a^2}{n_b^2} p\right) k_x}{k_x^2 - \frac{n_a^2}{n_d^2} \frac{n_a^2}{n_b^2} pq} \tag{2-22}$$

In order to show explicitly that only certain values of k_x are allowed by Equation 2-22 thereby giving rise to the modal nature light propagation in waveguides, one uses the trigonometric identities to obtain the following dispersion relationship expressed by the phase angles and mode number M:

$$k_x d = \tan^{-1}\left(\frac{n_a^2}{n_d^2}\frac{q}{k_x}\right) + \tan^{-1}\left(\frac{n_a^2}{n_b^2}\frac{p}{k_x}\right) + M\pi \qquad (2\text{-}23)$$

Take the three-layer waveguide shown in Figure 2-1 for example. The active layer thickness is d =0.1 μm and vacuum wavelength is λ_v = 0.85 μm. For this near-infrared (NIR) wavelength range, the material combination of GaAs for active layer and $Al_xGa_{1-x}As$ for cladding and buffer layers are commonly used. The buffer layer refractive index is depends of the mole fraction x or the AlAs compostion in $Al_xGa_{1-x}As$, and this relationship is shown in equation 2-24 [8].

$$n_b(x) = 3.590 - 0.710x + 0.091x^2 \qquad (2\text{-}24)$$

The GaAs has refractive index about 3.6 and AlAs has refractive index close to 3.0. The lower fraction of AlAs will make the cladding and buffer layer have lower refractive indices. The ratio of n_a/n_b become larger, the more energy of propagating wave will be confined in the active layer and the confinement factor Γ will become larger. However, this compound alloy has direct bandgap when the fraction x of AlAs is less than 0.45 and its corresponding refractive index is about 3.3 [8]. Semiconductor with indirect bandgaps are not efficient light emitters for applications [9]. Other factors and more advanced opto-physical effects which will cause the change of refractive index are discussed in [10] and [11]. In this dissertation, the refractive indices for

general GaAs/AlGaAs waveguides are n_a = 3.6 and n_b = n_d = 3.4. The effective refractive index n_e is 3.4266 can be numerically solved from Equation 2-22.

Figure 2-3 shows the schematic plot of $\left(1/n_j^2\right)\cdot H_{y,j}\left(x,0\right)^2$ vs. x for TM modes. Since the active layer has higher refractive index so the profile of the plot will be lower.

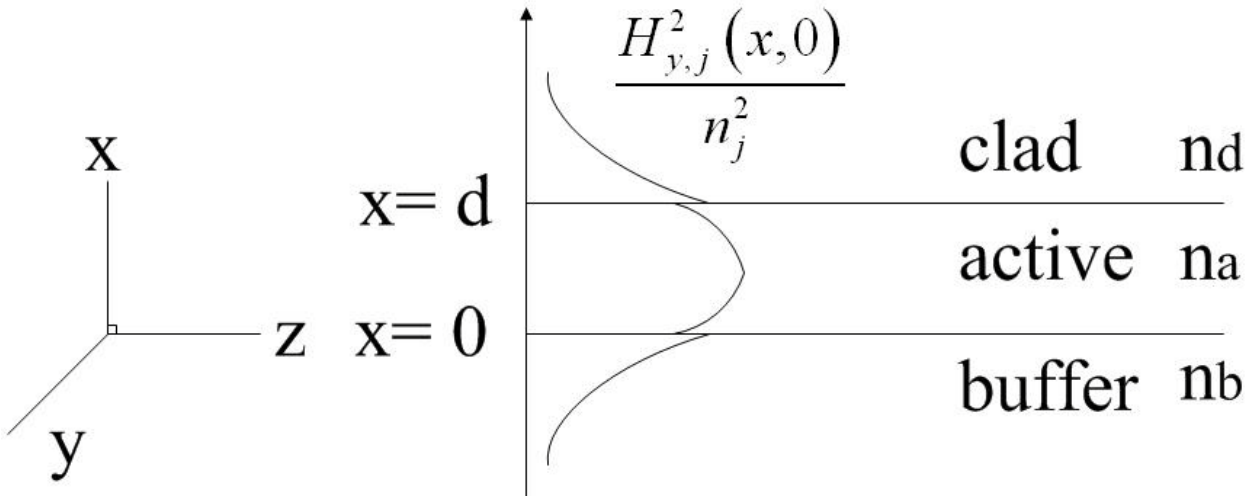

Figure 2-3. Schematic plot of $\left(1/n_j^2\right)\cdot H_{y,j}\left(x,0\right)^2$ vs. x for the fundamental TM mode

From Equation 2-14, $H_y\left(x,0\right)$ in each layer j is calculated. Figure 2-4 shows the calculated result of $\left(1/n_j^2\right)\cdot H_{y,j}\left(x,0\right)^2$ vs. x for the relative quantity pointing vector deriver in Equation 2-10.

Figure 2-4 is particularly interesting for semiconductors lasers operating in a TM modes since the $S_z\left(x,0\right)$ function is discontinuous due to the different refractive indices in each layer. The measured beam profile of QCLs utilizing TM mode also have such unsmooth at the a-b and a-d interfaces [12].

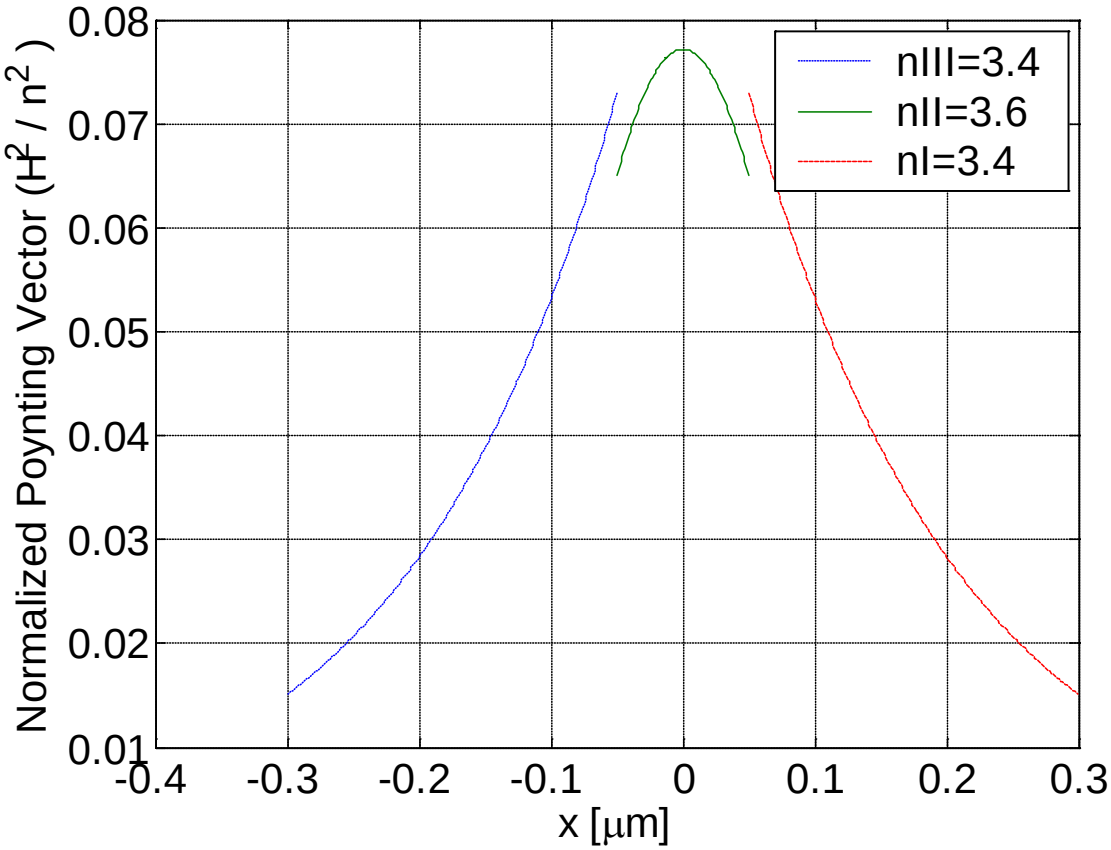

Figure 2-4. Calculated plot of $\left(1/n_j^2\right)\cdot H_{y,j}\left(x,0\right)^2$ vs. x for the fundamental TM mode

As discussed in the Introduction section, the main interest in this work is to determine the coupling coefficients responsible for laser oscillation and output power in corrugated waveguides. In order to understand the behavior of guided waves in waveguides of this type, it is useful to introduce the ray optics or bouncing ray picture of wave propagation. Since the light waves travel in the z-direction but are trapped in the vicinity of the active layer by total internal reflection at the a-b and a-d interfaces, wave propagation can be depicted as shown in Figure 2-5. The angle associated with the zig-zag motion of the light ray is called the mode bounce angle.

Figure 2-5 shows the bouncing ray in a three-layer waveguide in the fundamental mode. The incident rays come from the left side and propagate in the direction as the arrow indicated. The critical angels [13] at upper interface and lower interfaces are:

$$\theta_d = \sin^{-1}\left(\frac{n_d}{n_a}\right) \tag{2-25}$$

$$\theta_b = \sin^{-1}\left(\frac{n_b}{n_a}\right) \tag{2-26}$$

If $\max(\theta_b, \theta_c) < \theta_i < \frac{\pi}{2}$, the propagating light will be confined inside the active layer by the total internal reflection. This light will propagate along the z-direction in a zigzag path as shown in Figure 2-5. θ_0 is the bounce angle for the incident wave P_0.

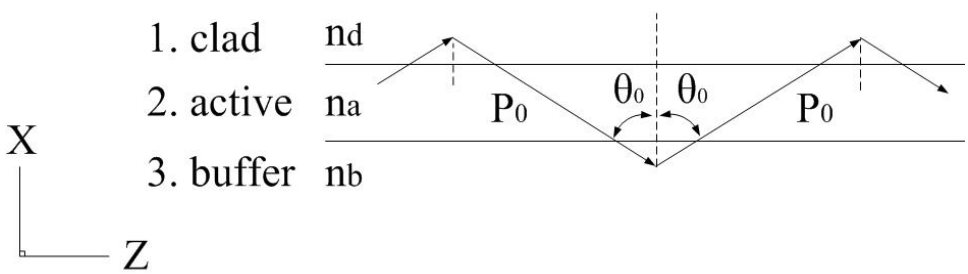

Figure 2-5. Bouncing ray in a guided-mode waveguide

Figure 2-6 [14] shows the relationship among the propagation constant in the z-direction in the fundamental mode, β_0, the effective incident angle θ_0, and wave vector k. The relationships can be expressed as follows:

$$k_z = k \cdot n_a \cdot \sin\theta_0 = k \cdot n_e = \beta_0 \tag{2-27a}$$

$$k_x = k \cdot n_a \cdot \cos\theta_0 = \sqrt{n_a^2 k^2 - \beta_0^2} \tag{2-27b}$$

In the above equation, $k = 2\pi/\lambda_0$ is the wave vector in vacuum. λ_0 is the wavelength in vacuum. n_e is considered to be the effective refractive index .

From Figure 2-6, for a fixed magnitude of incident wave vector, $n_a k$, its longitudinal component, $k_z = \beta_0$, and its transverse component, k_x, will determine the propagation behavior in this waveguide. The larger the real value of β_0 is, the more propagation along the z-direction. If the component β_0 is too small and k_x is large, the waveguide may have less propagation in the z direction and radiation out of from either buffer layer or clad later in the x direction, called radiation mode [7].

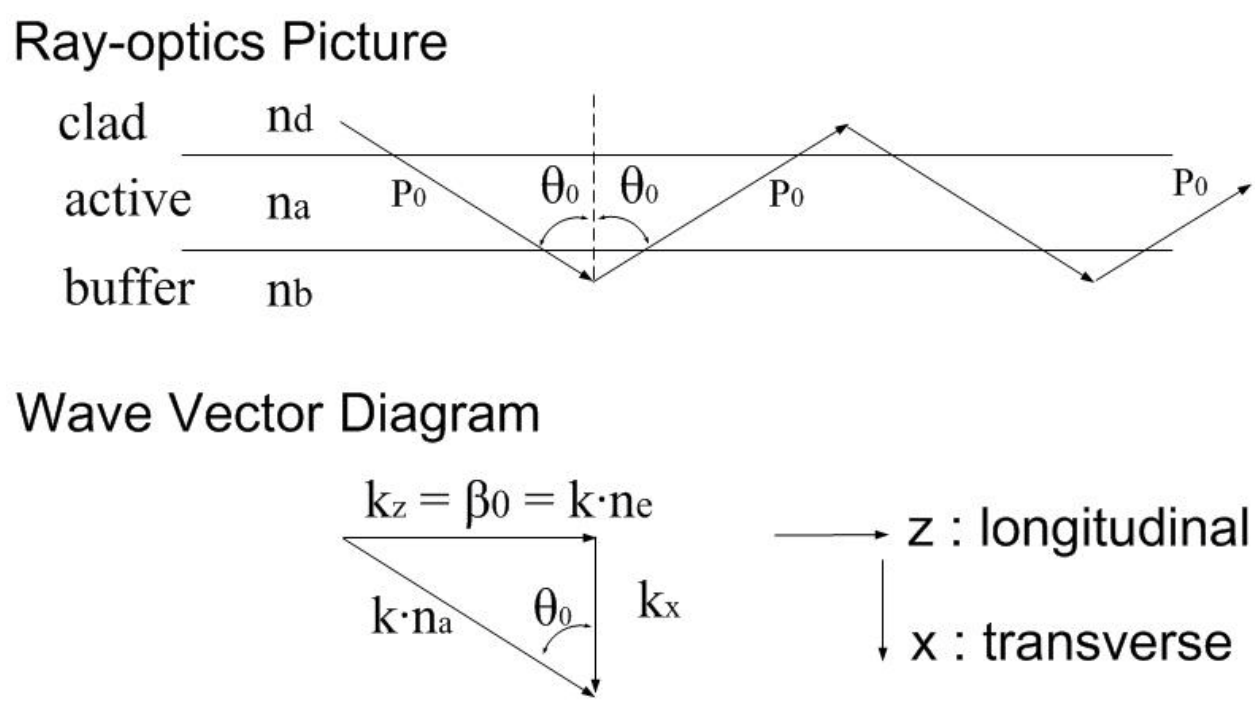

Figure 2-6. Wave propagation in the fundamental mode

These two key parameters, n_m and β, will help derive and analyze mathematical models in Chapter 3 and 4.

2.2 Corrugated Four-Layer Waveguides

2.2.1 Diffractive Waves in Corrugated Waveguides

Figure 2-7 shows the corrugated grating will generate diffracted waves. Under the buffer layer, a corrugated metal layer with refractive index n_c is added. The incident wave in terms of power can be expressed as P_0, the first-order diffractive wave P_{-1}, and the second-order diffractive wave P_{-2}.

A

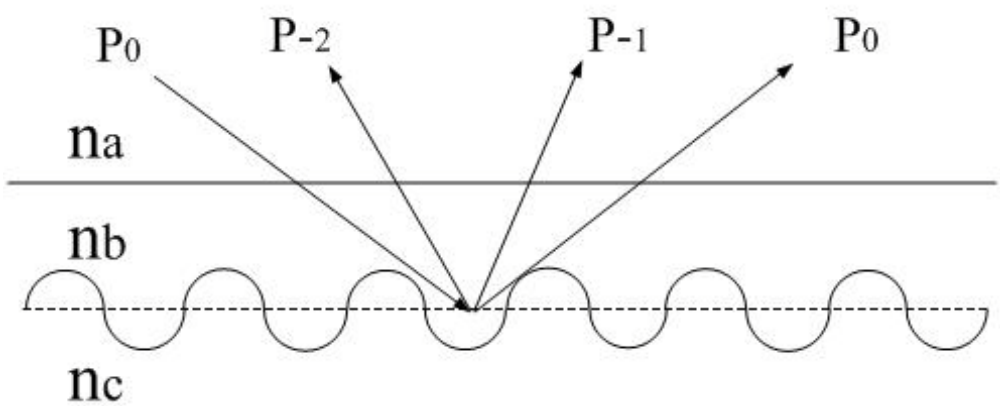

B

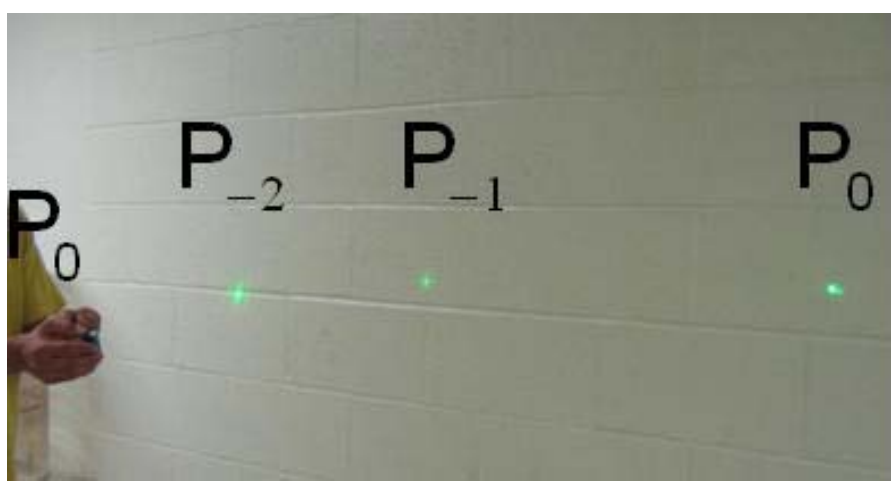

Figure 2-7. Diffraction caused by corrugated waveguide. A) Diffractive waves due to gratings B) Real picture of diffraction

2.2.2 First-Order Distributed Feedback in Corrugated Waveguides

Next, two special diffraction cases in such corrugated waveguides will be discussed. If the first-order diffractive wave P_{-1} happens to be the reverse direction of P_0 after one backward grating shift, it is called the first-order distributed feedback (DFB). Figure 2-8 (a) shows the ray picture for this case.

A

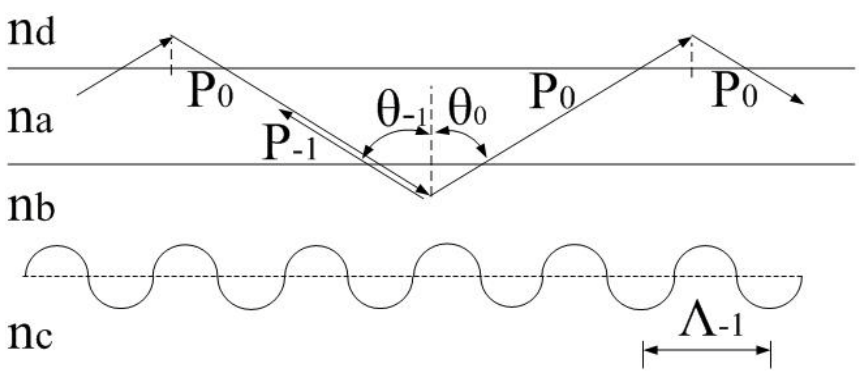

B

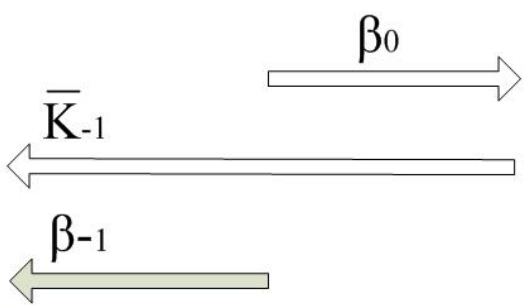

Figure 2-8. First-order DFB. A) Ray optics picture B) Wave-vector diagram

Figure 2-8 (b) shows the following relationship.

$$\beta_0 - \overline{\mathrm{K}}_{-1} = \beta_{-1} = -\beta_0 \quad \Rightarrow \overline{\mathrm{K}}_{-1} = 2\beta_0 \tag{2-28}$$

In Equation 2-28, the grating vector $\overline{\mathrm{K}}_{-1} = 2\pi/\Lambda_{-1}$, where Λ_{-1} is the grating period [15] for the first-order DFB.

Substituting Equation 2-7a into Equation 2-8, the grating period Λ_{-1} for the first-order DFB is

$$\Lambda_{-1} = \frac{\lambda}{2n_e} \tag{2-29}$$

Substituting Equation 2-7a into Equation 2-28, the bounce angle θ_{-1} for the first-order DFB has the same magnitude with θ_0

$$\beta_{-1} = k \cdot n_a \cdot \sin\theta_{-1} = -\beta_0 = -k \cdot n_a \cdot \sin\theta_0 \quad \Rightarrow \theta_{-1} = -\theta_0 \tag{2-30}$$

2.2.3 Second-Order Distributed Feedback in Corrugated Waveguides

If the second-order diffractive wave P_{-2} happens to be the reverse direction of P_0 after two grating shifts, it is called the second-order distributed feedback (DFB). Figure 2-9 (a) shows the ray picture for this case.

Figure 2-9 (b) shows the following relationship for the second-order DFB.

$$\beta_0 - 2\overline{\mathrm{K}}_{-2} = \beta_{-2} = -\beta_0 \quad \Rightarrow \overline{\mathrm{K}}_{-2} = \beta_0 \tag{2-31}$$

Substituting Equation 2-27(a) into Equation 2-31, the bounce angle θ_{-2} for the second-order DFB has the same magnitude with θ_0

$$\beta_{-2} = k \cdot n_a \cdot \sin\theta_{-2} = -\beta_0 = -k \cdot n_a \cdot \sin\theta_0 \quad \Rightarrow \theta_{-2} = -\theta_0 \tag{2-32}$$

Figure 2-9 shows the following relationship for the first-order diffractive waves. This first-order feedback waves P_{-1}, after one backward grating shift, diffract out perpendicularly to the z direction (i.e. $\theta_{-1} = 0$) so it does not have the propagation component along z direction.

$$\beta_0 - \overline{\mathrm{K}}_{-2} = \beta_{-1} = k \cdot n_a \cdot \sin 0^\circ = 0 \quad \Rightarrow \overline{\mathrm{K}}_{-2} = \beta_0 \tag{2-33}$$

Equations (2-31) and (2-33) show the conditions for second-order DFB match with each other. Substituting Equation (2-27a) into Equation either 2-31 or 2-33, the grating period Λ_{-2} for the second-order DFB is

$$\Lambda_{-2} = \frac{\lambda}{n_e} \tag{2-34}$$

A

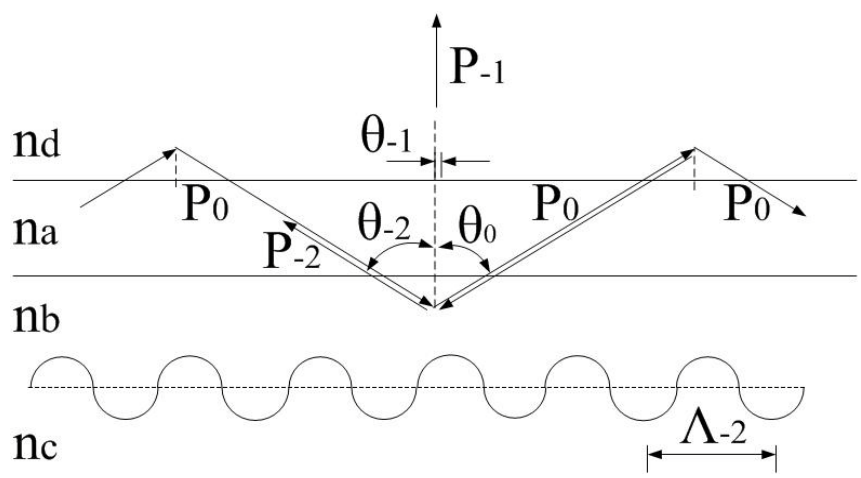

B

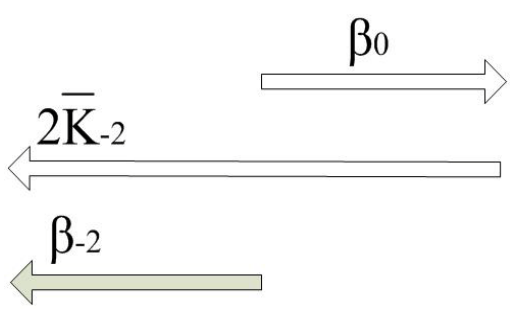

Figure 2-9. Second-order DFB. A) Ray optics picture B) Wave-vector diagram for the second order diffractive wave C) Wave-vector diagram for the first order diffractive wave

Compare Figure 2-8 and Figure 2-9, we can notice the second-order DFB will have smaller beam divergence angle [5] than the first-order DFB. Equation 2-15 shows

the divergence angle θ_D is proportional to wavelength λ and inversely proportional to the beam emission aperture D [16][17].

$$\theta_D \propto \frac{\lambda}{D} \tag{2-35}$$

Figure 2-10 (a) shows first-order DFB lasers emit beams from the edge of active layers and directions of beams are normal to the edge cross-section of active layers, also called edge-emitting lasers. The emission apertures (D_{-1}) are equal to the active layers thickness (d) which is usually in microns and about 1,000 times smaller than the emission apertures of substrate-emitting lasers. This small aperture will greatly increase the beam divergence and limit the practical applications in long wavelength operation.

A

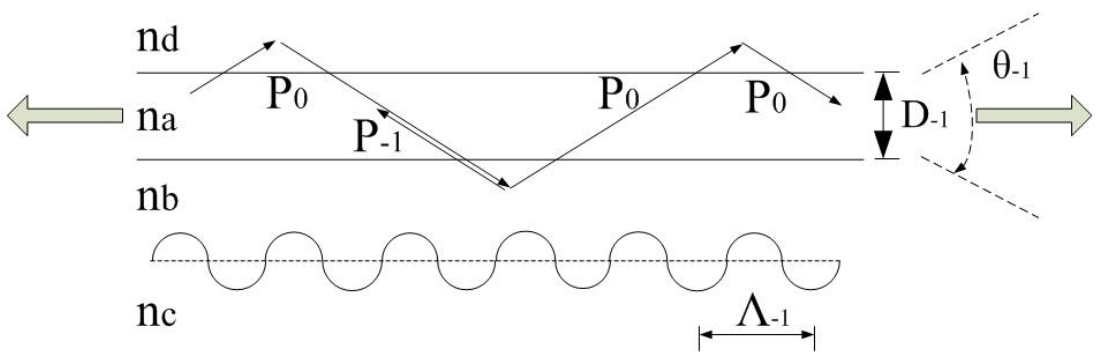

B

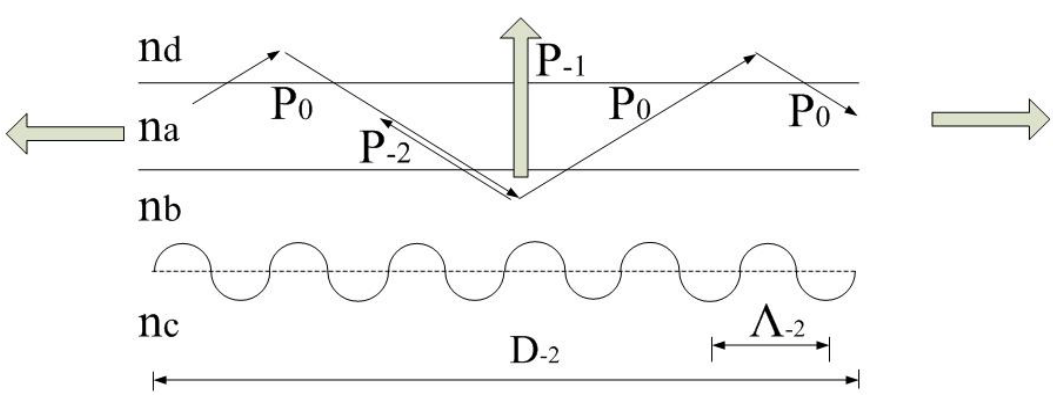

Figure 2-10. Schematic diagrams for A) First-order B) Second-order DFB

Figure 2-10 (b) shows the second order gratings have smaller beam divergence angle (θ_{-2}) due to its larger emission aperture (D_{-2}), which is equal to laser length (L), than that (θ_{-1}) of the first-order DFB grating [5]. The second order DFB lasers emit beams from the substrates and the directions of beams are normal to the substrate surfaces, also called substrate-emitting lasers. The divergences of beams are inversely proportional to the laser length, which are usually in mini meters in the direction of longitudinal direction. Applications, such as detecting explosives [18] or drugs [19], require wavelength 300 µm or 0.3 mm with high frequency in terahertz (THz, 10 to the order of 12). For extensive infrared applications such as gas sensing, optical communication [21], night-vision, thermograph/ thermal –tracking [22], the required wavelength range is from 0.7 µm up to1 mm. Second-order DFB lasers can help maintain the beam divergence in a smaller range in different applications. Table 1 summarizes the first-order DFB and second-order DFB.

Table 2-1. Comparison of the first-order DFB and second-order DFB

	First-order DFB	Second-order DFB
Beam direction	Edge-emitting	Substrate-emitting
Grating period	$\Lambda_{-1} = \frac{\lambda}{2n_e}$	$\Lambda_{-2} = \frac{\lambda}{n_e}$
Divergence angle	$\theta_{-1} \propto \frac{\lambda}{D_{-1}} \approx \frac{1 \sim 10\mu m}{1\mu m}$	$\theta_{-2} \propto \frac{\lambda}{D_{-2}} \approx \frac{1 \sim 10\mu m}{1000\mu m}$

CHAPTER 3
TM EIGENMODE EQUATIONS FOR PLANAR AND DISTRIBUTED FEEDBACK CORRUGATED SENICONDUCTOR WAVEGUIDES WITH SHINY-METAL CONTACTS

Floquet-Bloch formalism was used to derive expressions yielding the TE_0 mode backward coupling coefficient (κ) in dielectric waveguides with corrugated shiny-metal contacts [Luo 93]. In this chapter, we will derive similar expressions for TM_0 modes in the same types of waveguides. As mentioned previously, TM_0 modes are of interest since quantum cascade lasers (QCLs) only operate on such modes.

3.1 Floquet-Bloch Formalism for Corrugated Waveguides

Figure 3-1 shows a semiconductor laser structure with a perfect metal sinusoidally corrugated contact layer.

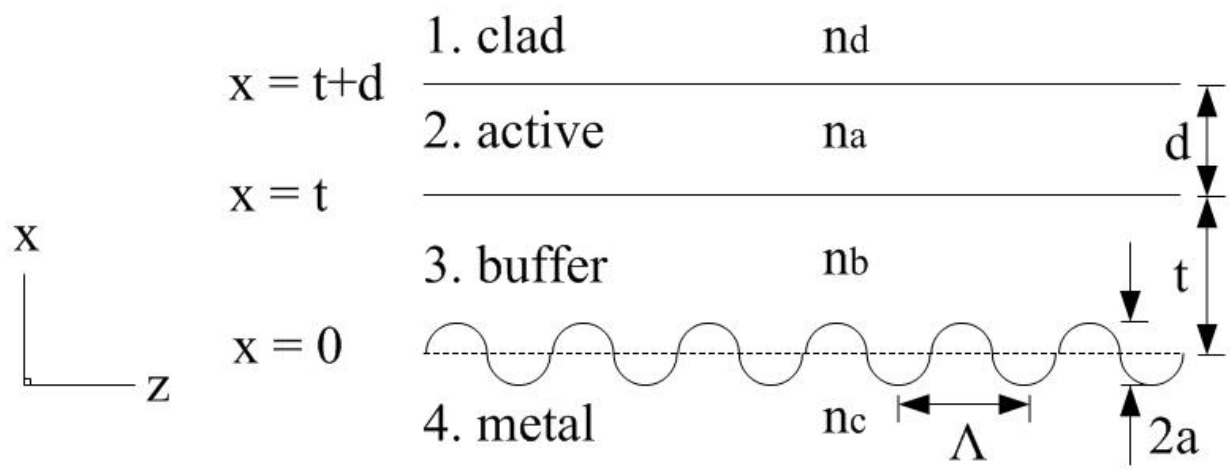

Figure 3-1. The shiny contact DFB laser structure

TM modes in such structure have their magnetic field pointing in the y direction. The coordinate system chosen has x = 0 at the interface of metal and semiconductor to simplify equations and computations. The Floquet-Bloch formalism requires that the magnetic field in each layer, cladding layer (H_d), active layer (H_a), buffer layer (H_b), and metal layer (H_c), be expanded in a plane wave series as follows:

$$H_d(x,z) = \sum_{m=-\infty}^{\infty} A_m \cdot \exp\left[-q_m\left(x-t-d\right)\right] \cdot \exp\left(-i\beta_m z\right) \tag{3-1}$$

$$H_a(x,z) = \sum_{m=-\infty}^{\infty} \left\{B_m \cdot \cos\left[\sigma_m\left(x-t\right)\right] + C_m \cdot \sin\left[\sigma_m\left(x-t\right)\right]\right\} \cdot \exp\left(-i\beta_m z\right) \tag{3-2}$$

$$H_b(x,z) = \sum_{m=-\infty}^{\infty} \left\{D_m \cdot \exp\left(p_m x\right) + E_m \cdot \exp\left(-p_m x\right)\right\} \cdot \exp\left(-i\beta_m z\right) \tag{3-3}$$

$$H_c(x,z) \approx 0 \tag{3-4}$$

$$\beta_m = \beta_0 + m\overline{\mathrm{K}} = \beta_0 + m\left(\frac{2\pi}{\Lambda}\right) \tag{3-5}$$

$$\sigma_m = \sqrt{n_a{}^2 k^2 - \beta_m{}^2} \tag{3-6}$$

$$p_m = \sqrt{\beta_m{}^2 - n_b{}^2 k^2} \tag{3-7}$$

$$q_m = \sqrt{\beta_m{}^2 - n_d{}^2 k^2} \tag{3-8}$$

$$k = \frac{2\pi}{\lambda} \tag{3-9}$$

In the above equations, β is the wave propagation constant, m is the index for the grating diffraction order, Λ is the grating period, λ is the vacuum wavelength, k is the wave vector and $\overline{\mathrm{K}}$ = 2π / λ is called the grating vector [15].

For TM modes, the tangential component of the magnetic field (H_y) and the tangential component of the electric field (E_z) must be continuous at the layer interfaces. The E_z continuous condition can be converted to the condition that $\frac{\partial H_y}{\partial x}$ is continuous using the following Maxwell Equation [7]:

$$\nabla \times \vec{H} = \varepsilon \frac{\partial \vec{E}}{\partial t} \tag{3-10}$$

The result for E_z is

$$E_z = \frac{i}{\omega \varepsilon_j} \frac{\partial H_y}{\partial x} \tag{3-11}$$

where ε_j is the medium permittivity in each layer j and ω is the circular frequency.

Therefore, the tangential component boundary conditions are equivalent to saying H_y and $\frac{\partial H_y}{\partial x}$ must be continuous at the following three interfaces: (1) x=t ; (2) x= t+d; (3) x = 0.

(1) At x = t, the equations of interest are Equations 3-2 and 3-3. Application of the boundary conditions leads to:

$$\begin{aligned} &\sum_{m=-\infty}^{\infty} B_m \cdot \exp\left(-i\beta_m z\right) = \sum_{m=-\infty}^{\infty} \left\{D_m \cdot \exp\left(p_m t\right) + E_m \cdot \exp\left(-p_m t\right)\right\} \cdot \exp\left(-i\beta_m z\right) \\ &\Rightarrow \quad B_m = D_m \cdot \exp\left(p_m t\right) + E_m \cdot \exp\left(-p_m t\right) \qquad ,\forall m \end{aligned} \tag{3-12}$$

$$\begin{aligned} &\sum_{m=-\infty}^{\infty} \left(\frac{\sigma_m}{\varepsilon_a}\right) C_m \cdot \exp\left(-i\beta_m z\right) = \sum_{m=-\infty}^{\infty} \left(\frac{p_m}{\varepsilon_b}\right) \left\{D_m \cdot \exp\left(p_m t\right) + E_m \cdot \exp\left(-p_m t\right)\right\} \cdot \exp\left(-i\beta_m z\right) \\ &\Rightarrow \quad \left(\frac{\sigma_m}{\varepsilon_a}\right) C_m = \left(\frac{p_m}{\varepsilon_b}\right) \left\{D_m \cdot \exp\left(p_m t\right) - E_m \cdot \exp\left(-p_m t\right)\right\} \qquad ,\forall m \end{aligned} \tag{3-13}$$

(2) At x = t + d, the equations of interest are Equations 3-1 and 3-2. Application of the boundary conditions leads to:

$$\begin{aligned} &\sum_{m=-\infty}^{\infty} A_m \cdot \exp\left(-i\beta_m z\right) = \sum_{m=-\infty}^{\infty} \left\{B_m \cdot \cos\left(\sigma_m d\right) + C_m \cdot \sin\left(\sigma_m d\right)\right\} \cdot \exp\left(-i\beta_m z\right) \\ &\Rightarrow \quad A_m = B_m \cdot \cos\left(\sigma_m d\right) + C_m \cdot \sin\left(\sigma_m d\right) \qquad ,\forall m \end{aligned} \tag{3-14}$$

$$\begin{aligned} &\sum_{m=-\infty}^{\infty} \left(\frac{q_m}{\varepsilon_d}\right) A_m \cdot \exp\left(-i\beta_m z\right) = \sum_{m=-\infty}^{\infty} \left(\frac{\sigma_m}{\varepsilon_a}\right) \left\{B_m \cdot \sin\left(\sigma_m d\right) - C_m \cdot \cos\left(\sigma_m d\right)\right\} \cdot \exp\left(-i\beta_m z\right) \\ &\Rightarrow \quad \left(\frac{q_m}{\varepsilon_d}\right) A_m = \left(\frac{\sigma_m}{\varepsilon_a}\right) \left\{B_m \cdot \sin\left(\sigma_m d\right) - C_m \cdot \cos\left(\sigma_m d\right)\right\} \qquad ,\forall m \end{aligned} \tag{3-15}$$

(3) At x = 0, it is necessary to specify an equation that describe the grating interface. In this case, the equation is:

$$x = f(z) = a \cdot \cos\left(\overline{K}z\right) = a \cdot \cos\left(2\pi \cdot \frac{z}{\Lambda}\right) \tag{3-16}$$

where 2a is the grating depth.

Since the metal contact is perfect metal, H_b vanishes at x = 0. Using Equation 3-3, this condition leads to:

$$\sum_{m=-\infty}^{\infty} \left\{ D_m \cdot \exp\left(p_m \cdot f(z)\right) + E_m \cdot \exp\left(-p_m \cdot f(z)\right) \right\} \cdot \exp\left(-i\beta_m z\right) = 0 \tag{3-17}$$

By Fourier series expansion, the exponential terms in Equation (3-17) become [23]:

$$\exp\left[\pm p_m \cdot f(z)\right] = \exp\left[\pm p_m a \cos\left(\overline{K}z\right)\right] = \sum_{n=-\infty}^{\infty} I_n\left(\pm p_m a\right) \exp\left[i\left(\overline{K}z\right)n\right] \tag{3-18}$$

where $I_n(u)$ is the modified or (hyperbolic) Bessel function of the first kind of order n. This function has the following properties:

$$\begin{aligned} I_n(-u) &= (-1)^n I_n(u) \\ I_{-n}(u) &= I_n(u) \end{aligned} \tag{3-19}$$

Substituting Equation 3-18 and 3-19, Equation 3-17 becomes:

$$\sum_{m=-\infty}^{\infty} \left\{ D_m \cdot \sum_{n=-\infty}^{\infty} I_n\left(p_m \cdot a\right) \cdot \exp\left(i\left(\overline{K}z\right)n\right) \right.$$

$$\left. + E_m \cdot \sum_{n=-\infty}^{\infty} (-1)^n I_n\left(p_m \cdot a\right) \cdot \exp\left(i\left(\overline{K}z\right)n\right) \right\} \cdot \exp\left(-i\beta_m z\right) = 0 \tag{3-20}$$

By substituting Equation 3-5, Equation 3-20 becomes:

$$\sum_{m=-\infty}^{\infty} \left\{ D_m \cdot \sum_{n=-\infty}^{\infty} I_n\left(p_m \cdot a\right) \cdot \exp\left(-i(m-n)\left(\overline{K}z\right)\right) \right.$$

$$\left. + E_m \cdot \sum_{n=-\infty}^{\infty} (-1)^n I_n\left(p_m \cdot a\right) \cdot \exp\left(-i(m-n)\left(\overline{K}z\right)\right) \right\} \cdot \exp\left(-i\beta_0 z\right) = 0 \tag{3-21}$$

Since the coefficients of $\exp\left(-in\overline{K}z\right)$ terms for each n should be zero, we obtain:

$$\sum_{m=-\infty}^{\infty}\left\{D_m I_{m-n}\left(p_m \cdot a\right)+\left(-1\right)^{m-n} E_m I_{m-n}\left(p_m \cdot a\right)\right\}=0 \qquad ,\forall n \tag{3-22}$$

From the above equations, we can obtain a liner homogeneous matrix system with variables A_m, B_m, C_m, D_m, E_m. The number of equations is equal to the number of variables. To have a nontrivial solution for this system, the determinant of the coefficient matrix should be zero [24] [25].

In the next few sections, we will discuss three special cases: planar, first-order DFB and second-order DFB waveguides for TM modes. In section 3.2, the eigenmode equation for the planar waveguides (grating depth 2a= 0) is derived by setting m=0 in Equations from (3-12) to (3-15) and in Equation (3-22), modified Bessel functions are equal to 1 due to 2a= 0. These five equations form a 5 by 5 matrix. In section 3.3, the eigenmode equation for first-order DFB waveguides is derived by setting m= 0 and m= -1 in the above equations. This is valid because all the other m-waves are evanescent. In this case, these ten equations form a 10 by 10 matrix. In section 3.4, the eigenmode equation for second-order DFB waveguides is derived by setting m= 0, m= -1, and m= -2 in the above equations. This is valid because all the other m-waves are evanescent. In this case, these fifteen equations form a 15 by 15 matrix.

3.2 Derivation of the Eigenmode Equation for Planar Waveguides by Truncated Floquet-Bloch Formalism

A grating depth 2a = 0 is equivalent to an unperturbed, planar four-layer waveguide with a perfect metal contact. In this case, Equations 3-13, 3-14, 3-15, 3-16 and 3-17 reduce to Equations 3-23, 3-24, 3-25, 3-26 and 3-27 respectively:

$$B_0 - D_0 \cdot \exp\left(p_0 t\right) - E_0 \cdot \exp\left(-p_0 t\right) = 0 \tag{3-23}$$

$$\left(\frac{\sigma_0}{\varepsilon_a}\right)C_0-\left(\frac{p_0}{\varepsilon_b}\right)D_0\cdot\exp\left(p_0t\right)+\left(\frac{p_0}{\varepsilon_b}\right)E_0\cdot\exp\left(-p_0t\right)=0 \tag{3-24}$$

$$A_0-B_0\cdot\cos\left(\sigma_0 d\right)-C_0\cdot\sin\left(\sigma_0 d\right)=0 \tag{3-25}$$

$$\left(\frac{q_0}{\varepsilon_d}\right)A_0-\left(\frac{\sigma_0}{\varepsilon_a}\right)B_0\cdot\sin\left(\sigma_0 d\right)+\left(\frac{\sigma_0}{\varepsilon_a}\right)C_0\cdot\cos\left(\sigma_0 d\right)=0 \tag{3-26}$$

$$D_0I_0\left(0\right)+E_0I_0\left(0\right)=0 \tag{3-27}$$

$$\text{where } I_n\left(0\right)=\begin{cases}1, & n=0\\ 0, & n\neq 0\end{cases} \tag{3-28}$$

Next, we will manipulate the above 5 equations into a closed-form expression.

Equation 3-26 divided by B3-25 and use trigonometric identity [26]:

$$\frac{q_0/\varepsilon_d}{\sigma_0/\varepsilon_a}=\frac{B_0\cdot\sin\left(\sigma_0 d\right)-C_0\cdot\cos\left(\sigma_0 d\right)}{B_0\cdot\cos\left(\sigma_0 d\right)+C_0\cdot\sin\left(\sigma_0 d\right)}=\frac{\tan\left(\sigma_0 d\right)-\dfrac{C_0}{B_0}}{1+\dfrac{C_0}{B_0}\cdot\tan\left(\sigma_0 d\right)}=\left[\sigma_0 d-\tan^{-1}\left(\frac{C_0}{B_0}\right)\right]$$

$$\Rightarrow\quad \frac{C_0}{B_0}=\tan\left[\sigma_0 d-\tan^{-1}\left(\frac{q_0/\varepsilon_d}{\sigma_0/\varepsilon_a}\right)\right]=\mathrm{X}_0 \tag{3-29}$$

Equation 3-24 divided by 3-23:

$$\frac{C_0}{B_0}=\frac{p_0/\varepsilon_b}{\sigma_0/\varepsilon_a}\cdot\frac{D_0\cdot\exp\left(p_0t\right)-E_0\cdot\exp\left(-p_0t\right)}{D_0\cdot\exp\left(p_0t\right)+E_0\cdot\exp\left(-p_0t\right)}=\mathrm{X}_0$$

$$\Rightarrow\quad \frac{D_0}{E_0}=\exp(-2p_0t)\cdot\left[\frac{\dfrac{\sigma_0/\varepsilon_a}{p_0/\varepsilon_b}\cdot\mathrm{X}_0-1}{\dfrac{\sigma_0/\varepsilon_a}{p_0/\varepsilon_b}\cdot\mathrm{X}_0+1}\right] \tag{3-30}$$

Rearrange Equation 3-27:

$$I_0(0)\cdot(D_0+E_0)=I_0(0)\cdot E_0\cdot\left(\frac{D_0}{E_0}+1_0\right)=0 \tag{3-31}$$

For a non-trial solution, $D_0 \neq 0, E_0 \neq 0$, from Equation 3-31, we obtain:

$$\frac{D_0}{E_0}+1=0 \tag{3-32}$$

Compare Equations 3-30 and 3-32:

$$\frac{D_0}{E_0}=\exp(-2p_0t)\cdot\left[\frac{\frac{\sigma_0/\varepsilon_a}{p_0/\varepsilon_b}\cdot \mathrm{X}_0-1}{\frac{\sigma_0/\varepsilon_a}{p_0/\varepsilon_b}\cdot \mathrm{X}_0+1}\right]=-1$$

$$\Rightarrow \frac{\sigma_0/\varepsilon_a}{p_0/\varepsilon_b}\cdot \mathrm{X}_0=\frac{\exp(2p_0t)+1}{\exp(2p_0t)-1}=\coth\left(p_0t\right)$$

$$\Rightarrow \mathrm{X}_0=\frac{p_0/\varepsilon_b}{\sigma_0/\varepsilon_a}\cdot\coth\left(p_0t\right) \tag{3-33}$$

Combine Equations 3-29 and 3-33:

$$\mathrm{X}_0=\frac{C_0}{B_0}=\tan\left[\sigma_0 d-\tan^{-1}\left(\frac{q_0/\varepsilon_d}{\sigma_0/\varepsilon_a}\right)\right]=\frac{p_0/\varepsilon_b}{\sigma_0/\varepsilon_a}\cdot\coth\left(p_0t\right)$$

$$\Rightarrow \frac{p_0}{\varepsilon_b}\cdot\coth\left(p_0t\right)=\frac{\sigma_0}{\varepsilon_a}\cdot\tan\left[\sigma_0 d-\tan^{-1}\left(\frac{q_0/\varepsilon_d}{\sigma_0/\varepsilon_a}\right)\right] \tag{3-34}$$

It is customary to specify the refraction index of each layer (n_j) in these multi-layer structures. As a consequence, the medium permittivity ε_j in Equation 3-31 is replaced by $\varepsilon_0\, n_j^{\,2}$, where ε_0 is the vacuum permittivity.

$$\frac{p_0}{n_b^2}\coth\left(p_0\cdot t\right)=\frac{\sigma_0}{n_a^2}\tan\left[\sigma_0\cdot d-\tan^{-1}\left(\frac{q_0}{\sigma_0}\cdot\frac{n_a^2}{n_d^2}\right)\right] \tag{3-35a}$$

Equation 3-35 can be expressed in the explicit form of mode number N.

$$\sigma_0\cdot d=\tan^{-1}\left(\frac{q_0}{\sigma_0}\frac{n_a^2}{n_d^2}\right)+\tan^{-1}\left[\frac{n_a^2}{n_b^2}\frac{p_0}{\sigma_0}\coth\left(p_0\cdot t\right)\right]+N\pi \tag{3-35b}$$

If N=0 in, the waveguide will have single laser beam spot and this is the fundamental mode for this waveguide [27]. For precise applications, we discuss the fundamental mode with single spot in this dissertation.

If both $\frac{n_d^2}{n_a^2}=1$ and $\frac{n_a^2}{n_b^2}=1$, then Equation 3-35 will become the form of TE eigenmode equation, as derived in [Luo 90]. However, the derivation process for TE modes is based on electric fields while the derivation process for TM modes is based on magnetic fields.

As mentioned at the end of section 3.1, Equations 3-23 to 3-27 constitute a linear homogeneous matrix system and can be written in matrix form and the matrix size is 5 by 5. To have an nonzero solution for variables A_0, B_0, C_0, D_0, E_0 in the above equations, the determinant of the coefficient matrix must be zero. By using matrix expansion, we can obtain the same Equation 3-35. The details of this manipulation process by using matrix expansion are given in Appendix B.

3.3 Derivation of the Eigenmode Equation for First-order DFB Corrugated Waveguides by Truncated Floquet-Bloch Formalism

In most practical DFB lasers utilizing first-order diffraction, the condition ka<<1 is satisfied. As a consequence, a truncated Floquet-Bloch formalism [23] is sufficient to compute the backward coupling coefficient (κ). In this case, there are only two types of

traveling waves: the fundamental forward wave (m=0, propagation constant $= \beta_0$) and the backward diffractive wave (m= -1, propagation constant $= -\beta_0$). All other m-waves are evanescent along the z-direction, and are neglected in the following calculation. The first-order DFB condition implies the following:

$$\beta_0 - \overline{\mathrm{K}} = -\beta_0 \quad \Rightarrow \overline{\mathrm{K}} = 2\beta_0 \tag{3-33}$$

As mentioned previously, ten equations are needed to describe first-order DFB. Five equations are for m = 0, and five equations are for m= -1. Four of the five m = 0 equations are Equations 3-23 to 3-26 and four of the 5 m = -1 equations are Equations 3-34 to 3-37. Ten equations are listed together in the following for the completeness of this first –order DFB model:

$$B_0 - D_0 \cdot \exp\left(p_0 t\right) - E_0 \cdot \exp\left(-p_0 t\right) = 0 \tag{3-23}$$

$$B_{-1} - D_{-1} \cdot \exp\left(p_{-1} t\right) - E_{-1} \cdot \exp\left(-p_{-1} t\right) = 0 \tag{3-34}$$

$$\left(\frac{\sigma_0}{\varepsilon_a}\right) C_0 - \left(\frac{p_0}{\varepsilon_b}\right) D_0 \cdot \exp\left(p_0 t\right) + \left(\frac{p_0}{\varepsilon_b}\right) E_0 \cdot \exp\left(-p_0 t\right) = 0 \tag{3-24}$$

$$\left(\frac{\sigma_{-1}}{\varepsilon_a}\right) C_{-1} - \left(\frac{p_{-1}}{\varepsilon_b}\right) D_{-1} \cdot \exp\left(p_{-1} t\right) + \left(\frac{p_{-1}}{\varepsilon_b}\right) E_{-1} \cdot \exp\left(-p_{-1} t\right) = 0 \tag{3-35}$$

$$A_0 - B_0 \cdot \cos\left(\sigma_0 d\right) - C_0 \cdot \sin\left(\sigma_0 d\right) = 0 \tag{3-25}$$

$$A_{-1} - B_{-1} \cdot \cos\left(\sigma_{-1} d\right) - C_{-1} \cdot \sin\left(\sigma_{-1} d\right) = 0 \tag{3-36}$$

$$\left(\frac{q_0}{\varepsilon_d}\right) A_0 - \left(\frac{\sigma_0}{\varepsilon_a}\right) B_0 \cdot \sin\left(\sigma_0 d\right) + \left(\frac{\sigma_0}{\varepsilon_a}\right) C_0 \cdot \cos\left(\sigma_0 d\right) = 0 \tag{3-26}$$

$$\left(\frac{q_{-1}}{\varepsilon_d}\right) A_{-1} - \left(\frac{\sigma_{-1}}{\varepsilon_a}\right) B_{-1} \cdot \sin\left(\sigma_{-1} d\right) + \left(\frac{\sigma_{-1}}{\varepsilon_a}\right) C_{-1} \cdot \cos\left(\sigma_{-1} d\right) = 0 \tag{3-37}$$

Since the Bessel functions of small argument are fast decaying with increasing order, it is sufficient to choose just the n = 0 and n = -1 for Equation 3-22.

$$D_0 I_0\left(p_0 \cdot a\right) + E_0 I_0\left(p_0 \cdot a\right) + D_{-1} I_{-1}\left(p_{-1} \cdot a\right) - E_{-1} I_{-1}\left(p_{-1} \cdot a\right) = 0 \tag{3-38}$$

$$D_0 I_1\left(p_0 \cdot a\right) - E_0 I_1\left(p_0 \cdot a\right) + D_{-1} I_0\left(p_{-1} \cdot a\right) + E_{-1} I_0\left(p_{-1} \cdot a\right) = 0 \tag{3-39}$$

Following the procedure in section 3.2, the above ten linear homogeneous equations will only have a non-trivial solution if the determinant of the coefficient matrix is zero. Manipulating the determinant leads to the following eigenmode equation:

$$\Phi_0 \cdot \Phi_{-1} = \frac{I_0\left(p_0 \cdot a\right) \cdot I_0\left(p_{-1} \cdot a\right)}{I_1\left(p_0 \cdot a\right) \cdot I_1\left(p_{-1} \cdot a\right)} \tag{3-40}$$

where $$\Phi_i = \frac{-1}{\tanh\left\{\tanh^{-1}\left\{\frac{p_i}{\sigma_i}\frac{n_a^2}{n_b^2}\tan\left[\sigma_i \cdot d + \tanh^{-1}\left(\frac{\sigma_i}{q_i}\frac{n_d^2}{n_a^2}\right)\right]\right\} + p_i \cdot t\right\}} \tag{3-41}$$

The details of the manipulation process are given in Appendix C.

If both $\frac{n_d^2}{n_a^2} = 1$ and $\frac{n_a^2}{n_b^2} = 1$, then Equation 3-41 will become the TE eigenmode equation, as derived in [23].

Since we consider shallow grooves, the Bessel functions in Equation 3-40 can be approximated as the following polynomials:

$$\begin{aligned} I_0\left(u\right) &\approx 1 \\ I_1\left(u\right) &\approx \frac{u}{2} \end{aligned} \quad , \text{u<<1} \tag{3-42}$$

3.4 Derivation of the Eigenmode Equation for Second-order DFB Corrugated Waveguides by Truncated Floquet-Bloch Formalism

In most practical DFB lasers utilizing second-order diffraction, the condition of shallow groove, ka<<1, is satisfied. Consequently, a truncated Floquet-Bloch formalism

is sufficient to compute the backward coupling coefficient (κ). In this case, there are three types of traveling waves: the fundamental forward wave (m=0, propagation constant $= \beta_0$), the upward surface emitting wave (m= -1, propagation constant = 0) and the backward diffractive wave (m= -2, propagation constant $= -\beta_0$). All other higher-order m-waves are evanescent along the z-direction, and are neglected in the following calculation. The second-order DFB condition implies the following:

$$\beta_0 - 2\overline{\mathrm{K}} = -\beta_0 \quad \Rightarrow \overline{\mathrm{K}} = \beta_0 \tag{3-43}$$

With the similar procedures discussed in Section 3.3, fifteen linear homogeneous equations are needed to describe this second-order DFB. Five equations are for m = 0, five equations are for m= -1 and five equations are for m=-2. Four of the five m = 0 equations are Equations 3-23 to 3-26, four of the five m = -1 equations are Equations 3-34 to 3-37 and four of the five m = -2 equations are 3-44 to 3-47. Fifteen equations are listed together in the following for the completeness of this second –order DFB model:

$$B_0 - D_0 \cdot \exp\left(p_0 t\right) - E_0 \cdot \exp\left(-p_0 t\right) = 0 \tag{3-23}$$

$$B_{-1} - D_{-1} \cdot \exp\left(p_{-1} t\right) - E_{-1} \cdot \exp\left(-p_{-1} t\right) = 0 \tag{3-34}$$

$$B_{-2} - D_{-2} \cdot \exp\left(p_{-2} t\right) - E_{-2} \cdot \exp\left(-p_{-2} t\right) = 0 \tag{3-44}$$

$$\left(\frac{\sigma_0}{\varepsilon_a}\right) C_0 - \left(\frac{p_0}{\varepsilon_b}\right) D_0 \cdot \exp\left(p_0 t\right) + \left(\frac{p_0}{\varepsilon_b}\right) E_0 \cdot \exp\left(-p_0 t\right) = 0 \tag{3-24}$$

$$\left(\frac{\sigma_{-1}}{\varepsilon_a}\right) C_{-1} - \left(\frac{p_{-1}}{\varepsilon_b}\right) D_{-1} \cdot \exp\left(p_{-1} t\right) + \left(\frac{p_{-1}}{\varepsilon_b}\right) E_{-1} \cdot \exp\left(-p_{-1} t\right) = 0 \tag{3-35}$$

$$\left(\frac{\sigma_{-2}}{\varepsilon_a}\right) C_{-2} - \left(\frac{p_{-2}}{\varepsilon_b}\right) D_{-2} \cdot \exp\left(p_{-2} t\right) + \left(\frac{p_{-2}}{\varepsilon_b}\right) E_{-2} \cdot \exp\left(-p_{-2} t\right) = 0 \tag{3-45}$$

$$A_0 - B_0 \cdot \cos(\sigma_0 d) - C_0 \cdot \sin(\sigma_0 d) = 0 \tag{3-25}$$

$$A_{-1} - B_{-1} \cdot \cos(\sigma_{-1} d) - C_{-1} \cdot \sin(\sigma_{-1} d) = 0 \tag{3-36}$$

$$A_{-2} - B_{-2} \cdot \cos(\sigma_{-2} d) - C_{-2} \cdot \sin(\sigma_{-2} d) = 0 \tag{3-46}$$

$$\left(\frac{q_0}{\varepsilon_d}\right) A_0 - \left(\frac{\sigma_0}{\varepsilon_a}\right) B_0 \cdot \sin(\sigma_0 d) + \left(\frac{\sigma_0}{\varepsilon_a}\right) C_0 \cdot \cos(\sigma_0 d) = 0 \tag{3-26}$$

$$\left(\frac{q_{-1}}{\varepsilon_d}\right) A_{-1} - \left(\frac{\sigma_{-1}}{\varepsilon_a}\right) B_{-1} \cdot \sin(\sigma_{-1} d) + \left(\frac{\sigma_{-1}}{\varepsilon_a}\right) C_{-1} \cdot \cos(\sigma_{-1} d) = 0 \tag{3-37}$$

$$\left(\frac{q_{-2}}{\varepsilon_d}\right) A_{-2} - \left(\frac{\sigma_{-2}}{\varepsilon_a}\right) B_{-2} \cdot \sin(\sigma_{-2} d) + \left(\frac{\sigma_{-2}}{\varepsilon_a}\right) C_{-2} \cdot \cos(\sigma_{-2} d) = 0 \tag{3-47}$$

Since the Bessel functions of small argument are fast decaying with increasing order, it is sufficient to choose just the n = 0, n = -1 and n= -2 for Equation 3-22.

$$D_0 I_0(p_0 \cdot a) + E_0 I_0(p_0 \cdot a) + D_{-1} I_{-1}(p_{-1} \cdot a) - E_{-1} I_{-1}(p_{-1} \cdot a)$$
$$+ D_{-2} I_{-2}(p_{-2} \cdot a) + E_{-2} I_{-2}(p_{-2} \cdot a) = 0 \tag{3-48}$$

$$D_0 I_1(p_0 \cdot a) - E_0 I_1(p_0 \cdot a) + D_{-1} I_0(p_{-1} \cdot a) + E_{-1} I_0(p_{-1} \cdot a)$$
$$+ D_{-2} I_{-1}(p_{-2} \cdot a) - E_{-2} I_{-1}(p_{-2} \cdot a) = 0 \tag{3-49}$$

$$D_0 I_2(p_0 \cdot a) + E_0 I_2(p_0 \cdot a) + D_{-1} I_1(p_{-1} \cdot a) - E_{-1} I_1(p_{-1} \cdot a)$$
$$+ D_{-2} I_0(p_{-2} \cdot a) + E_{-2} I_0(p_{-2} \cdot a) = 0 \tag{3-50}$$

These fifteen equations form a 15 by 15 matrix and leads to the following eigenmode equation:

$$I_0(p_{-1} \cdot a)\left[I_0(p_0 \cdot a) \cdot I_0(p_{-2} \cdot a) - I_2(p_0 \cdot a) \cdot I_2(p_{-2} \cdot a)\right]$$
$$= I_1(p_{-1} \cdot a) \cdot \Phi_{-1} \left\{ I_1(p_0 \cdot a) \cdot \left[I_0(p_{-2} \cdot a) - I_2(p_{-2} \cdot a)\right] \cdot \Phi_0 \right.$$

$$+I_1\left(p_{-2}\cdot a\right)\cdot\left[I_0\left(p_0\cdot a\right)-I_2\left(p_0\cdot a\right)\right]\cdot\Phi_{-2}\Big\} \tag{3-51}$$

where Φ_i is shown in equation (3-41) and $i=0$, -1, -2.

The details of the manipulation process are much more vigorous but similar to Appendix C.

If both $\frac{n_d^2}{n_a^2}=1$ and $\frac{n_a^2}{n_b^2}=1$, then Equation 3-51 will become the TE eigenmode equation, as derived in [23].

Equation 3-51 is a neat closed-form expression for second-order DFB simulation. Since we consider shallow grooves, the Bessel functions in Equation 3-51 can be approximated as the following polynomials:

$$\begin{aligned} I_0\left(u\right) &\approx 1+\frac{u^2}{4} \\ I_1\left(u\right) &\approx \frac{u}{2} \qquad\qquad \text{, u<<1} \\ I_2\left(u\right) &\approx \frac{u^2}{8} \end{aligned} \tag{3-52}$$

CHAPTER 4
CALCULATION METHODOLOGY AND RESULTS

4.1 Methodology

In modeling corrugated DFB semiconductor lasers, the backward diffraction coupling coefficient kappa (κ) replaces the end mirror reflectivity used to determine the threshold current requirement in conventional lasers. Figure 4-1 shows waveguide with corrugated grating. The incident power (P) comes into and propagates along this corrugated structure. During this process, the incident power will generate transmitted power (TP) and reflected power (RP) with reflection coefficient $R = \tanh^2(\kappa L)$ [28].

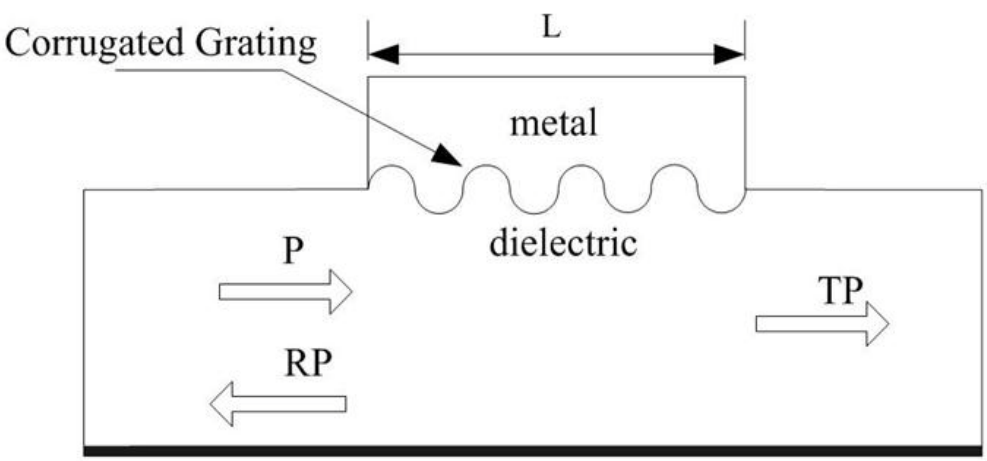

Figure 4-1. The coupling coefficient (κ) and reflection

For dielectric/dielectric gratings, coupled mode perturbation theory is normally used to calculate κ using the overlap integral of the product of the square of the index perturbation Δn with the square of the electric field mode function E(x): $\kappa \propto \int \Delta n^2(x) E^2(x) dx$ [29]. However, this method cannot be used for metal/dielectric gratings because of the very large index perturbation at the metal/dielectric interface and the uncertainty on how to choose the unperturbed waveguide [30] [31]. In addition, since the electric field is essentially zero in the metal, the overlap concept cannot even

be defined. Figure 4-2 shows a method that can be used to calculate κ for metal/dielectric gratings is called the Floquet-Bloch formalism [23].

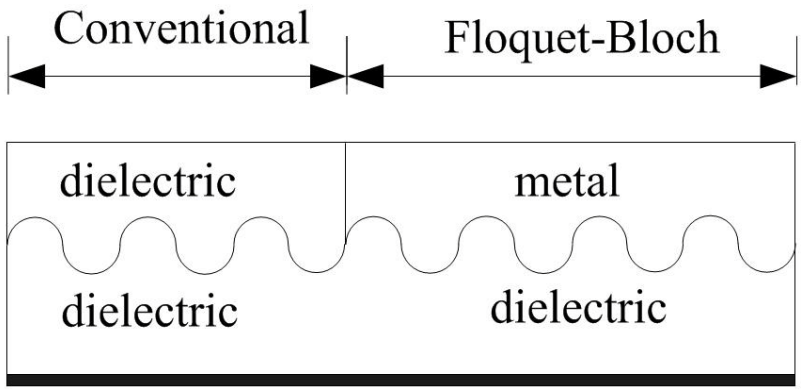

Figure 4-2. Floquet-Bloch formalism for calculating κ of metal/dielectric corrugated structures

In the Floquet-Bloch formalism, one expands the eigenmode solutions to the waveguide equation in each layer of the waveguide into an infinity numbers of forward–going plane and backward-going plane waves. Since most of the waves in the expansion are evanescent and decay rapidly in the wave direction, one only needs to consider the traveling wave terms to get good accuracy for κ in the DFB problem. This approach is called truncated Floquet-Bloch formalism (TFBF), by choosing the most significant terms and neglecting the fast-decaying terms in order to have a well-balanced trade-off of considering between effectiveness and efficiency during modeling process.

This approach has been used to construct models for the fundamental transverse electric waveguide mode (TE_0) in planar, first-order DFB and second-order DFB waveguides [23]. In this work, the truncated Floquet-Bloch formalism is extended to the more complex transverse magnetic waveguide mode (TM_0) problem since QCLs only lase on this type of mode [3].

The procedures of truncated Floquet-Bloch formalism include two major parts. The first part is to use Maxwell's equations to derive a wave equation for the transverse magnetic field in a planar metal-clad waveguide. This part includes: solving the wave equation and obtaining the solutions in each layer, applying boundary conditions at the layer-interfaces and finally determine the eigenmode equation and solve for the propagation constant β_0 for the fundamental TM mode (TM_0). The second part is to convert the planar waveguide into a corrugated waveguide by applying a sinusoidal corrugation at the metal-dielectric interface. This part includes: using the TM_0 mode of the planar waveguide problem to form an infinite plane wave expansion for the transverse magnetic field in each layer of the corrugated waveguide, select the type of DFB (first-order or second-order), keeping the terms in the plane wave expansion associated with the type of DFB and ignore the evanescent wave terms, applying boundary conditions at the layer-interfaces and obtain a set of linear homogeneous equations where the coefficients are functions of β, using linear algebra to transform the equation set into a coefficient matrix describing this corrugated waveguide system, using the coefficient matrix equation to derive a transcendental equation for β and finally solving the coefficient matrix equations numerically to find $\tilde{\beta} = \beta_0 \pm i\kappa$, where κ is the imaginary part of conjugated complex propagation constant $\tilde{\beta}$ and κ is also the DFB coupling coefficient.

Figure 4-3 shows the $\omega - \beta$ dispersion diagram for DFB corrugated waveguides. The period of the DFB corrugated waveguide introduces the stop band $\Delta\omega$ at the Bragg frequency π/Λ [23]. Then the propagation constant becomes complex and has a

imaginary part. This concept is similar to energy-wavevector (E-k) diagram [32] for the electron energy states in the periodic lattice of semiconductors [33].

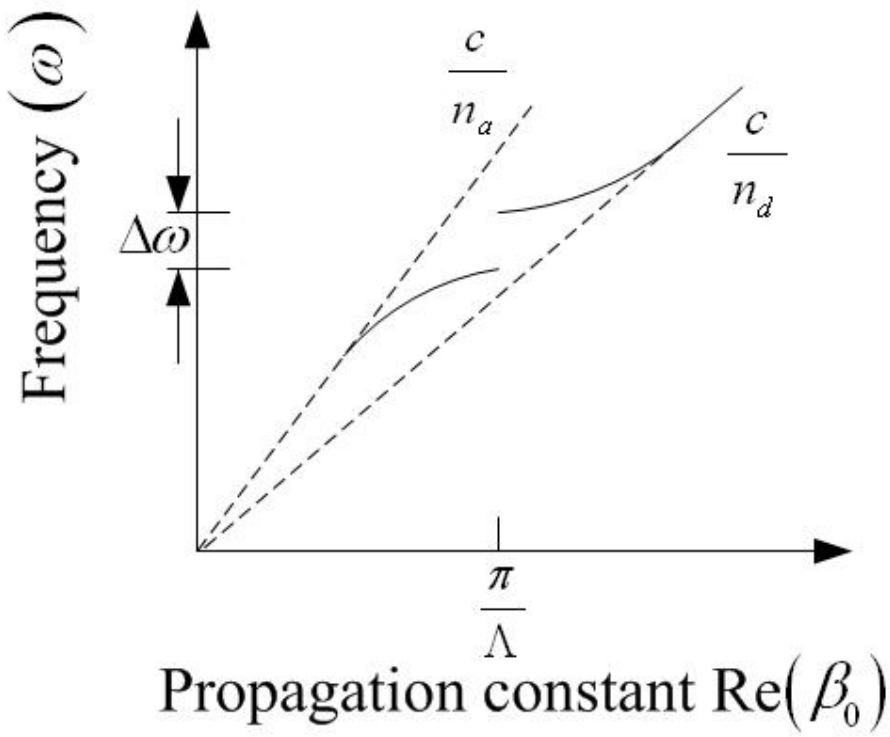

Figure 4-3. ω-β dispersion diagram for DFB

This stop band of this ω-β dispersion curve can show the interaction between the periodic corrugation and optical mode. The magnitude of this stop band has the following relationship between κ and $\Delta\omega$ by coupled mode theory [34]:

$$\kappa = \frac{n_e}{2c} \cdot \Delta\omega \tag{4-1}$$

where c is the velocity of light in vacuum and n_e is the effective refractive index for waveguides.

Coupling coefficient κ in Equation 4-1 can be expressed by the imaginary part of complex propagation constant $\tilde{\beta}$ for the corrugated waveguides:

$$\kappa = \frac{n_e}{2c}\cdot\left(2\pi\cdot\Delta f\right) = \frac{1}{2}\cdot 2\pi\cdot\frac{\Delta f}{c}\cdot n_e = \frac{1}{2}\cdot 2\pi\cdot\left(\frac{1}{\lambda_1}-\frac{1}{\lambda_2}\right)\cdot n_e = \frac{1}{2}\cdot\Delta k\cdot n_e$$
$$= \frac{1}{2}\cdot\Delta\tilde{\beta} = \frac{1}{2}\left\|\left[\beta_0 + \mathrm{Im}\left(\tilde{\beta}\right)\right] - \left[\beta_0 - \mathrm{Im}\left(\tilde{\beta}\right)\right]\right\| = \mathrm{Im}\left(\tilde{\beta}\right) \tag{4-2}$$

where $\Delta f = f_1 - f_2$, $f_1 = c/\lambda_1$ and $f_2 = c/\lambda_2$

Coupling coefficient κ in Equation 4-2 can be expressed by the function of wavelengths:

$$\kappa = \frac{1}{2}\cdot 2\pi\cdot\left(\frac{1}{\lambda_1}-\frac{1}{\lambda_2}\right)\cdot n_e = \pi\cdot\frac{\lambda_2-\lambda_1}{\lambda_1\lambda_2}\cdot n_e = \pi\cdot\frac{\left(\lambda+\frac{\Delta\lambda}{2}\right)-\left(\lambda+\frac{\Delta\lambda}{2}\right)}{\left(\lambda+\frac{\Delta\lambda}{2}\right)\left(\lambda-\frac{\Delta\lambda}{2}\right)}\cdot n_e$$
$$= \pi\cdot\frac{\Delta\lambda}{\lambda^2-\frac{1}{4}\left(\Delta\lambda\right)^2}\cdot n_e \approx \pi\cdot\frac{\Delta\lambda}{\lambda^2}\cdot n_e \tag{4-3}$$

where $\Delta\lambda = \lambda_2 - \lambda_1$, $\lambda_2 = \lambda + \frac{\Delta\lambda}{2}$ and $\lambda_1 = \lambda - \frac{\Delta\lambda}{2}$

4.2 Computation

In Chapter 3, we developed mathematical models for planar waveguides and corrugated waveguides. Figure 4-4 shows the flow chart to compute coupling coefficient. Flow chart is a useful tool [35] to organize the logic of computer codes to iteratively search the complex propagation constant and the complicated optical coupling calculation. MATLAB® software [36] with numerical concepts [37] is used to write the computer codes to find the complex propagation constant and plot the figures. The imaginary part of this complex propagation constant is the coupling coefficient.

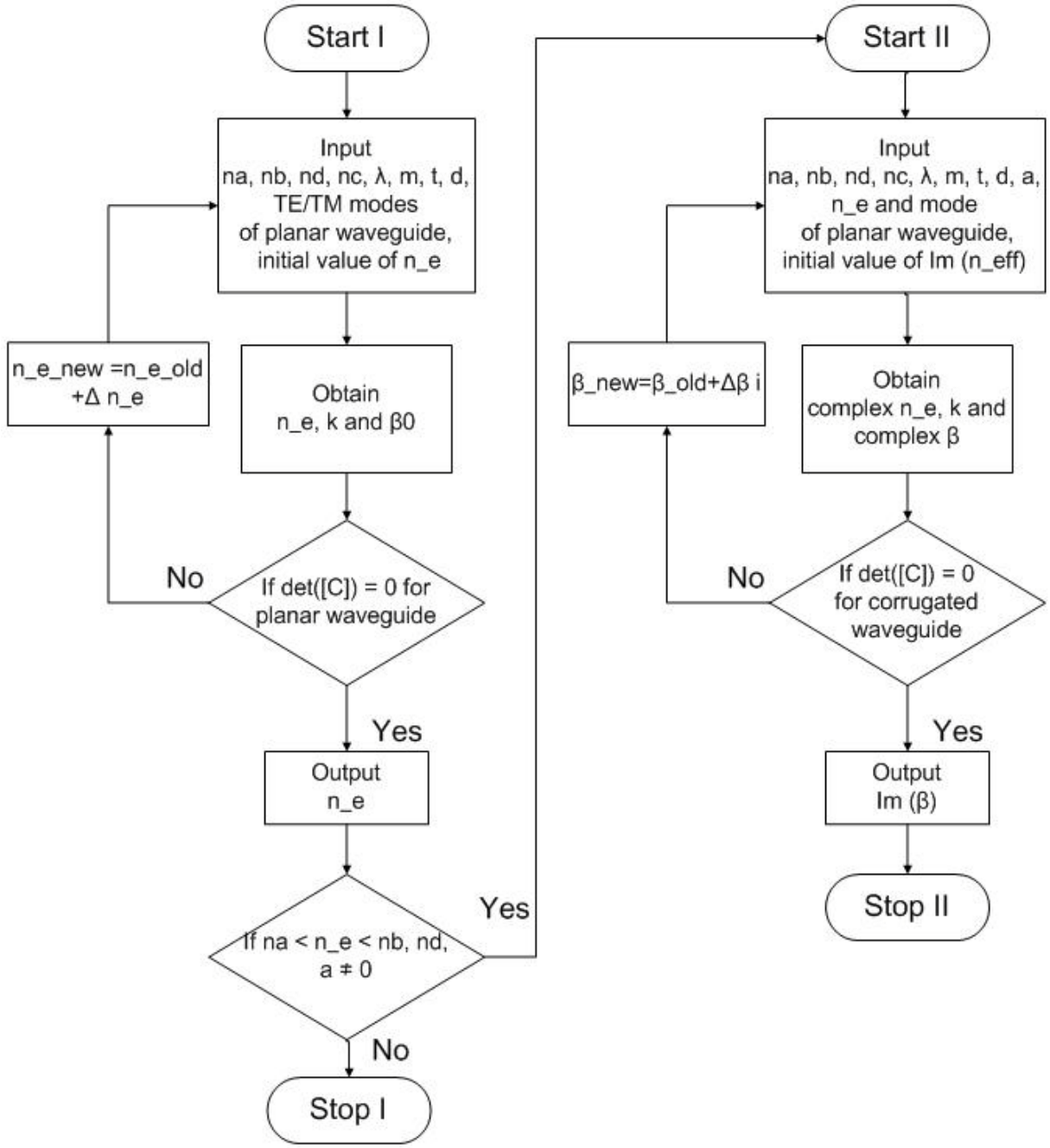

Figure 4-4. Flow chart to compute coupling coefficient (κ)

Figure 4-5 shows an example of plotting the value of the determinant of coefficient matrix or the eigenmode equation 3-41 versus complex propagation constant for a corrugated waveguides with normalized corrugation amplitude ka=0.5 on TE mode.

The value on the z-axis equal to zero will be the solution for the eigenmode equation3-41. An algorithm to search a solution in a zig-zag way on complex plan of propagation constant is not very efficient. Figure 4-5 can visualize how the equations varied with the propagation constant so that we can narrow down to the possible neighborhood where the solution point is.

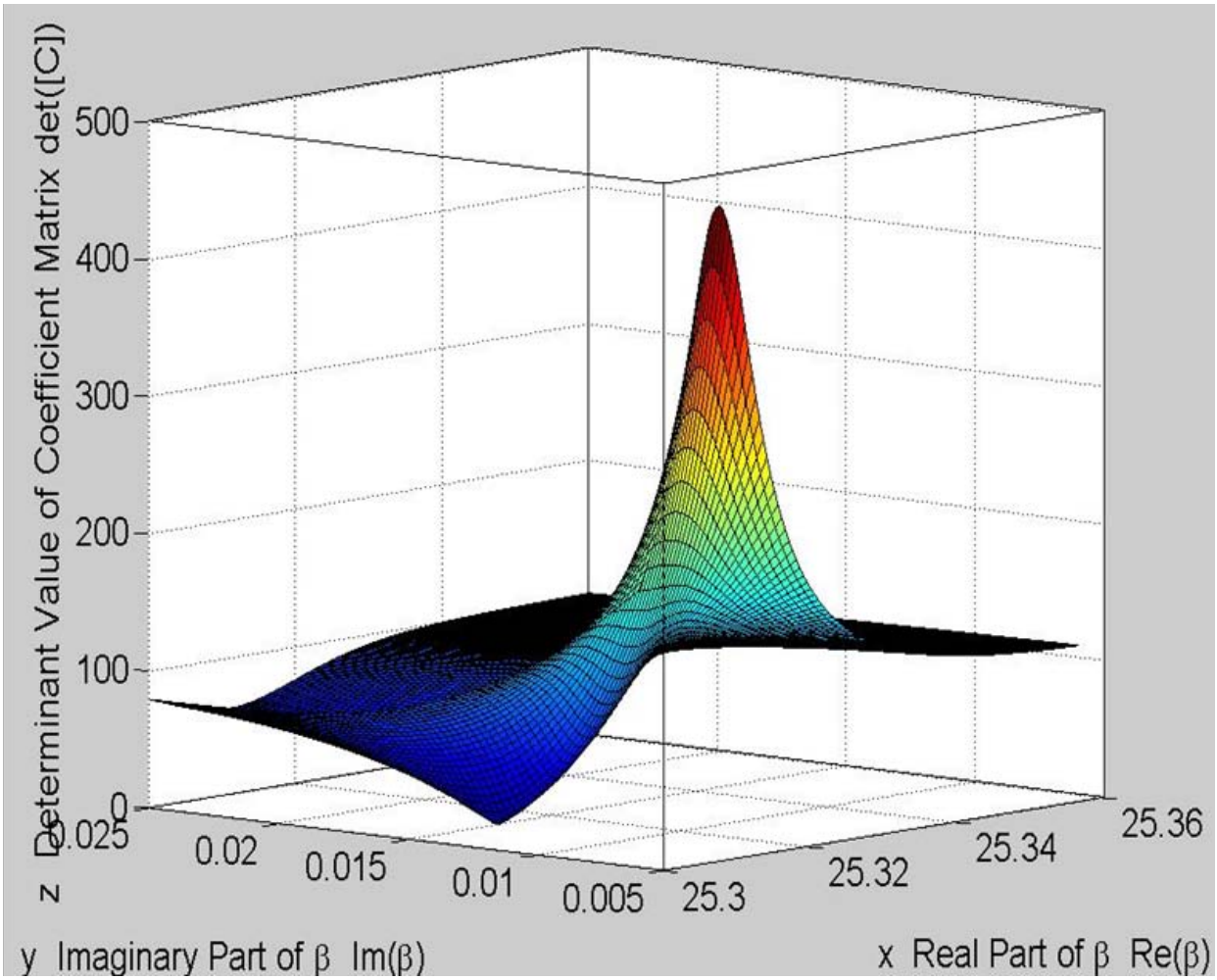

Figure 4-.5 An example showing the value of eigenmode equations versus propagation constant when ka=0.5

Figure 4-6 shows the zoom-in plot for the point with zero value on the z-axis in Figure 4-5. In Figure 4-6, the x-z plan shows the eigenmode equation has zero value when the real part of complex propagation constant has the value 25.3109. Figure 4-6,

the y-z plan shows the eigenmode equation has zero value when the imaginary part of complex propagation constant has the value 0.0146 [1/µm] or 146 [1/cm]. The x-y plane is the complex plan for propagation constant.

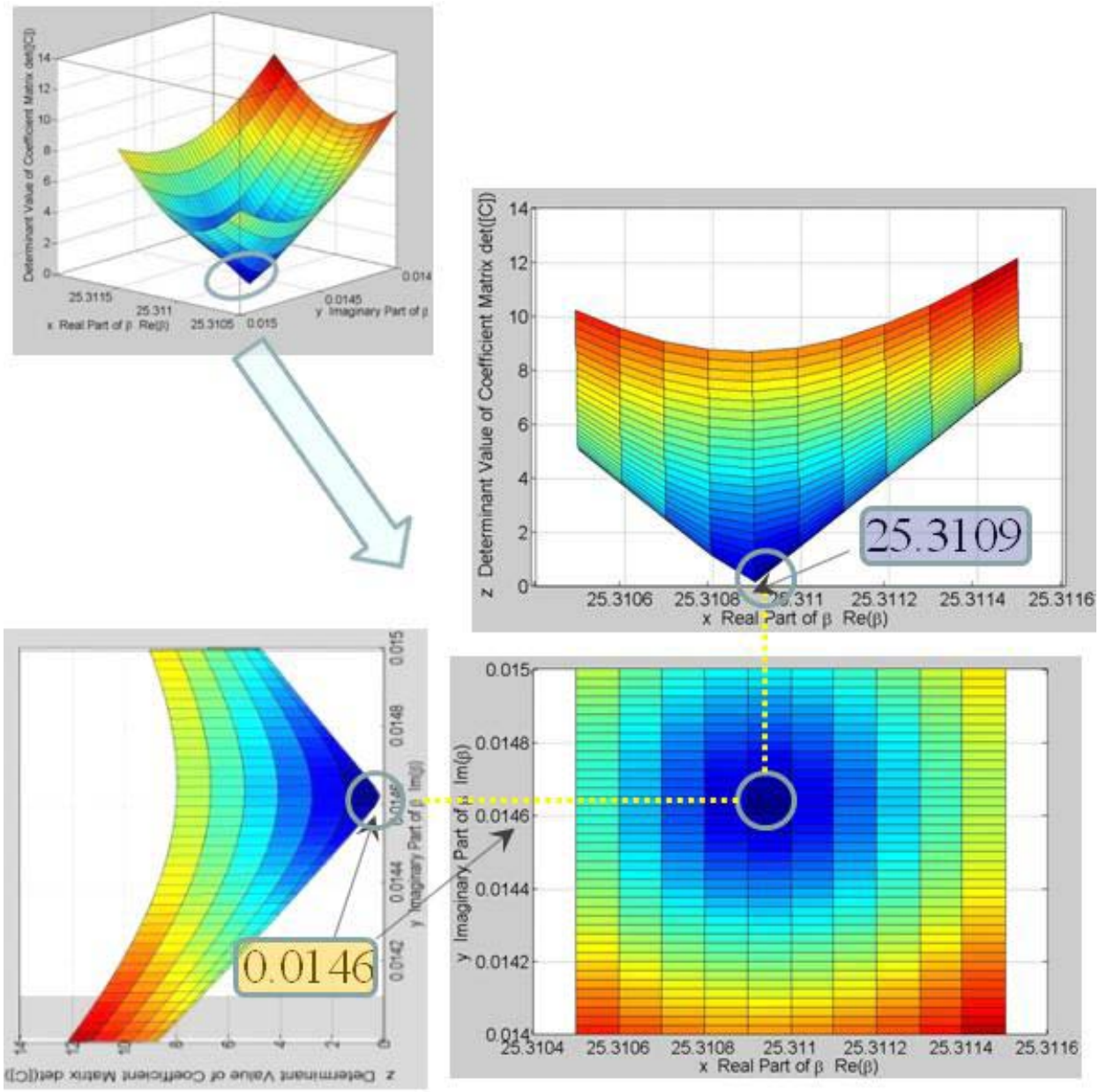

Figure 4-6. Solution search to compute coupling coefficient (κ) when ka=0.5

4.3 Numerical Results and Discussions

Figure 4-7 shows the coupling coefficient versus the corrugation amplitude for 1st-order DFB for TM_0 and TE_0 modes. The curve with circle in this figure is named as TM-1 (ModA), which means TM mode- first order DFB (Model A by using models in Chapter 3). The waveguide use the following parameters: $\lambda = 850nm$, active layer thickness $d = 100nm$, buffer layer thickness $t = 300nm$. For lasers made of GaAs/AlGaAs materials, they have typical values of active layer refractive index $n_a = 3.6$ and buffer/cladding layer refractive index $n_b = n_d = 3.4$. Larger corrugation amplitude will cause larger perturbation so the coupling effect will become larger. The TM mode will have more interaction with corrugated metal so its coupling coefficient is larger than TE coupling coefficient.

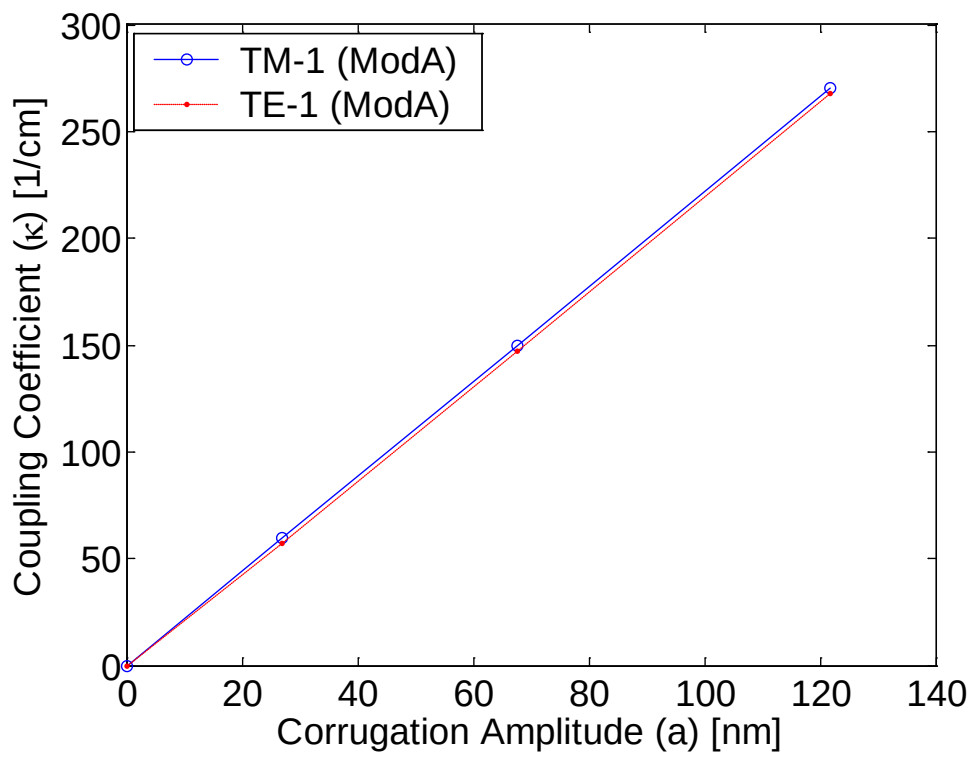

Figure 4-7. Coupling coefficient (κ) vs. corrugation amplitude (a)

Figure 4-8 shows the coupling coefficient versus the buffer layer thickness for 1st-order DFB for TM_0 and TE_0 modes. The waveguides use the following parameters: the normalized corrugation amplitude ka=0.2, $\lambda = 850nm$, active layer thickness $d = 100nm$, the refractive indices are $n_a = 3.6$ and $n_b = n_d = 3.4$.

If we reduce the buffer thickness, the mode will interact with corrugation more and the coupling coefficient would become larger. After reaching the maximum coupling coefficient, there is a roll-over due to the mismatch of the mode. After the roller-over the curves will have a cut-off point on their left-most end when the effective refractive index reaches 3.4 in this case.

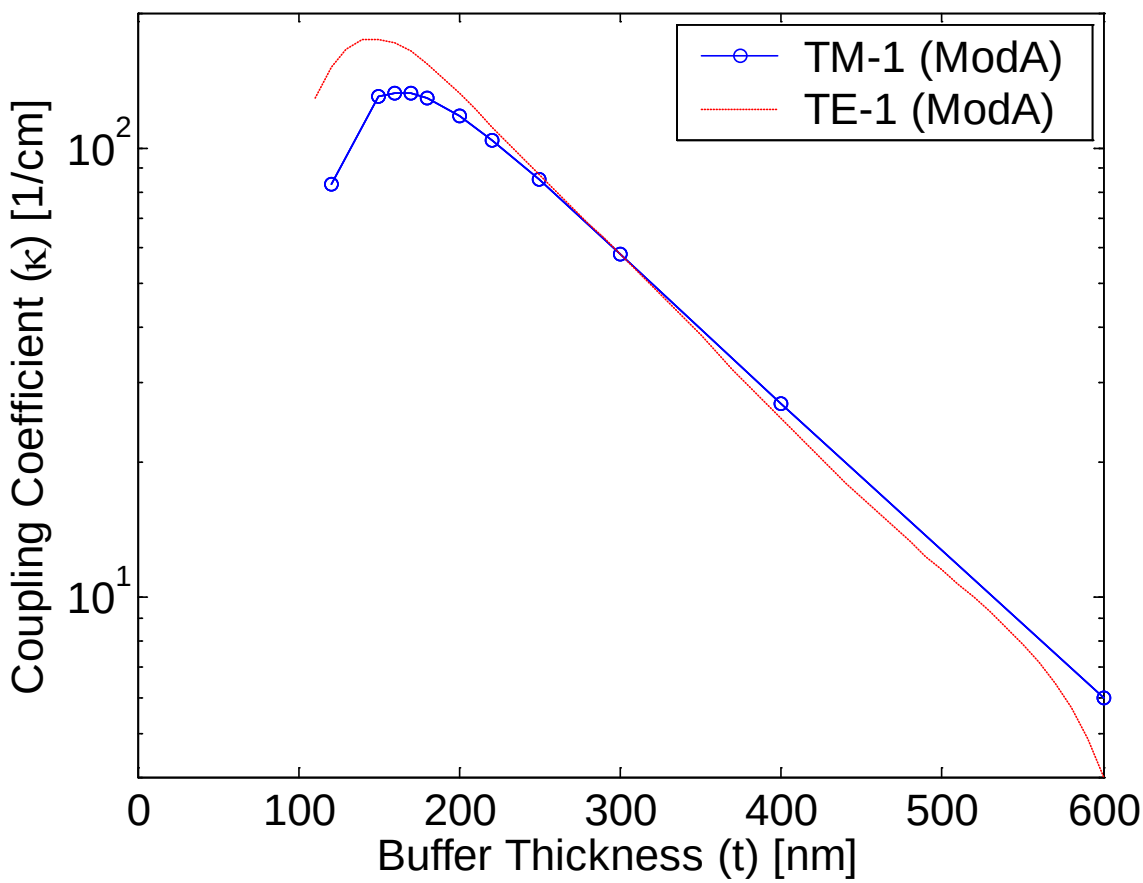

Figure 4-8. Coupling coefficient (κ) vs. buffer thickness (t)

Figure 4-8 shows the coupling coefficient versus the active layer thickness for 1st-order DFB for TM_0 and TE_0 modes. The waveguides use the following parameters: the normalized corrugation amplitude ka=0.2, $\lambda = 850nm$, active layer thickness $d = 100nm$, buffer layer thickness $t = 300nm$. The refractive indices are $n_a = 3.6$ and $n_b = n_d = 3.4$.

The curves in Figure 4-9 for active layer thickness variation has similar trend with the curve in Figure 4-8 for buffer layer variation.

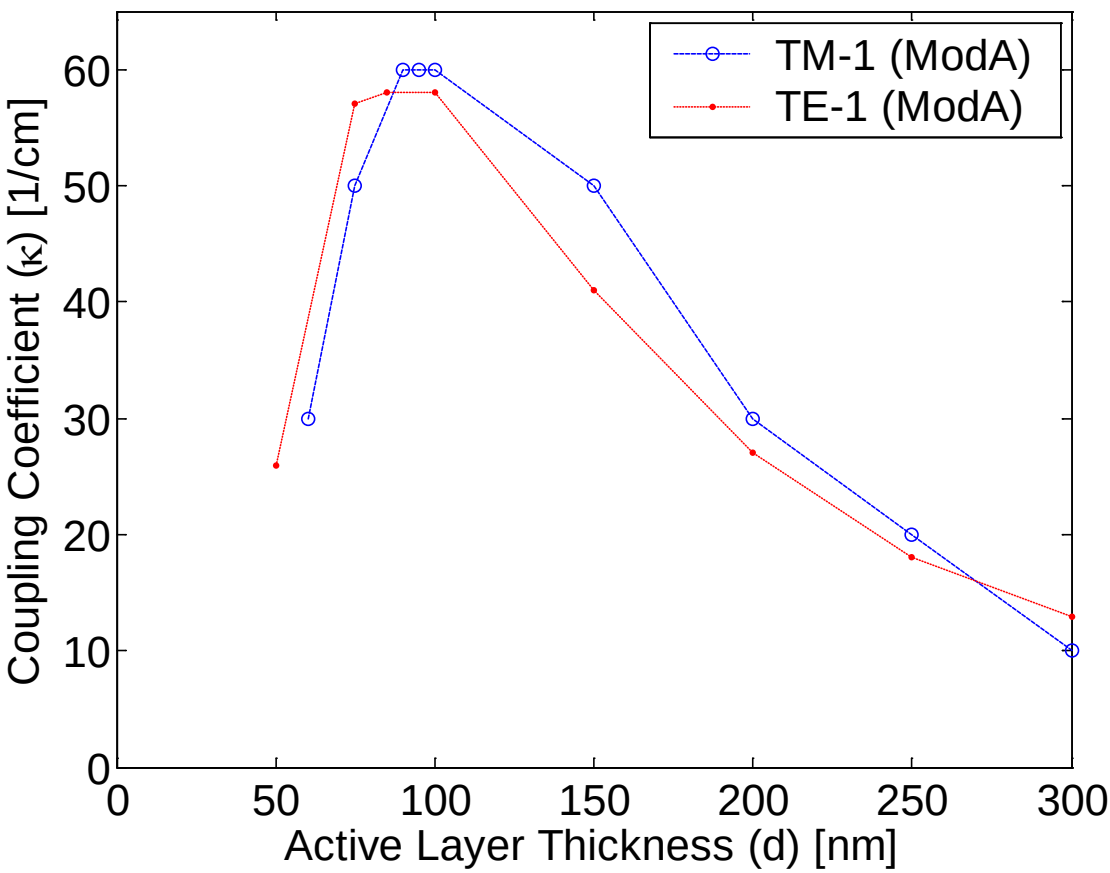

Figure 4-9. Coupling coefficient (κ) vs. active layer thickness (t)

CHAPTER 5
MODIFED MODELS CONSIDERING REAL METALS

5.1 Full Floquet-Bloch Formalism for Real Metals

In Chapter 3, we assume the magnetic field is zero inside the perfect metal layer. To be more precisely model different real metal, the fields inside the metal is not zero. Figure 5-1 shows a semiconductor laser structure with a perfect metal sinusoidally corrugated contact layer. The metal layer has a complex refractive index n_c.

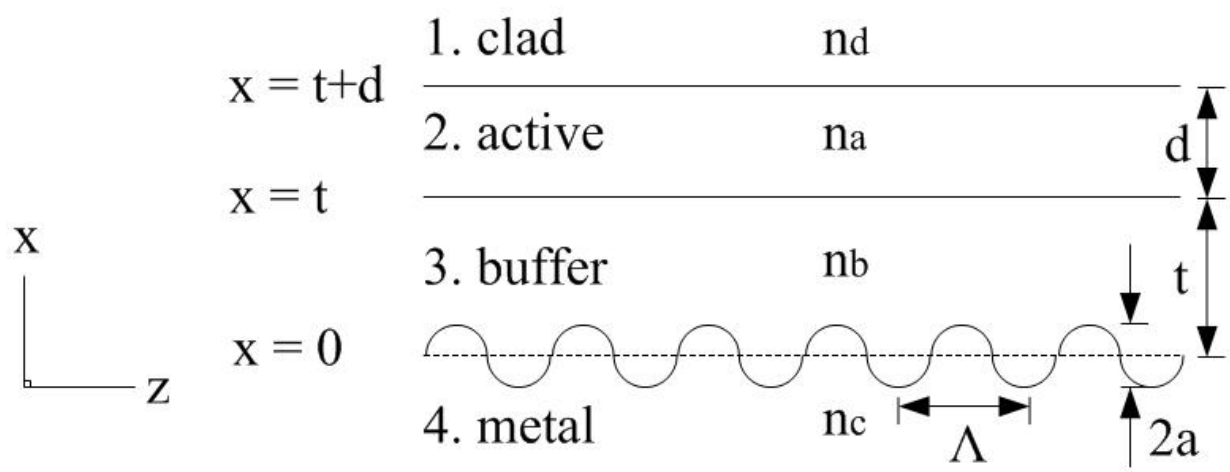

Figure 5-1. The DFB laser structure with real metal contact

TM modes in such structure have their magnetic field pointing in the y direction. The coordinate system chosen has x = 0 at the interface of metal and semiconductor to simplify equations and computations. The Floquet-Bloch formalism requires that the magnetic field in each layer, cladding layer (H_d), active layer (H_a), buffer layer (H_b), and metal layer (H_c), be expanded in a plane wave series as follows:

$$H_d(x,z) = \sum_{m=-\infty}^{\infty} A_m \cdot \exp\left[-q_m\left(x-t-d\right)\right] \cdot \exp\left(-i\beta_m z\right) \tag{5-1}$$

$$H_a(x,z) = \sum_{m=-\infty}^{\infty} \left\{B_m \cdot \cos\left[\sigma_m\left(x-t\right)\right] + C_m \cdot \sin\left[\sigma_m\left(x-t\right)\right]\right\} \cdot \exp\left(-i\beta_m z\right) \tag{5-2}$$

$$H_b(x,z) = \sum_{m=-\infty}^{\infty} \left\{D_m \cdot \exp\left(p_m x\right) + E_m \cdot \exp\left(-p_m x\right)\right\} \cdot \exp\left(-i\beta_m z\right) \tag{5-3}$$

$$H_c(x,z) = \sum_{m=-\infty}^{\infty} F_m \cdot \exp\left[-qc_m\left(-x\right)\right] \cdot \exp\left(-i\beta_m z\right) \tag{5-4}$$

where $\beta_m = \beta_0 + m\overline{\mathrm{K}} = \beta_0 + m\left(\frac{2\pi}{\Lambda}\right)$ (5-5)

$$\sigma_m = \sqrt{n_a{}^2 k^2 - \beta_m{}^2} \tag{5-6}$$

$$p_m = \sqrt{\beta_m{}^2 - n_b{}^2 k^2} \tag{5-7}$$

$$q_m = \sqrt{\beta_m{}^2 - n_d{}^2 k^2} \tag{5-8}$$

$$qc_m = \sqrt{\beta_m{}^2 - n_c{}^2 k^2} \tag{5-9}$$

$$k = \frac{2\pi}{\lambda} \tag{5-10}$$

In the above equations parameters are defined in Chapter 3, β is the wave propagation constant, m is the index for the grating diffraction order, Λ is the grating period, λ is the vacuum wavelength, k is the wave vector and $\overline{\mathrm{K}}$ = 2π / λ is called the grating vector. The field is not zero for real metals [38][39].

For TM modes, the tangential component of the magnetic field (H_y) and the tangential component of the electric field (E_z) must be continuous at the layer interfaces. The E_z continuous condition can be converted to the condition that $\frac{\partial H_y}{\partial x}$ is continuous using the following Maxwell Equation:

$$\nabla \times \vec{H} = \varepsilon \frac{\partial \vec{E}}{\partial t} \tag{5-10}$$

The result for E_z is

$$E_z = \frac{i}{\omega \varepsilon_j} \frac{\partial H_y}{\partial x} \tag{5-11}$$

where ε_j is the medium permittivity in each layer j and ω is the circular frequency.

Therefore, the tangential component boundary conditions are equivalent to saying H_y and $\frac{\partial H_y}{\partial x}$ must be continuous at the following three interfaces: (1) x=t ; (2) x= t+d; (3) x = 0. By using the similar manipulation process to satisfy the above boundary condition, we can obtain a liner homogeneous matrix system with variables: A_m, B_m, C_m, D_m, E_m . F_m The number of equations is equal to the number of variables. To have a nontrivial solution for this system, the determinant of the coefficient matrix for magnetic field should be zero.

We will discuss three special cases: planar, first-order DFB and second-order DFB waveguides for TM modes. The eigenmode equation for the planar waveguides (grating depth 2a= 0) is derived by setting m=0 in Equations 5-1 to 5-10. These six equations form a 6 by 6 matrix, as shown in Appendix D. The eigenmode equation for first-order DFB waveguides is derived by setting m= 0 and m= -1 in the above equations. This is valid because all the other m-waves are evanescent. In this case, these twelve equations form a 12 by 12 matrix, as shown in Appendix E. The eigenmode equation for second-order DFB waveguides is derived by setting m= 0, m= -1, and m= -2 in the above equations. This is valid because all the other m-waves are evanescent. In this case, these eighteen equations form a 18 by 18 matrix. In the next section, we will also compare results (curves) of TM with results of TE. To derive TE models, electric fields are used in planar wave expression by using TFBT [23]. However, [23] did not consider the electric field by using TFBT. In this work, we consider real metals have decay electric fields from the corrugation interface [38]. Then, the matrix size for TE modes would become 6 by 6 for planar, 12 by 12 for first-order DFB, 18 by 18 for second-order waveguides.

5.2 Numerical Results and Discussions

For convenience, we will use Model B (ModB) for the models in Chapter 5 using the non-zero fields inside the metal layer. In Chapter 3, the models are named Model A (Mod A). Figure 5-2 shows the coupling coefficient versus the corrugation amplitude for first-order DFB for TM_0 and TE_0 modes. The curve with diamond points in this figure is named as TM-1 (ModB), which means TM mode- first order DFB (Model B by using models in Chapter 5). The waveguide use the following parameters: $\lambda = 850nm$, active layer thickness $d = 100nm$, buffer layer thickness $t = 300nm$, for GaAs/AlGaAs materials, active layer refractive index $n_a = 3.6$ and buffer/cladding layer refractive index $n_b = n_d = 3.4$.

Larger corrugation amplitude will cause larger perturbation so the coupling effect will become larger. The TM mode will have more interaction with corrugated metal so its coupling coefficient is larger than TE coupling coefficient. The coupling coefficient of TM-1 (ModB) is larger than TM-1 (ModA). Because TM Model B consider the non-zero magnetic field at the corrugated interface between the dielectric buffer layer and metal layer so the interaction at this interface is bigger than TM Model A which approximate the magnetic field inside the metal as zero.

For the curve TE-1 (ModA) means the electric field inside the metal is zero but it is the exact situation to perfect metal. The curve named TE-1 (ModB) considers the real metal with electric field inside the metal. Since the real metal has lower diffraction efficiency at this corrugated interface, the field interaction at this interface is smaller than the perfect metal with higher diffraction efficiency. Thus, the coupling coefficient of TE-1 (ModA) is larger than TE-1 (ModB).

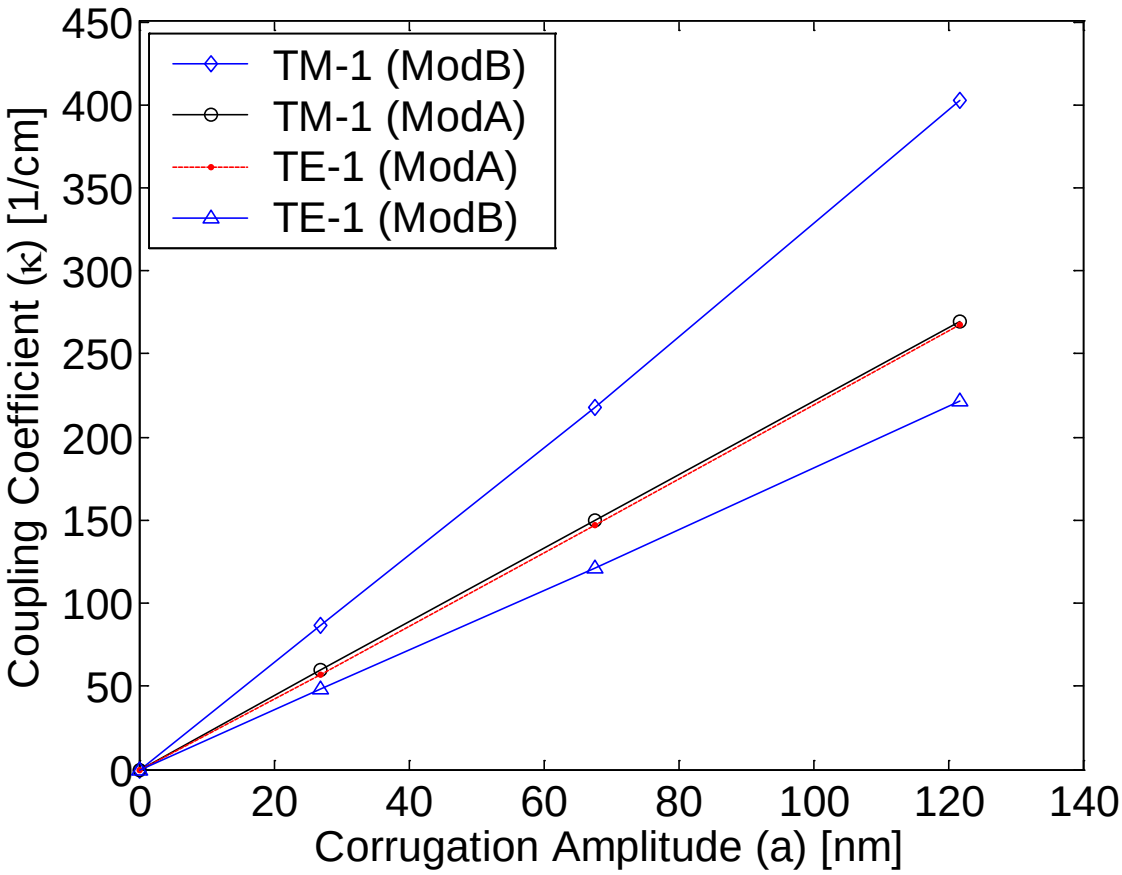

Figure 5-2. Coupling coefficient (κ) vs. corrugation amplitude (a)

Figure 5-3 shows the coupling coefficient versus the buffer layer thickness for 1st-order DFB for Model A and Model B, operating on TM_0 modes. The waveguides use the following parameters: the normalized corrugation amplitude ka=0.2, $\lambda = 850nm$, active layer thickness $d = 100nm$, the refractive indices are $n_a = 3.6$ and $n_b = n_d = 3.4$.

If we reduce the buffer thickness, the mode will interact with corrugation more and the coupling coefficient would become larger. After reaching the maximum coupling coefficient , there is a roll-over due to the mismatch of the mode. After the roller-over the curves will have a cut-off point on their left-most end when the effective refractive index reaches 3.4 in this case.

The coupling coefficient outside the roll-over region of TM-1 (ModB) is larger than the coupling coefficient of TM-1 (ModA). Because TM Model B consider the non-zero magnetic field at the corrugated interface between the dielectric buffer layer and metal layer so the interaction at this interface is bigger than TM Model A which approximate the magnetic field inside the metal as zero. ModA and B has close value of maximum coupling coefficient. Coupling coefficient calculated by ModA and ModB have close change rate with respect to the buffer thickness

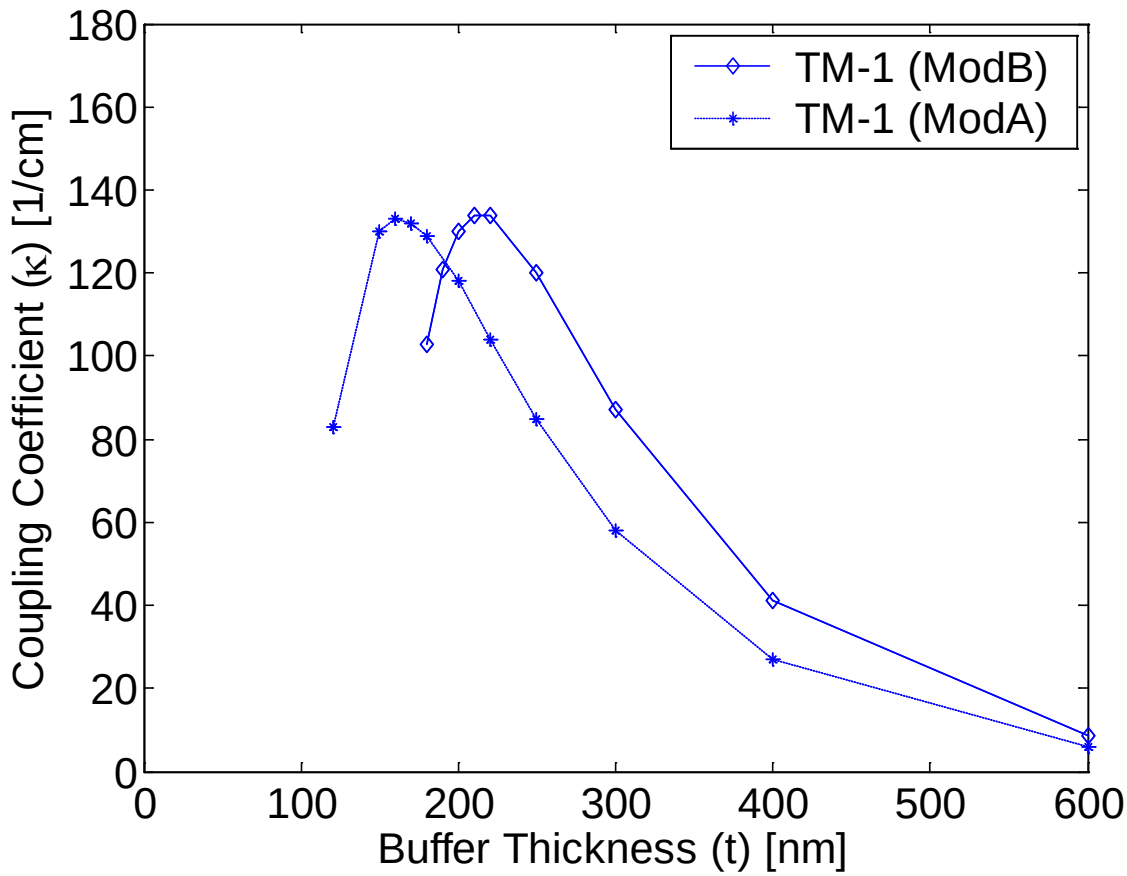

Figure 5-3. Coupling coefficient (κ) vs. buffer thickness (t)

Figure 5-4 shows the coupling coefficient versus the buffer layer thickness for 1st-order DFB for Model B, operating on TM_0 and TE_0 modes. The waveguides use the

following parameters: the normalized corrugation amplitude ka=0.2, $\lambda = 850nm$, active layer thickness $d = 100nm$, the refractive indices are: $n_a = 3.6$ and $n_b = n_d = 3.4$.

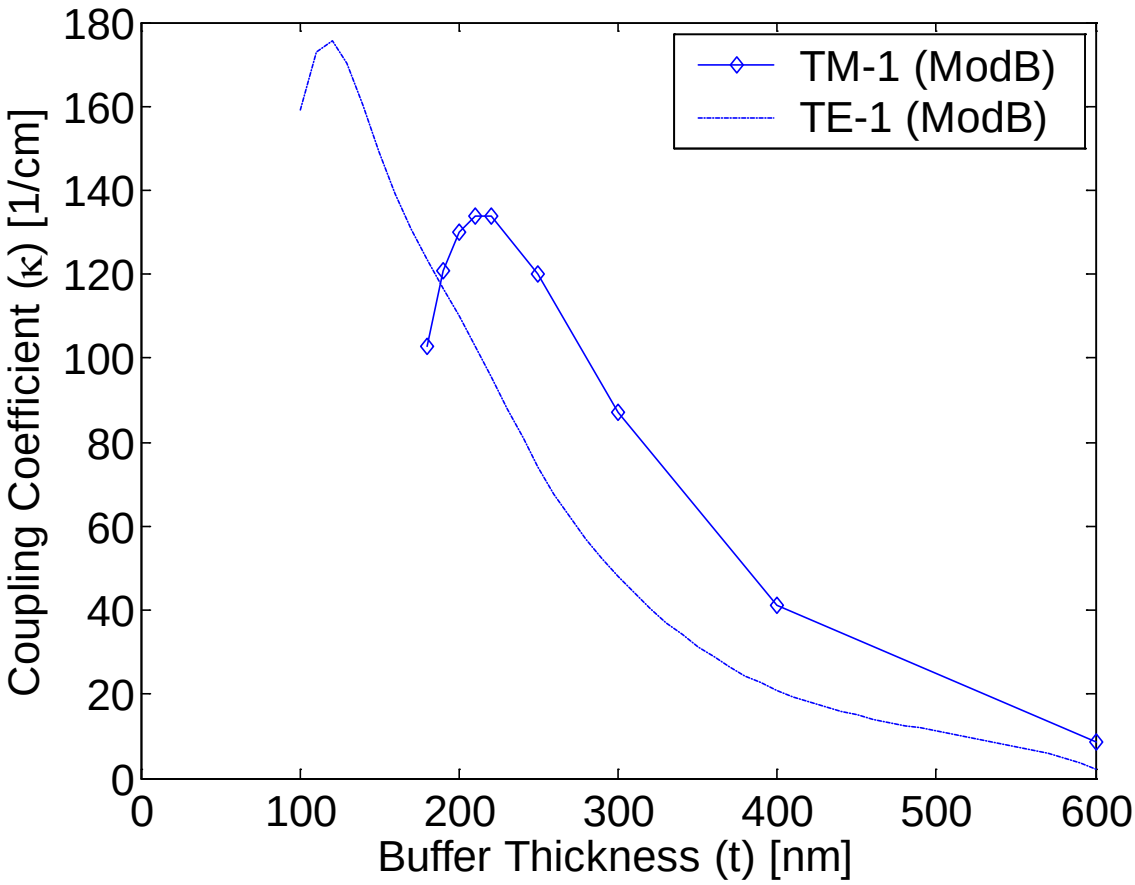

Figure 5-4. Coupling coefficient (κ) vs. buffer thickness (t)

Figure 5-5 shows the coupling coefficient versus the active layer thickness for 1st-order DFB for Model A and B, operating on TM_0 modes. The waveguides use the following parameters: the normalized corrugation amplitude ka=0.2, $\lambda = 850nm$, active layer thickness $d = 100nm$, buffer layer thickness $t = 300nm$. The refractive indices are $n_a = 3.6$ and $n_b = n_d = 3.4$.

The curves in Figure 5-5 for active layer thickness variation has similar trend with the curve in Figure 5-3 for buffer layer variation. Coupling coefficient calculated by ModA and ModB have close change rate with respect to the active layer thickness. However, the maximum coupling coefficient calculated by ModB are larger than that by ModA.

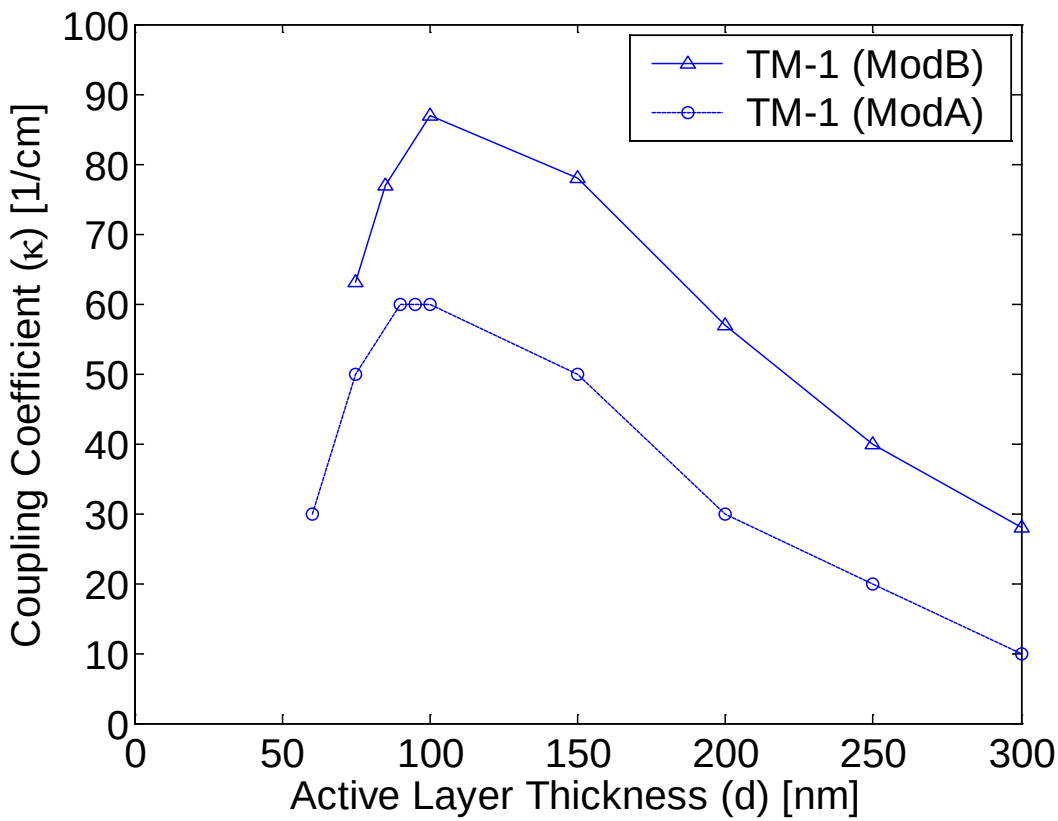

Figure 5-5. Coupling coefficient (κ) vs. active layer thickness (t)

Figure 5-6 shows the coupling coefficient versus the active layer thickness for 1st-order DFB for Model B, operating on TM_0 and TE_0 modes. The waveguides use the following parameters: the normalized corrugation amplitude ka=0.2, $\lambda = 850nm$, active layer thickness $d = 100nm$, buffer layer thickness $t = 300nm$. The refractive indices are $n_a = 3.6$ and $n_b = n_d = 3.4$.

The curves in Figure 5-6 for active layer thickness variation has similar trend with the curve in Figure 5-4 for buffer layer variation. However, the maximum coupling coefficient calculated by TM-1 ModB is larger than TE-1 ModA.

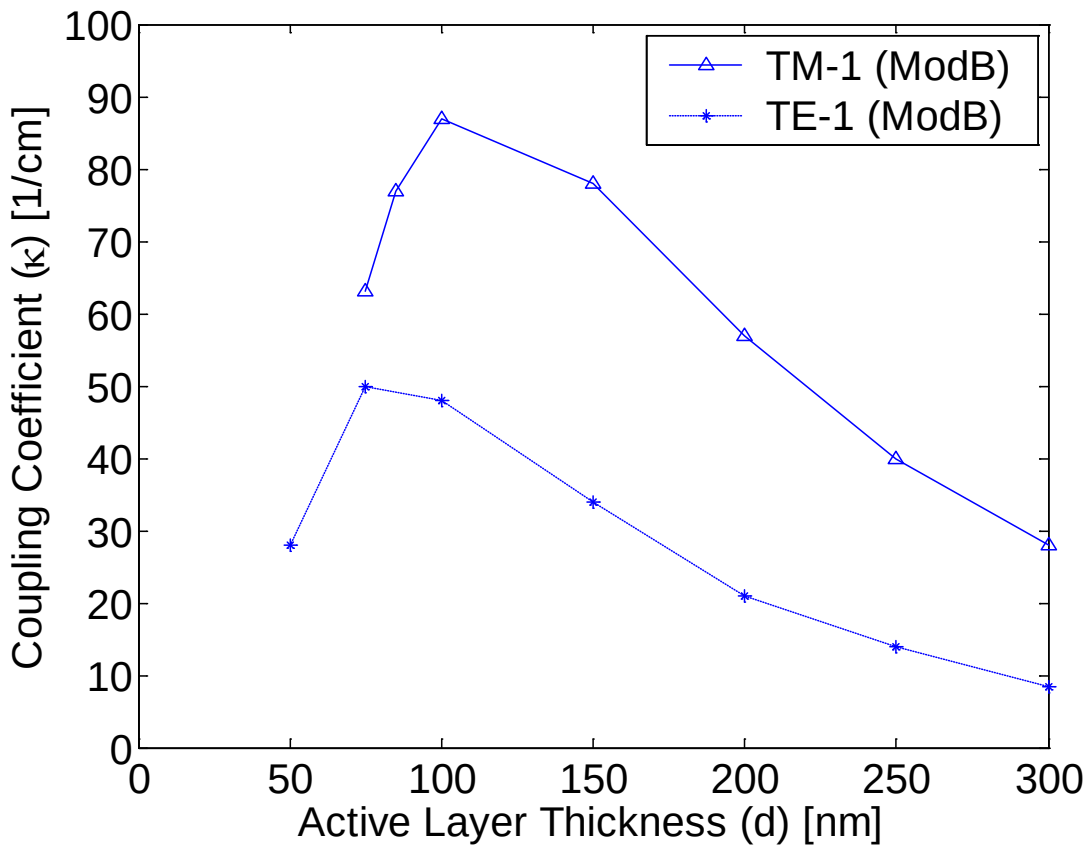

Figure 5-6. Coupling coefficient (κ) vs. active layer thickness (t)

From Figure 5-2 to Figure 5-6, κ versus geometric parameters (a, t, d) in ModB are discussed. Next, κ versus a physical parameter will be discussed. Figure 5-7 shows the plot of coupling coefficient versus corrugation amplitude for different metal material at the corrugated interface by using TM-1 (ModB). The perfect metals theoretically have a complex refractive index $-\infty i$. However, in the real world there is no such material. However, gold has the refractive index $0.16-5.3i$ is considered to be close to a perfect metal. We try another imaginary metal, refractive index $-12.8i$, closer

to a perfect metal than gold. Another imaginary metal, refractive index $2-0.1i$, is less a perfect metal than gold is and should be considered more like a dielectric material instead of a metal. In TM cases, the magnetic fields have big amplitude outside the perfect metal; while TE case, the electric fields are almost zero just outside the perfect metal. In TM case, this big amplitude will cause big interaction at the interface and cause larger coupling coefficient if the metal at the grating is more like a perfect metal. The waveguide with metal of refractive index $-12.8i$ has a larger coupling coefficient than the waveguide with gold. When the corrugation amplitude becomes larger, this metal effect and interaction will become even larger and the coupling coefficient curve becomes super-linear. Vice versa, the waveguide with metal layer replaced by a material of refractive index $2-0.1i$ has a smaller coupling coefficient than the waveguide with gold. Its coupling coefficient curve is smaller than the curve from TM-1 (ModA) which considers such metal effect to be very small.

Figure 5-8 shows the plot of coupling coefficient versus corrugation amplitude for different metal material at the corrugated interface by using TE-1. The perfect metals theoretically have the complex refractive index $-\infty i$ .Gold, with a refractive index $0.16-5.3i$, is considered to be close to a perfect metal. The metal with refractive index $-12.8i$, is closer to a perfect metal than gold is. The waveguide with metal of refractive index $-12.8i$ has a larger coupling coefficient than the waveguide with gold. In TE case, the perfect metal has zero electric field inside the perfect metal. Other imperfect metals can allow electric field penetrate into the metal surface and this penetrate depth is call skin depth [38]. The less perfect metals will have worse diffraction efficiency [Luo 90] and the coupling coefficient will be smaller.

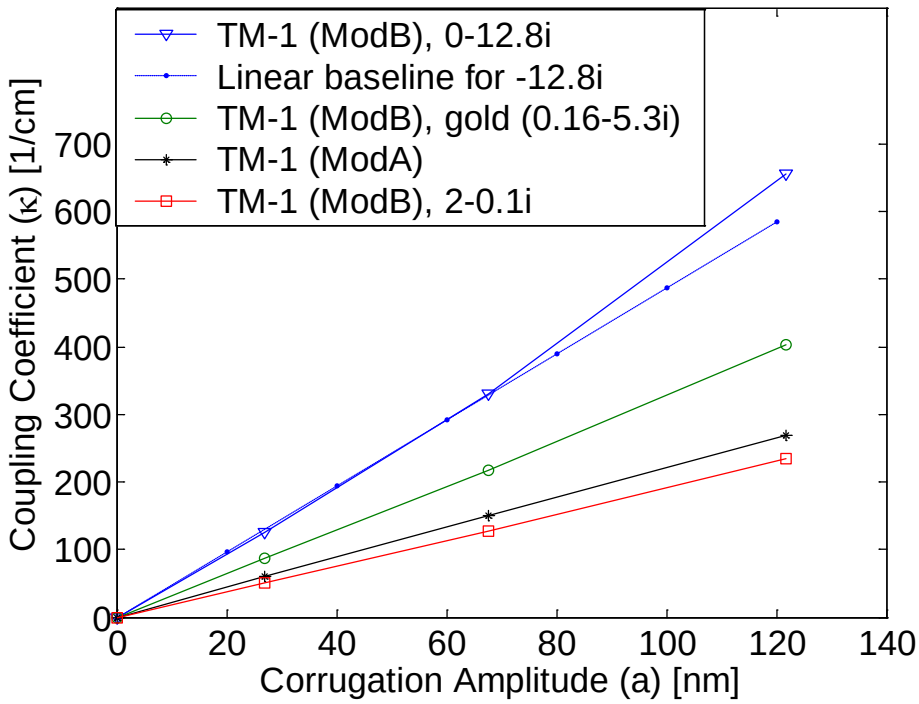

Figure 5-7. Coupling coefficient (κ) vs. corrugation amplitude (a) for different metals

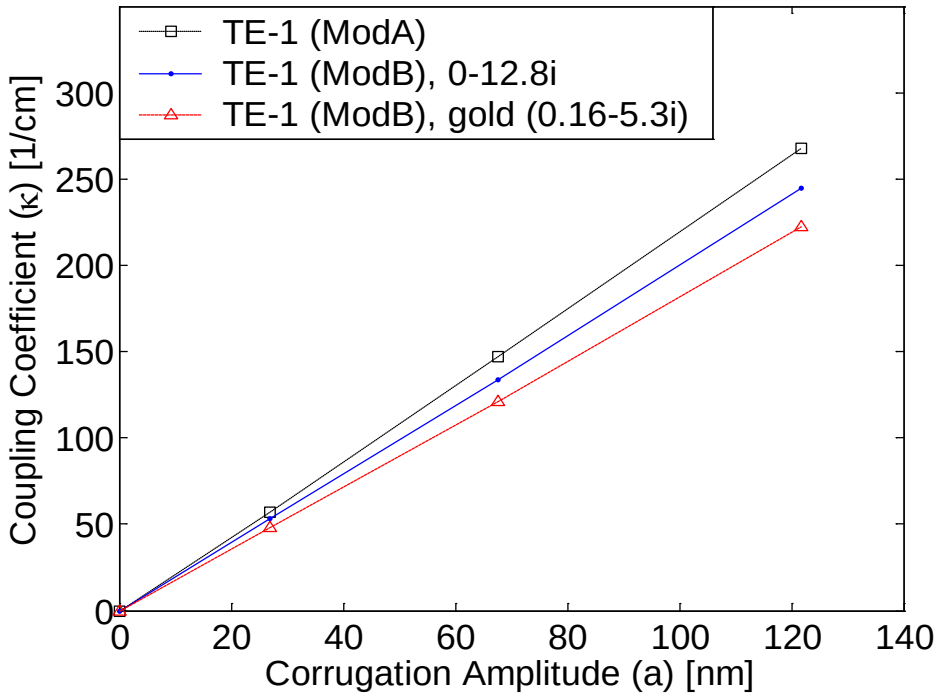

Figure 5-8. Coupling coefficient (κ) vs. corrugation amplitude (a) for different metals

CHAPTER 6
SUBSTRATE-EMITTING DFB-QCL

6.1 Multi-Layer Structure of DFB-QCL

Figure 6-1(a) is reproduced from Figure 1-5 and Figure 6-1(b) shows a scanning electron micrograph (SEM) picture of the corrugated QCL material prior to device fabrication [5].

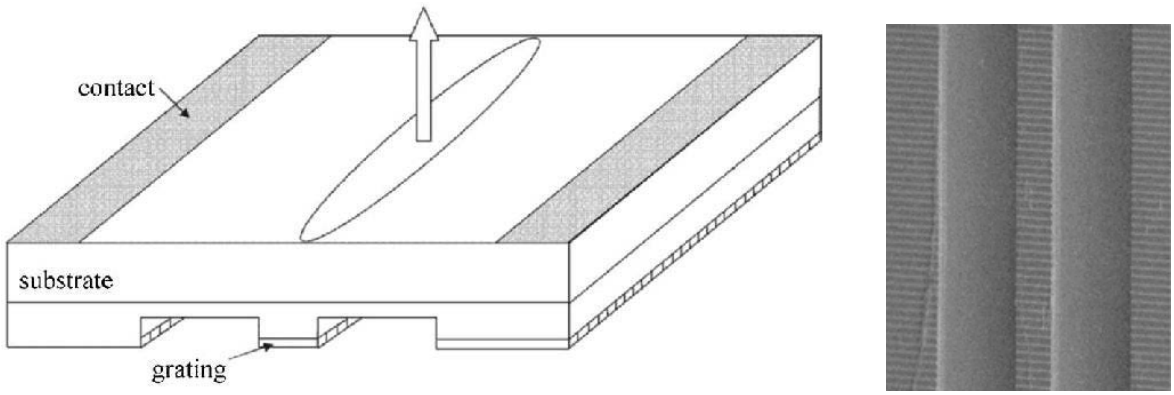

A B

Figure 6-1. Substrate-emitting DFB-QCL [5]. A) Sketch showing laser beam emission from substrate B) SEM picture showing corrugation prior to device fabrication

The corrugation or grating shown in Figure 6-1 is fabricated on top of an epitaxial layer structure grown on an InP substrate by a crystal growth technique usually referred to as MOCVD. In Figure 6-2, the relatively thick layers of this epitaxial structure are shown with the InP substrate (not shown) at the top of the figure. The active region in the middle of the structure is composed of 30 stages and each of those stages is a multilayer structure containing typically about 20 very thin layers. One of these very thin layers in each stage is a quantum well for electrons and it's in these layers where optical gain is created by stimulated emission between energy states in the conduction band.

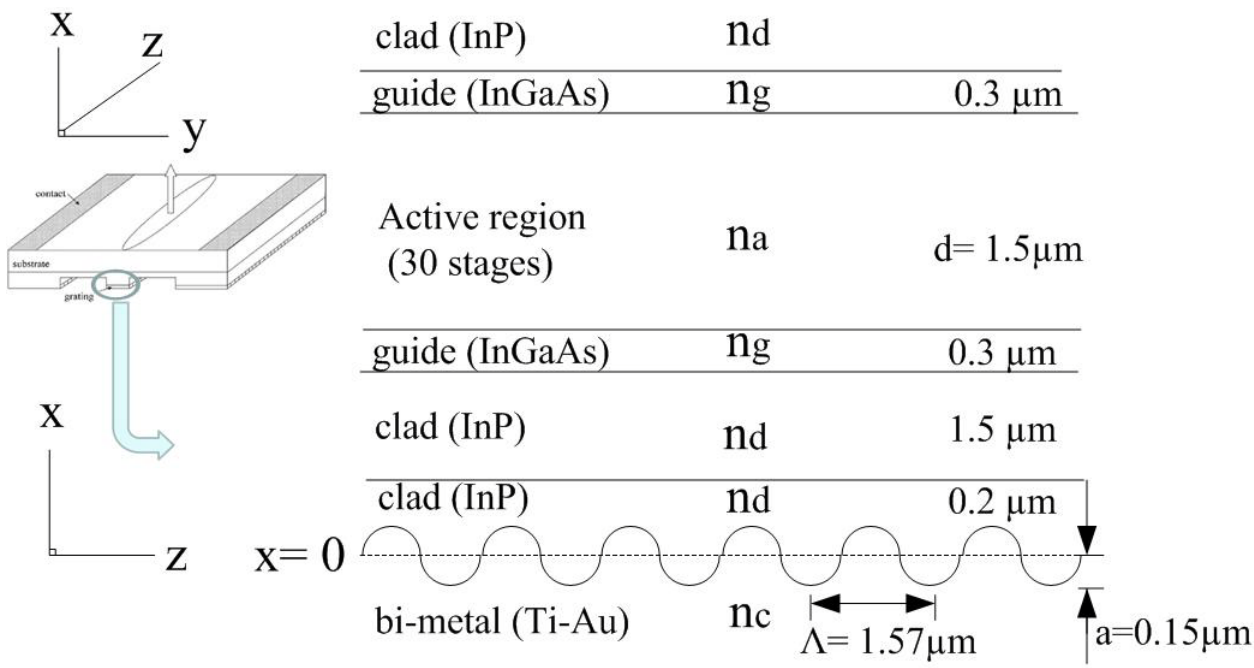

Figure 6-2. Schematic waveguide structure (zoom-in cross-sectional view at the eight-layer waveguide along the longitudinal z-direction) from the substrate-emitting DFB-QCL in Figure 6-1

As mentioned in Chapter 1, the main reasons why the DFB-QCLs made from this material did not operate at room temperature are likely to be insufficient gain from the 30 QWs in the active region and/or a too small value of κTM-2. Because of the past experience in this lab in calculating κTE-1 values in metal-clad, corrugated, we decided to study the possible κTM-2 problem. In this case, the detailed structure of the active region can be ignored and the only layer parameters required are active layer thickness (d) and its refractive index n_a .

As shown in Figure 6-2, there are 8 layers that we need to consider when computing the DFB coupling coefficients. In reality, the bottom layer called the Ti-Au, bi-metal layer is actually composed of two layers; a thin titanium layer with complex refractive index $n_{Ti} = 6.3 - 6.60633i$ for optical wavelength $\lambda = 5.1\mu m$ and thickness

$t_{Ti} = 10nm$ and a much thicker gold layer with $n_{Au} = 3.7 - 36.0849i$ and thickness 100nm. The thin Ti-layer is normally used in fabricating semiconductor lasers because it adheres better than gold to semiconductor materials like InP and GaAs.

As shown in the previous chapters, when the Floquet-Bloch Formalism is used to solve waveguide problems, the introduction of each new layer into the structure creates two more infinite summations and correspondingly bigger matrices and determinants. In this case, the problem can be solved by replacing the 8-layer with a 4-layer structure that has the same complex effective refractive index as the 8 layer structure and the same laser mode intensity profile. In this case, the waveguide parameters for the replacement guide are: $\lambda = 5.1\mu m,\ n_a = 3.38,\ n_b = n_d = 3.10,\ n_c = 4.0 - 27.5975i,$ $d = 1.5\mu m,\quad t = 1.7\mu m,$ and the complex effective refractive index for both guides is $n_e = 3.2 - 0.0003i$. The replacement 4-layer guide is shown in Figure 6-3.

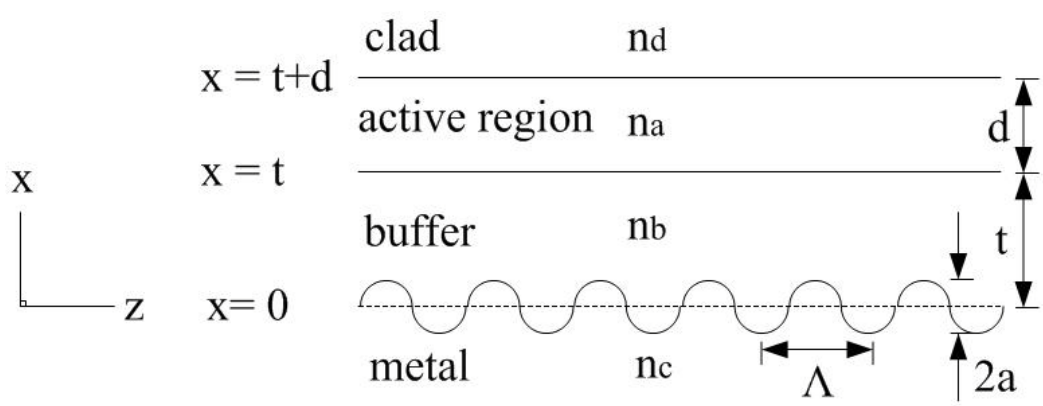

Figure 6-3. Schematic approximated four-layer waveguide structure for the eight-layer waveguide

6.2 DFB Coupling Coefficients

The parameters associated with the corrugation used in [Lya07] and sketched in Figure 6-3 are: $\Lambda = \lambda / n_e = 5.1\mu m / 3.247 = 1.57\mu m,$ corrugation amplitude $a = 0.3\mu m$

and its normalized corrugation amplitude is $ka = (2\pi/5.1)\cdot 0.3 = 0.37$. The first-order coupling coefficient is about $12\,[cm^{-1}]$ and second-order coupling coefficient is about $3\,[cm^{-1}]$. From the design criteria $\kappa L \approx 1$ based on coupled-mode theory [40], the longitudinal device length is about 3.3 mm. The device length is 2.5mm [5]. Figure 6-4 shows the coupling coefficient versus corrugation amplitude (a) by using TM Model B. The first-order coupling coefficient is about $16\,[cm^{-1}]$ for normalized corrugation amplitude ka=0.5.

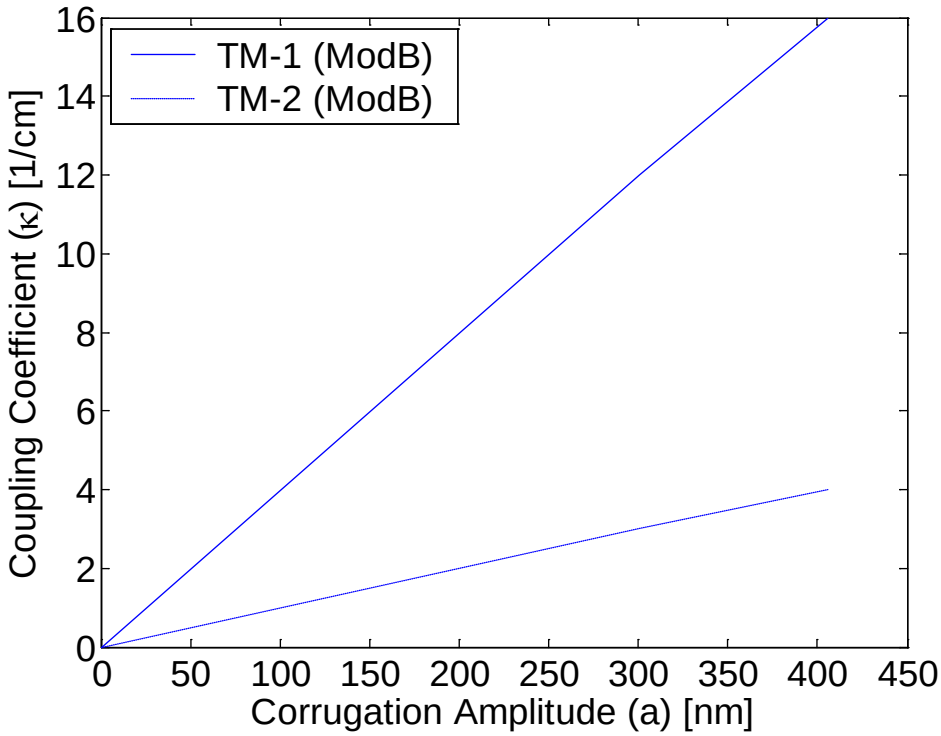

Figure 6-4. Coupling coefficient (κ) vs. corrugation amplitude (a) for simplified 4-layer waveguide

CHAPTER 7
CONCLUSION

In this dissertation, we start from the introduction of semiconductor history in Chapter 1. Chapter 2 with Appendix A introduces the fundamental concepts of optical waveguides needed to establish our models. Chapter 3 demonstrates the modeling process and Chapter 4 shows the numerical results of DFB semiconductor waveguides with corrugated metal contacts, operating on fundamental TM modes. Chapter 5 modifies the above modes and develops more universal models considering the real metals, operating on TE and TM modes. Our calculation results in Chapter 4 and 5 are compared with lab's previous work [23] and have reasonable results to validate our models. Then we apply to our model to our lab's previous DFB-QCL, operating on longer wavelength [5].

In Chapter 3, although Model A provides a quick approximation, it has limits and only provides better approximation for waveguide with smaller corrugation amplitude, thick buffer or thick active layer. These thick-layer cases have smaller coupling coefficients but have closer value to Model B in Chapter 5. Model B can deal with wider cases. If the buffer thickness is decreased, the coupling coefficient will increase. This thin buffer will also help heat dissipation from active layer to metal contact, which serves as the heat sink for hot active region in laser waveguides. Besides, Model B can consider different real metals with higher accuracy. The thinner buffer layer finally will reach a peak with maximum coupling coefficient. After that peak, the thinner buffer layer will have a deep roll-over and reach a cut-off point quickly due to the mismatch of the mode interaction with the corrugation. We should avoid this roll-over region in design. Coupling coefficient has similar response to the variation of active layer.

The coupling coefficient is more sensitive to the variation of corrugation amplitude than the variation of buffer or active layer, as shown in Table F-1 in Appendix F. Bigger corrugation amplitude will cause direct and stronger interaction at the corrugated interface. However, the layer thickness causes the mode profile change and then the tail of mode profile indirectly changes the interaction at the corrugation interface.

The TM waveguides usually have bigger coupling coefficient due to the stronger field interaction at the corrugation interface than TE waveguides. Appendix G shows the difference of field interaction at the dielectric-metal interface for planar waveguides between TM and TE modes. Although this TM field interaction increase seems to be small compared with the peak of the entire field profile, this interaction increase causes the significant change of coupling coefficient since the coupling coefficient is related to the imaginary part of complex propagation constants. Usually the imaginary part of the propagation constant is much smaller than the real part of the propagation constant. Thus, the small amount of interaction change in the interface will cause the small amount but comparatively large percentage of change in coupling coefficient.

However, the TM has thicker cut-off buffer layer so the heat dissipation to metal may become a problem. Lasers using multi-layer in the active region will have bigger thickness in such active region. The TM curves of describing the relationship between coupling coefficient and active layer thickness usually is the right-shit with respect to the TE curves. Such TM curves usually have larger thickness when the maximum coupling happens and when the cut-off happens.

The second-order DFB may have smaller coupling coefficient than the first-order DFB does. The second-order DFB has looser grating period, so the interaction at this

corrugation would be not as intense as the first-order DFB. The second-order DFB also has first-order diffracted waves which carry some mode and emit away from the corrugation interface, so the coupling coefficient would be decreased.

In Chapter 6, we discuss the design consideration based on fabrication and material and then apply our models to calculate the DFB-QCL. The coupling coefficient of this DFB-QCL is comparatively smaller than the modeling case in Chapter 5. This DFB-QCL have longer wavelength 5.1 μm than the 0.85 μm cases in Chapter 5. Considering the grating period, about 1/6 of the wavelength for the first-order DFB and 1/3 of the wavelength for the second DFB, the grating period of Mid-IR DFB-QCL is much larger than that of near-IR lasers so the interaction at the corrugated grating would be weaker and the coupling coefficient would be smaller. One way to increase the coupling coefficient is to increase the corrugation amplitude to compensate the density of grating. The other factor of decreasing the coupling coefficient is that this DFB-QCL active layer thickness is very large but the active layer thickness is needed for the multiple quantum wells. Due to the complexity of material control and optical loss of material, this calculated coupling coefficient may be theoretically larger than the actual coupling coefficient of the real devices.

APPENDIX A
MAXWELL'S EQUATIONS AND GUIDED ELECTROMAGNETIC WAVES

In this appendix it is shown that, in general, an electromagnetic wave whose beam shape is independent of propagation direction (guided wave) can be specified by a linear combination of a transverse electric (TE) vector beam function and a transverse magnetic (TM) vector beam function.

Assume an electromagnetic wave is traveling in a medium characterized by permeability μ, dielectric constant ε and conductivity σ. If the net charge density in the medium ρ is zero, Maxwell's equations for the electric field $\mathbf{E}(x,y,z,t) \equiv \mathbf{E}$ and magnetic field $\mathbf{H}(x,y,z,t) \equiv \mathbf{H}$ are [41]:

$$\nabla \cdot \mathbf{E} = 0 \tag{A-1}$$

$$\nabla \cdot \mathbf{H} = 0 \tag{A-2}$$

$$\nabla \times \mathbf{E} = -\mu \frac{\partial \mathbf{H}}{\partial t} \tag{A-3}$$

$$\nabla \times \mathbf{H} = \varepsilon \frac{\partial \mathbf{E}}{\partial t} + \sigma \mathbf{E} \tag{A-4}$$

If the wave travels in the +z-direction and has a finite extent in the x-y plane that is independent of z (a guided wave traveling in the +z-direction) then $\mathbf{E}$ and $\mathbf{H}$ can be expressed in the following general form [41]:

$$\mathbf{E} = \mathbf{E}(x,y) \cdot \exp\left[i(\beta z - \omega t)\right] \tag{A-5}$$

$$\mathbf{H} = \mathbf{H}(x,y) \cdot \exp\left[i(\beta z - \omega t)\right] \tag{A-6}$$

where β is the propagation constant (longitudinal wave constant), ω is the circular frequency and the vector beam functions $\mathbf{E}(x,y)$ and $\mathbf{H}(x,y)$ are given by:

$$\mathbf{E}(x,y) = E_x(x,y)\hat{i} + E_y(x,y)\hat{j} + E_z(x,y)\hat{k} \equiv E_x\hat{i} + E_y\hat{j} + E_z\hat{k} \tag{A-7}$$

$$\mathbf{H}(x,y) = H_x(x,y)\hat{i} + H_y(x,y)\hat{j} + H_z(x,y)\hat{k} \equiv H_x\hat{i} + H_y\hat{j} + H_z\hat{k} \tag{A-8}$$

In equations A-7 and A-8, the symbols $\hat{i}, \hat{j}$ and $\hat{k}$ represent unit vectors in the x,y and z directions respectively. It should be noted while the vector beam functions $\mathbf{E}(x,y)$ and $\mathbf{H}(x,y)$ defined in equations A-7 and A-8 are independent of z as required by the guided wave assumption, they do in general have a **k**-vector or longitudinal component. In other words, we are not assuming here that the guided waves are transverse. Note also that bold, capitalized symbols in this appendix represent vector functions while their non-vector aspects are represented by non-bold, capitalized-italicized symbols.

Substituting the electric field wave expressions in equations A-5 and A-7 into Maxwell's electric field divergence equation A-1 leads to:

$$\frac{\partial E_x}{\partial x} + \frac{\partial E_y}{\partial y} + i\beta E_z = 0 \tag{A-9}$$

Substituting the magnetic field wave expressions in equations A-6 and A-8 into Maxwell's magnetic field divergence equation A-2 leads to:

$$\frac{\partial H_x}{\partial x} + \frac{\partial H_y}{\partial y} + i\beta H_z = 0 \tag{A-10}$$

Substituting the electric and magnetic field wave expressions in equations A-5 through A-8 into Maxwell's electric field curl equation A-3 leads to three equations:

$$\frac{\partial E_z}{\partial y} - i\beta E_y = i\omega\mu H_x \tag{A-11}$$

$$i\beta E_x - \frac{\partial E_z}{\partial x} = i\omega\mu H_y \tag{A-12}$$

$$\frac{\partial E_y}{\partial x} - \frac{\partial E_x}{\partial y} = i\omega\mu H_z \tag{A-13}$$

Substituting the electric and magnetic field wave expressions in equations A-5 through A-8 into Maxwell's magnetic field curl equation A-4 leads to three equations:

$$\frac{\partial H_z}{\partial y} - i\beta H_y = \left(\sigma - i\omega\varepsilon\right) E_x \tag{A-14}$$

$$i\beta H_x - \frac{\partial H_z}{\partial x} = \left(\sigma - i\omega\varepsilon\right) E_y \tag{A-15}$$

$$\frac{\partial H_y}{\partial x} - \frac{\partial H_x}{\partial y} = \left(\sigma - i\omega\varepsilon\right) E_z \tag{A-16}$$

The transverse field functions $E_x\left(x,y\right)$, $E_y\left(x,y\right)$, $H_x\left(x,y\right)$ and $H_y\left(x,y\right)$ can be expressed in terms of derivatives of the longitudinal field functions $E_z\left(x,y\right)$ and $H_z\left(x,y\right)$ by manipulating equations A-9 through A-16 as shown below.

The expression for $E_x\left(x,y\right)$ is obtained by eliminating H_y from equations A-12 and A-14 and introducing a parameter k_t called the transverse wave constant.

$$k_t^2 = \omega^2\varepsilon\mu - \beta^2 + i\omega\mu\sigma \tag{A-17}$$

$$E_x = \frac{i}{k_t^2}\left(\beta\frac{\partial E_z}{\partial x} + \omega\mu\frac{\partial H_z}{\partial y}\right) \tag{A-18}$$

The expression for $E_y\left(x,y\right)$ is obtained by eliminating H_x from equations A-11 and A-15.

$$E_y = \frac{i}{k_t^2}\left(\beta\frac{\partial E_z}{\partial y} - \omega\mu\frac{\partial H_z}{\partial x}\right) \tag{A-19}$$

The expression for $H_x(x,y)$ is obtained by eliminating E_y from equations A-11 and A-15.

$$H_x = \frac{i}{k_t^2}\left(-\omega\varepsilon\frac{\partial E_z}{\partial y} + \beta\frac{\partial H_z}{\partial x}\right) \tag{A-20}$$

The expression for $H_y(x,y)$ is obtained by eliminating E_x from equations A-12 and A-14.

$$H_y = \frac{i}{k_t^2}\left(\omega\varepsilon\frac{\partial E_z}{\partial x} + \beta\frac{\partial H_z}{\partial y}\right) \tag{A-21}$$

Using equations A-18 and A-19, one can write down a general expression for the transverse electric vector field of a guided electromagnetic wave,

$$\begin{aligned}\mathbf{E}_t(x,y) &= E_x(x,y)\hat{i} + E_y(x,y)\hat{j} \\ &= \frac{i}{k_t^2}\left(\beta\frac{\partial E_z}{\partial x} + \omega\mu\frac{\partial H_z}{\partial y}\right)\hat{i} + \frac{i}{k_t^2}\left(\beta\frac{\partial E_z}{\partial y} - \omega\mu\frac{\partial H_z}{\partial x}\right)\hat{j}\end{aligned} \tag{A-22}$$

Using equations A-20 and A-21, one can write down a similar expression for the transverse vector magnetic field of a guided electromagnetic wave,

$$\begin{aligned}\mathbf{H}_t(x,y) &= H_x(x,y)\hat{i} + H_y(x,y)\hat{j} \\ &= \frac{i}{k_t^2}\left(-\omega\varepsilon\frac{\partial E_z}{\partial y} + \beta\frac{\partial H_z}{\partial x}\right)\hat{i} + \frac{i}{k_t^2}\left(\omega\varepsilon\frac{\partial E_z}{\partial x} + \beta\frac{\partial H_z}{\partial y}\right)\hat{j}\end{aligned} \tag{A-23}$$

The linear combination of equations A-22 and A-23 is the total transverse vector field distribution (vector beam function) for a guided electromagnetic wave

$$\mathbf{F}_t(x,y) = \mathbf{E}_t(x,y) + \mathbf{H}_t(x,y) \tag{A-24}$$

The eight terms in $\mathrm{F}_t(x,y)$ from equations A-22 and A-23 can be arranged into two groups, one group of four containing no longitudinal electric field terms, called transverse electric (TE) and the other group containing no longitudinal magnetic field

terms, called transverse magnetic (TM). This grouping in $\mathrm{F}_t(x,y)$ can be expressed by E_z and H_z in the following form:

$$\mathbf{F}_t(x,y) \equiv \mathbf{F}_t(E_z, H_z) = \mathbf{F}_{t,TE}(E_z = 0) + \mathbf{F}_{t,TM}(H_z = 0) \tag{A-25}$$

where $\mathbf{F}_{t,TE}(E_z = 0)$ is given by

$$\mathbf{F}_{t,TE}(E_z = 0) = \frac{i}{k_t^2}\left(\omega\mu\frac{\partial H_z}{\partial y} + \beta\frac{\partial H_z}{\partial x}\right)\hat{i} + \frac{i}{k_t^2}\left(-\omega\mu\frac{\partial H_z}{\partial x} + \beta\frac{\partial H_z}{\partial y}\right)\hat{j} \tag{A-26}$$

and $\mathbf{F}_{t,TM}(H_z = 0)$ is given by

$$\mathbf{F}_{t,TM}(H_z = 0) = \frac{i}{k_t^2}\left(\beta\frac{\partial E_z}{\partial x} - \omega\varepsilon\frac{\partial E_z}{\partial y}\right)\hat{i} + \frac{i}{k_t^2}\left(\beta\frac{\partial E_z}{\partial y} + \omega\varepsilon\frac{\partial E_z}{\partial x}\right)\hat{j} \tag{A-27}$$

Experimentally, it is found that the beams emitted from QCLs are polarized perpendicular to the plane of the waveguide layers (x-direction in our notation). This is due to the fact that the intersubband transitions responsible for providing optical gain in a thin quantum well active layer can only be excited by an electric field normal to the layer [Fai 94]. The condition that $E_x \neq 0$ for QCLs implies that $E_y = 0$. When used in equation A-22, one obtains the following:

$$\frac{\partial H_z}{\partial x} = \frac{\beta}{\omega\mu}\frac{\partial E_z}{\partial y} \tag{A-28a}$$

$$\frac{\partial E_z}{\partial y} = \frac{\omega\mu}{\beta}\frac{\partial H_z}{\partial x} \tag{A-28b}$$

Substituting equation A-28a into equation A-26:

$$\begin{aligned}\mathbf{F}_{t,TE}(E_z = 0) &= \frac{i}{k_t^2}\left(\omega\mu\frac{\partial H_z}{\partial y} + \frac{\beta^2}{\omega\mu}\frac{\partial E_z}{\partial y}\right)\hat{i} + \frac{i}{k_t^2}\left(-\beta\frac{\partial E_z}{\partial y} + \beta\frac{\partial H_z}{\partial y}\right)\hat{j} \\ &= \frac{i}{k_t^2}\left(\omega\mu\frac{\partial H_z}{\partial y}\hat{i} + \beta\frac{\partial H_z}{\partial y}\hat{j}\right)\end{aligned} \tag{A-29}$$

Substituting equation A-28b into equation A-27:

$$\begin{aligned}\mathbf{F}_{t,TM}(H_z=0) &= \frac{i}{k_t^2}\left(\beta\frac{\partial E_z}{\partial x}-\frac{\omega^2\varepsilon\mu}{\beta}\frac{\partial H_z}{\partial x}\right)\hat{i}+\frac{i}{k_t^2}\left(\omega\mu\frac{\partial H_z}{\partial x}+\omega\varepsilon\frac{\partial E_z}{\partial x}\right)\hat{j} \\ &= \frac{i}{k_t^2}\cdot\left(\beta\frac{\partial E_z}{\partial x}\hat{i}+\omega\varepsilon\frac{\partial E_z}{\partial x}\hat{j}\right)\end{aligned} \tag{A-30}$$

If we use the assumption $\partial/\partial y = 0$ for the slab waveguide described in Chapter II and substituting $\partial/\partial y = 0$ into equation A-29, the transverse field operating on TE modes, $\mathbf{F}_{t,TE}$,will vanish. The transverse filed operating on TM modes, $\mathbf{F}_{t,TM}$, in equation A-30 depends on E_z and x.

From equations A-24 and A-25, $\mathbf{F}_{t,TM}$ can be further expressed by transverse electric field and transverse magnetic field, both operating on TM modes:

$$\mathbf{F}_{t,TM}(x,y) = \mathbf{E}_{t,TM}(x,y) + \mathbf{H}_{t,TM}(x,y) \tag{A-31}$$

Substituting $H_z = 0$ and $\partial/\partial y = 0$ into equation A-22, $\mathbf{E}_{t,TM}(x,y)$ is given by:

$$\mathbf{E}_{t,TM}(x,y) = \frac{i\beta}{k_t^2}\frac{\partial E_z}{\partial x}\hat{i} \equiv \mathbf{E}_{x,TM} \tag{A-32}$$

Substituting $H_z = 0$ and $\partial/\partial y = 0$ into equation A-23, $\mathbf{H}_{t,TM}(x,y)$ is given by:

$$\mathbf{H}_{t,TM}(x,y) = \frac{i\omega\varepsilon}{k_t^2}\frac{\partial E_z}{\partial x}\hat{j} \equiv \mathbf{H}_{y,TM} \tag{A-33}$$

Similarly to equation A-31, the total longitudinal vector field distribution (vector beam function) $\mathbf{F}_{l,TM}(x,y)$ for a guided electromagnetic wave operating on TM modes is the linear combination of longitudinal electric filed and longitudinal magnetic field, both are operating on TM modes:

$$\mathbf{F}_{l,TM}\left(x,y\right)=\mathbf{E}_{l,TM}\left(x,y\right)+\mathbf{H}_{l,TM}\left(x,y\right) \tag{A-34}$$

Substituting $H_z=0$ and $\partial/\partial y=0$ into equation A-16, $\mathbf{E}_{l,TM}\left(x,y\right)$ is given by:

$$\mathbf{E}_{l,TM}\left(x,y\right)=E_z\hat{k}=\frac{1}{\left(\sigma-i\omega\varepsilon\right)}\frac{\partial H_y}{\partial x}\hat{k}\equiv\mathbf{E}_{z,TM} \tag{A-35}$$

Substituting $H_z=0$ and $\partial/\partial y=0$ into equation A-13, $\mathbf{H}_{l,TM}\left(x,y\right)=0$. Therefore, the total longitudinal field operating on TM modes, $\mathbf{F}_{l,TM}\left(x,y\right)$, only has a non-zero term $\mathbf{E}_{l,TM}\left(x,y\right)$, as shown in equation A-35.

Figure A-1 summaries the three polarizations in the slab waveguide operating on TM modes. From the derivation in Chapter II, we would use one of these three polarizations: the only one magnetic field $\mathbf{H}_y$ obtained from equation A-33, to describe the other two polarizations. These two polarizations are electric fields: $\mathbf{E}_{x,TM}\left(x,y\right)$ derived from equation A-32 and $\mathbf{E}_{z,TM}\left(x,y\right)$ derived from equation A-35. In this figure, we remove subscripts TM and use $\mathbf{H}_y$, $\mathbf{E}_x$ and $\mathbf{E}_z$ to represent the above three polarizations. In brief, for slab waveguides operating on transverse magnetic modes, only the non-zero magnetic fields $\mathbf{H}_y$ (no electric field) exist in the transverse y-direction.

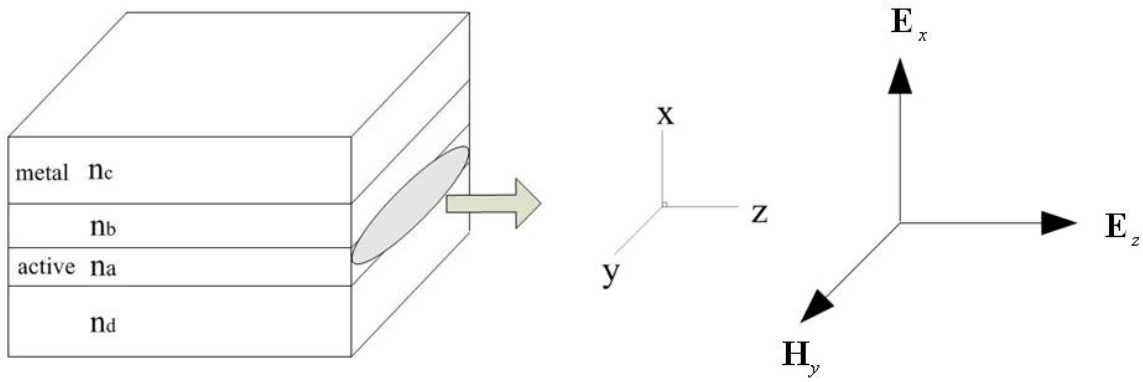

Figure A-1. Three polarizations in the slab waveguide operating on TM modes

APPENDIX B
DERIVATION OF EQUATION 3-32 FOR PLANAR WAVEGUIDEDS IN TM MODE

Re-list equations (3-23) through (3-27) as follow:

$$B_0 - D_0 \cdot \exp\left(p_0 t\right) - E_0 \cdot \exp\left(-p_0 t\right) = 0 \tag{3-23}$$

$$\left(\frac{\sigma_0}{\varepsilon_a}\right) C_0 - \left(\frac{p_0}{\varepsilon_b}\right) D_0 \cdot \exp\left(p_0 t\right) + \left(\frac{p_0}{\varepsilon_b}\right) E_0 \cdot \exp\left(-p_0 t\right) = 0 \tag{3-24}$$

$$A_0 - B_0 \cdot \cos\left(\sigma_0 d\right) - C_0 \cdot \sin\left(\sigma_0 d\right) = 0 \tag{3-25}$$

$$\left(\frac{q_0}{\varepsilon_d}\right) A_0 - \left(\frac{\sigma_0}{\varepsilon_a}\right) B_0 \cdot \sin\left(\sigma_0 d\right) + \left(\frac{\sigma_0}{\varepsilon_a}\right) C_0 \cdot \cos\left(\sigma_0 d\right) = 0 \tag{3-26}$$

$$D_0 I_0\left(0\right) + E_0 I_0\left(0\right) = 0 \tag{3-27}$$

$$\text{where } I_n\left(0\right) = \begin{cases} 1, & n = 0 \\ 0, & n \neq 0 \end{cases} \tag{3-28}$$

Equations 3-23 to 3-27 constitute a linear homogeneous matrix system and can be written in matrix form as follows:

$$\begin{bmatrix} 0 & 1 & 0 & -\exp\left(p_0 \cdot t\right) & -\exp\left(-p_0 \cdot t\right) \\ 0 & 0 & \frac{\sigma_0}{\varepsilon_a} & -\frac{p_0}{\varepsilon_b}\exp\left(p_0 \cdot t\right) & \frac{p_0}{\varepsilon_b}\exp\left(-p_0 \cdot t\right) \\ 1 & -\cos\left(\sigma_0 \cdot d\right) & -\sin\left(\sigma_0 \cdot d\right) & 0 & 0 \\ \frac{q_0}{\varepsilon_d} & -\frac{\sigma_0}{\varepsilon_a}\sin\left(\sigma_0 \cdot d\right) & \frac{\sigma_0}{\varepsilon_a}\cos\left(\sigma_0 \cdot d\right) & 0 & 0 \\ 0 & 0 & 0 & 1 & 1 \end{bmatrix} \begin{bmatrix} A_0 \\ B_0 \\ C_0 \\ D_0 \\ E_0 \end{bmatrix} = 0 \tag{B-1}$$

To have a nonzero solution for A_0, B_0, C_0, D_0, E_0 in equation B-1, the determinant of the coefficient matrix must be zero [24][25].

$$\begin{vmatrix} 0 & 1 & 0 & -\exp(p_0 \cdot t) & -\exp(-p_0 \cdot t) \\ 0 & 0 & \frac{\sigma_0}{\varepsilon_a} & -\frac{p_0}{\varepsilon_b}\exp(p_0 \cdot t) & \frac{p_0}{\varepsilon_b}\exp(-p_0 \cdot t) \\ 1 & -\cos(\sigma_0 \cdot d) & -\sin(\sigma_0 \cdot d) & 0 & 0 \\ \frac{q_0}{\varepsilon_d} & -\frac{\sigma_0}{\varepsilon_a}\sin(\sigma_0 \cdot d) & \frac{\sigma_0}{\varepsilon_a}\cos(\sigma_0 \cdot d) & 0 & 0 \\ 0 & 0 & 0 & 1 & 1 \end{vmatrix} = 0 \qquad \text{(B-2)}$$

To simplify equation B-2, we used the matrix expansion of this determinant [Bro 89] by minors of the fifth row. This 5 by 5 matrix is reduced into two 4 by 4 matrices as follows:

$$-1 \cdot \begin{vmatrix} 0 & 1 & 0 & -\exp(-p_0 \cdot t) \\ 0 & 0 & \frac{\sigma_0}{\varepsilon_a} & \frac{p_0}{\varepsilon_b} \cdot \exp(-p_0 \cdot t) \\ 1 & -\cos(\sigma_0 \cdot d) & -\sin(\sigma_0 \cdot d) & 0 \\ 1 & -\frac{\sigma_0 / \varepsilon_a}{q_0 / \varepsilon_d} \cdot \sin(\sigma_0 \cdot d) & \frac{\sigma_0 / \varepsilon_a}{q_0 / \varepsilon_d} \cdot \cos(\sigma_0 \cdot d) & 0 \end{vmatrix}$$

$$+1 \cdot \begin{vmatrix} 0 & 1 & 0 & -\exp(p_0 \cdot t) \\ 0 & 0 & \frac{\sigma_0}{\varepsilon_a} & -\frac{p_0}{\varepsilon_b} \cdot \exp(p_0 \cdot t) \\ 1 & -\cos(\sigma_0 \cdot d) & -\sin(\sigma_0 \cdot d) & 0 \\ 1 & -\frac{\sigma_0 / \varepsilon_a}{q_0 / \varepsilon_d} \cdot \sin(\sigma_0 \cdot d) & \frac{\sigma_0 / \varepsilon_a}{q_0 / \varepsilon_d} \cdot \cos(\sigma_0 \cdot d) & 0 \end{vmatrix} = 0 \qquad \text{(B-3)}$$

(i) From the first term in equation B-3, the first column is chosen for expanding this 4 by 4 matrix into two 3 by 3 matrices:

$$= -1 \cdot \begin{vmatrix} 1 & 0 & -\exp(-p_0 \cdot t) \\ 0 & \frac{\sigma_0}{\varepsilon_a} & \frac{p_0}{\varepsilon_b} \cdot \exp(-p_0 \cdot t) \\ -\frac{\sigma_0 / \varepsilon_a}{q_0 / \varepsilon_d} \cdot \sin(\sigma_0 \cdot d) & \frac{\sigma_0 / \varepsilon_a}{q_0 / \varepsilon_d} \cdot \cos(\sigma_0 \cdot d) & 0 \end{vmatrix}$$

$$+1\cdot\begin{vmatrix} 1 & 0 & -\exp(-p_0\cdot t) \\ 0 & \dfrac{\sigma_0}{\varepsilon_a} & \dfrac{p_0}{\varepsilon_b}\cdot\exp(-p_0\cdot t) \\ -\cos(\sigma_0\cdot d) & -\sin(\sigma_0\cdot d) & 0 \end{vmatrix} \tag{B-4}$$

From the first term in equation B-4, the first row is chosen for expanding this 3 by 3 matrix into two 2 by 2 matrices:

$$=-1\cdot\begin{vmatrix} \dfrac{\sigma_0}{\varepsilon_a} & \dfrac{p_0}{\varepsilon_b}\cdot\exp(-p_0\cdot t) \\ \dfrac{\sigma_0/\varepsilon_a}{q_0/\varepsilon_d}\cdot\cos(\sigma_0\cdot d) & 0 \end{vmatrix}$$

$$-\left[-\exp(-p_0\cdot t)\right]\cdot\begin{vmatrix} 0 & \dfrac{\sigma_0}{\varepsilon_a} \\ -\dfrac{\sigma_0/\varepsilon_a}{q_0/\varepsilon_d}\cdot\sin(\sigma_0\cdot d) & \dfrac{\sigma_0/\varepsilon_a}{q_0/\varepsilon_d}\cdot\cos(\sigma_0\cdot d) \end{vmatrix}$$

$$=\frac{\sigma_0/\varepsilon_a}{q_0/\varepsilon_d}\cdot\frac{p_0}{\varepsilon_b}\cdot\exp(-p_0\cdot t)\cdot\cos(\sigma_0\cdot d)+\frac{(\sigma_0/\varepsilon_a)^2}{q_0}\cdot\exp(-p_0\cdot t)\cdot\sin(\sigma_0\cdot d) \tag{B-5}$$

From the second term in equation B-4, the first row is chosen for expanding this 3 by 3 matrix into two 2 by 2 matrices:

$$=1\cdot\begin{vmatrix} \dfrac{\sigma_0}{\varepsilon_a} & \dfrac{p_0}{\varepsilon_b}\cdot\exp(-p_0\cdot t) \\ -\sin(\sigma_0\cdot d) & 0 \end{vmatrix}+\left[-\exp(-p_0\cdot t)\right]\cdot\begin{vmatrix} 0 & \dfrac{\sigma_0}{\varepsilon_a} \\ -\cos(\sigma_0\cdot d) & -\sin(\sigma_0\cdot d) \end{vmatrix}$$

$$=\frac{p_0}{\varepsilon_b}\cdot\exp(-p_0\cdot t)\cdot\sin(\sigma_0\cdot d)-\sigma_0\cdot\exp(-p_0\cdot t)\cdot\cos(\sigma_0\cdot d) \tag{B-6}$$

(ii) From the second term in equation B-3, the first column is chosen for expanding this 4 by 4 matrix into two 3 by 3 matrices:

$$= -1 \cdot \begin{vmatrix} 1 & 0 & -\exp(p_0 \cdot t) \\ 0 & \frac{\sigma_0}{\varepsilon_a} & -\frac{p_0}{\varepsilon_b} \cdot \exp(p_0 \cdot t) \\ -\frac{\sigma_0 / \varepsilon_a}{q_0 / \varepsilon_d} \cdot \sin(\sigma_0 \cdot d) & \frac{\sigma_0 / \varepsilon_a}{q_0 / \varepsilon_d} \cdot \cos(\sigma_0 \cdot d) & 0 \end{vmatrix}$$

$$-1 \cdot \begin{vmatrix} 1 & 0 & -\exp(p_0 \cdot t) \\ 0 & \frac{\sigma_0}{\varepsilon_a} & -\frac{p_0}{\varepsilon_b} \cdot \exp(p_0 \cdot t) \\ -\cos(\sigma_0 \cdot d) & -\sin(\sigma_0 \cdot d) & 0 \end{vmatrix} \tag{B-7}$$

From the first term in equation B-7, the first row is chosen for expanding this by 3 matrix into two 2 by 2 matrices:

$$= -1 \cdot \begin{vmatrix} \frac{\sigma_0}{\varepsilon_a} & -\frac{p_0}{\varepsilon_b} \cdot \exp(p_0 \cdot t) \\ \frac{\sigma_0 / \varepsilon_a}{q_0 / \varepsilon_d} \cdot \cos(\sigma_0 \cdot d) & 0 \end{vmatrix}$$

$$+\left[-\exp(p_0 \cdot t)\right] \cdot \begin{vmatrix} 0 & \frac{\sigma_0}{\varepsilon_a} \\ -\frac{\sigma_0 / \varepsilon_a}{q_0 / \varepsilon_d} \cdot \sin(\sigma_0 \cdot d) & \frac{\sigma_0 / \varepsilon_a}{q_0 / \varepsilon_d} \cdot \cos(\sigma_0 \cdot d) \end{vmatrix}$$

$$= \frac{\sigma_0 / \varepsilon_a}{q_0 / \varepsilon_d} \cdot \frac{p_0}{\varepsilon_b} \cdot \exp(p_0 \cdot t) \cdot \cos(\sigma_0 \cdot d) - \frac{(\sigma_0 / \varepsilon_a)^2}{q_0} \cdot \exp(p_0 \cdot t) \cdot \sin(\sigma_0 \cdot d) \tag{B-8}$$

From the second term in equation B-7, the first row is chosen for expanding this 3 by 3 matrix into two 2 by 2 matrices:

$$= -1 \cdot \begin{vmatrix} \frac{\sigma_0}{\varepsilon_a} & -\frac{p_0}{\varepsilon_b} \cdot \exp(p_0 \cdot t) \\ -\sin(\sigma_0 \cdot d) & 0 \end{vmatrix} - \left[-\exp(p_0 \cdot t)\right] \cdot \begin{vmatrix} 0 & \frac{\sigma_0}{\varepsilon_a} \\ -\cos(\sigma_0 \cdot d) & -\sin(\sigma_0 \cdot d) \end{vmatrix}$$

$$= \frac{p_0}{\varepsilon_b} \cdot \exp(p_0 \cdot t) \cdot \sin(\sigma_0 \cdot d) + \sigma_0 \cdot \exp(p_0 \cdot t) \cdot \cos(\sigma_0 \cdot d) \tag{B-9}$$

(iii) Combine the above expanded equations into a more condensed formula.

Add equations B-5 and B-8 to obtain

$$=\frac{\sigma_0/\varepsilon_a}{q_0/\varepsilon_d}\cdot\frac{p_0}{\varepsilon_b}\cdot\cos\left(\sigma_0\cdot d\right)\cdot\left[\exp\left(p_0\cdot t\right)+\exp\left(-p_0\cdot t\right)\right]$$

$$-\frac{\left(\sigma_0/\varepsilon_a\right)^2}{q_0}\cdot\sin\left(\sigma_0\cdot d\right)\cdot\left[\exp\left(p_0\cdot t\right)-\exp\left(-p_0\cdot t\right)\right] \qquad \text{(B-10)}$$

Add equations B-6 and B-9 to obtain

$$=\frac{p_0}{\varepsilon_b}\cdot\sin\left(\sigma_0\cdot d\right)\left[\exp\left(p_0\cdot t\right)+\exp\left(-p_0\cdot t\right)\right]$$

$$+\frac{\sigma_0}{\varepsilon_a}\cdot\cos\left(\sigma_0\cdot d\right)\cdot\left[\exp\left(p_0\cdot t\right)-\exp\left(-p_0\cdot t\right)\right] \qquad \text{(B-11)}$$

Combine equations B-10 and B-11 to obtain the full value of the original 5 by 5 determinant in equation B-2.

$$\frac{p_0}{\varepsilon_b}\cdot\left[\exp\left(p_0\cdot t\right)+\exp\left(-p_0\cdot t\right)\right]\cdot\left[\frac{\sigma_0/\varepsilon_a}{q_0/\varepsilon_d}\cdot\cos\left(\sigma_0\cdot d\right)+\sin\left(\sigma_0\cdot d\right)\right]$$

$$+\frac{\sigma_0}{\varepsilon_a}\cdot\left[\exp\left(p_0\cdot t\right)-\exp\left(-p_0\cdot t\right)\right]\cdot\left[-\frac{\sigma_0/\varepsilon_a}{q_0/\varepsilon_d}\cdot\sin\left(\sigma_0\cdot d\right)+\cos\left(\sigma_0\cdot d\right)\right]=0 \qquad \text{(B-12)}$$

Divide equation B-12 by 2 and use trigonometric formula [26] to obtain:

$$\frac{p_0}{\varepsilon_b}\cdot\cosh\left(p_0\cdot t\right)\cdot\left[\frac{\sigma_0/\varepsilon_a}{q_0/\varepsilon_d}\cdot\cos\left(\sigma_0\cdot d\right)+\sin\left(\sigma_0\cdot d\right)\right]$$
$$+\frac{\sigma_0}{\varepsilon_a}\cdot\sinh\left(p_0\cdot t\right)\cdot\left[-\frac{\sigma_0/\varepsilon_a}{q_0/\varepsilon_d}\cdot\sin\left(\sigma_0\cdot d\right)+\cos\left(\sigma_0\cdot d\right)\right]=0 \qquad \text{(B-13)}$$

Divide equation B-13 by $\cos\left(\sigma_0\cdot t\right)$

$$\frac{p_0}{\varepsilon_b}\cdot\cosh\left(p_0\cdot t\right)\cdot\left[\frac{\sigma_0/\varepsilon_a}{q_0/\varepsilon_d}+\tan\left(\sigma_0\cdot d\right)\right]$$

$$+\frac{\sigma_0}{\varepsilon_a}\cdot\sinh\left(p_0\cdot t\right)\cdot\left[-\frac{\sigma_0/\varepsilon_a}{q_0/\varepsilon_d}\cdot\tan\left(\sigma_0\cdot d\right)+1\right]=0 \tag{B-14}$$

Divide equation B-14 by $\sinh\left(p_0\cdot t\right)$

$$\frac{p_0}{\varepsilon_b}\cdot\coth\left(p_0\cdot t\right)\cdot\left[\frac{\sigma_0/\varepsilon_a}{q_0/\varepsilon_d}+\tan\left(\sigma_0\cdot d\right)\right]+\frac{\sigma_0}{\varepsilon_a}\cdot\left[-\frac{\sigma_0/\varepsilon_a}{q_0/\varepsilon_d}\cdot\tan\left(\sigma_0\cdot d\right)+1\right]=0$$

$$\Rightarrow\coth\left(p_0\cdot t\right)=-\frac{\sigma_0/\varepsilon_a}{p_0/\varepsilon_b}\cdot\frac{\left[1-\frac{\sigma_0/\varepsilon_a}{q_0/\varepsilon_d}\cdot\tan\left(\sigma_0\cdot d\right)\right]}{\left[\frac{\sigma_0/\varepsilon_a}{q_0/\varepsilon_d}+\tan\left(\sigma_0\cdot d\right)\right]}$$

$$=-\frac{\sigma_0/\varepsilon_a}{p_0/\varepsilon_b}\cdot\frac{\left[\frac{q_0/\varepsilon_d}{\sigma_0/\varepsilon_a}-\cdot\tan\left(\sigma_0\cdot d\right)\right]}{\left[1+\frac{q_0/\varepsilon_d}{\sigma_0/\varepsilon_a}\cdot\tan\left(\sigma_0\cdot d\right)\right]} \tag{B-15}$$

Use trigonometric formula [26] to simplify equation B-15:

Let $\tan\left(\theta\right)=\frac{q_0/\varepsilon_d}{\sigma_0/\varepsilon_a}\quad\Rightarrow\theta=\tan^{-1}\left(\frac{q_0/\varepsilon_d}{\sigma_0/\varepsilon_a}\right)$ (B-16)

Substitute equation B-16 into B-15

$$\coth\left(p_0\cdot t\right)=-\frac{\sigma_0/\varepsilon_a}{p_0/\varepsilon_b}\cdot\frac{\left[\tan\left(\theta\right)-\tan\left(\sigma_0\cdot d\right)\right]}{\left[1+\tan\left(\theta\right)\cdot\tan\left(\sigma_0\cdot d\right)\right]}$$

$$=\frac{\sigma_0/\varepsilon_a}{p_0/\varepsilon_b}\cdot\frac{\left[\tan\left(\sigma_0\cdot d\right)-\tan\left(\theta\right)\right]}{\left[1+\tan\left(\sigma_0\cdot d\right)\cdot\tan\left(\theta\right)\right]}$$

$$=\frac{\sigma_0/\varepsilon_a}{p_0/\varepsilon_b}\cdot\tan\left[\sigma_0\cdot d-\tan^{-1}\left(\frac{q_0/\varepsilon_d}{\sigma_0/\varepsilon_a}\right)\right] \tag{B-17}$$

It is customary to specify the refraction index of each layer (n_j) in these multi-layer structures. As a consequence, the medium permittivity ε_j in equation B-17 is replaced by $\varepsilon_0 \, n_j^{\,2}$, where ε_0 is the vacuum permittivity .

$$\coth\left(p_0 \cdot t\right) = \frac{\sigma_0 / n_a^2}{p_0 / n_b^2} \tan\left[\sigma_0 \cdot d - \tan^{-1}\left(\frac{q_0}{\sigma_0} \cdot \frac{n_a^2}{n_d^2}\right)\right] \tag{B-18}$$

Thus, equations 3-31 and 3-32 Q.E.D.

APPENDIX C
DERIVATION OF EQUATION 3-41 FOR FIRST-ORDER DFB WAVEGUIDES IN TM MODE

Rearrange equation 3-23 through 3-26 as follow:

$$A_0 = B_0 \cdot \cos(\sigma_0 d) + C_0 \cdot \sin(\sigma_0 d) \tag{C-1}$$

$$\left(\frac{q_0}{\varepsilon_d}\right) A_0 = \left(\frac{\sigma_0}{\varepsilon_a}\right) B_0 \cdot \sin(\sigma_0 d) - \left(\frac{\sigma_0}{\varepsilon_a}\right) C_0 \cdot \cos(\sigma_0 d) \tag{C-2}$$

$$B_0 = D_0 \cdot \exp(p_0 t) + E_0 \cdot \exp(-p_0 t) \tag{C-3}$$

$$\left(\frac{\sigma_0}{\varepsilon_a}\right) C_0 = \left(\frac{p_0}{\varepsilon_b}\right) D_0 \cdot \exp(p_0 t) - \left(\frac{p_0}{\varepsilon_b}\right) E_0 \cdot \exp(-p_0 t) \tag{C-4}$$

Equation C-1 divided by C-2 and use trigonometric formula [26] to obtain::

$$\frac{\sigma_0 / \varepsilon_a}{q_0 / \varepsilon_d} = \frac{B_0 \cdot \cos(\sigma_0 d) + C_0 \cdot \sin(\sigma_0 d)}{B_0 \cdot \sin(\sigma_0 d) - C_0 \cdot \cos(\sigma_0 d)} = \frac{\frac{B_0}{C_0} + \tan(\sigma_0 d)}{\frac{B_0}{C_0} \cdot \tan(\sigma_0 d) - 1} = -\tan\left[\sigma_0 d + \tan^{-1}\left(\frac{B_0}{C_0}\right)\right]$$

$$\Rightarrow \quad \frac{B_0}{C_0} = -\tan\left[\sigma_0 d + \tan^{-1}\left(\frac{\sigma_0 / \varepsilon_a}{q_0 / \varepsilon_d}\right)\right] = -\mathrm{X}_0 \tag{C-5}$$

Equation C-3 divided by C-4:

$$\frac{B_0}{C_0} = \frac{\sigma_0 / \varepsilon_a}{p_0 / \varepsilon_b} \cdot \frac{D_0 \cdot \exp(p_0 t) + E_0 \cdot \exp(-p_0 t)}{D_0 \cdot \exp(p_0 t) - E_0 \cdot \exp(-p_0 t)} = -\mathrm{X}_0$$

$$\Rightarrow \quad \frac{D_0}{E_0} = \exp(-2 p_0 t) \cdot \left[\frac{\frac{p_0 / \varepsilon_b}{\sigma_0 / \varepsilon_a} \mathrm{X}_0 - 1}{\frac{p_0 / \varepsilon_b}{\sigma_0 / \varepsilon_a} \mathrm{X}_0 + 1}\right] \tag{C-6}$$

Similarly, from equations 3-34 through 3-37:

$$\Rightarrow \quad \frac{D_{-1}}{E_{-1}} = \exp(-2p_{-1}t)\cdot\left[\frac{\frac{p_{-1}/\varepsilon_b}{\sigma_{-1}/\varepsilon_a}\mathrm{X}_{-1}-1}{\frac{p_{-1}/\varepsilon_b}{\sigma_{-1}/\varepsilon_a}\mathrm{X}_{-1}+1}\right] \tag{C-7}$$

Rearrange equations 3-38 through 3-39 as follow:

$$I_0\left(p_0\cdot a\right)\left[D_0+E_0\right] = -I_{-1}\left(p_{-1}\cdot a\right)\left[D_{-1}-E_{-1}\right] \tag{C-8}$$

$$I_1\left(p_0\cdot a\right)\left[D_0-E_0\right] = -I_0\left(p_{-1}\cdot a\right)\left[D_{-1}+E_{-1}\right] \tag{C-9}$$

Equation C-8 divided by C-9:

$$\frac{I_0\left(p_0\cdot a\right)\cdot I_0\left(p_{-1}\cdot a\right)}{I_1\left(p_0\cdot a\right)\cdot I_1\left(p_{-1}\cdot a\right)} = \left(\frac{1-\frac{D_0}{E_0}}{1+\frac{D_0}{E_0}}\right)\left(\frac{1-\frac{D_{-1}}{E_{-1}}}{1+\frac{D_{-1}}{E_{-1}}}\right) \tag{C-10}$$

Substitute equation C-6 into C-10 and use trigonometric formula [26] to manipulate:

$$\frac{1-\frac{D_0}{E_0}}{1+\frac{D_0}{E_0}} = \frac{1-\exp(-2p_0t)\cdot\left[\frac{\frac{p_0/\varepsilon_b}{\sigma_0/\varepsilon_a}\mathrm{X}_0-1}{\frac{p_0/\varepsilon_b}{\sigma_0/\varepsilon_a}\mathrm{X}_0+1}\right]}{1+\exp(-2p_0t)\cdot\left[\frac{\frac{p_0/\varepsilon_b}{\sigma_0/\varepsilon_a}\mathrm{X}_0-1}{\frac{p_0/\varepsilon_b}{\sigma_0/\varepsilon_a}\mathrm{X}_0+1}\right]}$$

$$= \frac{\left[\frac{p_0/\varepsilon_b}{\sigma_0/\varepsilon_a}\mathrm{X}_0+1\right]-\exp(-2p_0t)\cdot\left[\frac{p_0/\varepsilon_b}{\sigma_0/\varepsilon_a}\mathrm{X}_0-1\right]}{\left[\frac{p_0/\varepsilon_b}{\sigma_0/\varepsilon_a}\mathrm{X}_0+1\right]+\exp(-2p_0t)\cdot\left[\frac{p_0/\varepsilon_b}{\sigma_0/\varepsilon_a}\mathrm{X}_0-1\right]}$$

$$= \frac{\frac{p_0/\varepsilon_b}{\sigma_0/\varepsilon_a}\mathrm{X}_0\left[1-\exp(-2p_0t)\right]+\left[1+\exp(-2p_0t)\right]}{\frac{p_0/\varepsilon_b}{\sigma_0/\varepsilon_a}\mathrm{X}_0\left[1+\exp(-2p_0t)\right]+\left[1-\exp(-2p_0t)\right]}$$

$$= \frac{\frac{p_0/\varepsilon_b}{\sigma_0/\varepsilon_a}\mathrm{X}_0\left[\exp(p_0t)-\exp(-p_0t)\right]+\left[\exp(p_0t)+\exp(-p_0t)\right]}{\frac{p_0/\varepsilon_b}{\sigma_0/\varepsilon_a}\mathrm{X}_0\left[\exp(p_0t)+\exp(-p_0t)\right]+\left[\exp(p_0t)-\exp(-p_0t)\right]}$$

$$= \frac{\frac{p_0/\varepsilon_b}{\sigma_0/\varepsilon_a}\mathrm{X}_0\cdot\tanh\left(p_0t\right)+1}{\frac{p_0/\varepsilon_b}{\sigma_0/\varepsilon_a}\mathrm{X}_0+\tanh\left(p_0t\right)}$$

$$= \frac{1}{\tanh\left[p_0t+\tanh^{-1}\left(\frac{p_0/\varepsilon_b}{\sigma_0/\varepsilon_a}\mathrm{X}_0\right)\right]}$$

$$= \frac{1}{\tanh\left\{\tanh^{-1}\left\{\frac{p_0/\varepsilon_b}{\sigma_0/\varepsilon_a}\tan\left[\sigma_0\cdot d+\tanh^{-1}\left(\frac{\sigma_0/\varepsilon_a}{q_0/\varepsilon_d}\right)\right]\right\}+p_0\cdot t\right\}} = \Phi_0 \qquad \text{(C-11)}$$

Similarly, substitute equation C-7 into C-10:

$$\frac{1-\frac{D_{-1}}{E_{-1}}}{1+\frac{D_{-1}}{E_{-1}}} = \frac{1}{\tanh\left\{\tanh^{-1}\left\{\frac{p_{-1}/\varepsilon_b}{\sigma_{-1}/\varepsilon_a}\tan\left[\sigma_{-1}\cdot d+\tanh^{-1}\left(\frac{\sigma_{-1}/\varepsilon_a}{q_{-1}/\varepsilon_d}\right)\right]\right\}+p_{-1}\cdot t\right\}} = \Phi_{-1} \qquad \text{(C-12)}$$

Combine equations C-11 and C-12:

$$\Phi_i = \frac{1}{\tanh\left\{\tanh^{-1}\left\{\frac{p_i/\varepsilon_b}{\sigma_i/\varepsilon_a}\tan\left[\sigma_i\cdot d+\tanh^{-1}\left(\frac{\sigma_i/\varepsilon_a}{q_i/\varepsilon_d}\right)\right]\right\}+p_i\cdot t\right\}} \qquad \text{(C-13)}$$

It is customary to specify the refraction index of each layer (n_j) in these multi-layer structures. As a consequence, the medium permittivity ε_j in equation C-13 is replaced by $\varepsilon_0 \, n_j^{\,2}$, where ε_0 is the vacuum permittivity.

$$\Phi_i = \frac{-1}{\tanh\left\{\tanh^{-1}\left\{\frac{p_i}{\sigma_i}\frac{n_a^2}{n_b^2}\tan\left[\sigma_i \cdot d + \tanh^{-1}\left(\frac{\sigma_i}{q_i}\frac{n_d^2}{n_a^2}\right)\right]\right\} + p_i \cdot t\right\}} \tag{C-14}$$

Substitute equations C-11, C-12 and C-14 into C-10:

$$\frac{I_0\left(p_0 \cdot a\right) \cdot I_0\left(p_{-1} \cdot a\right)}{I_1\left(p_0 \cdot a\right) \cdot I_1\left(p_{-1} \cdot a\right)} = \left(\frac{1 - \frac{D_0}{E_0}}{1 + \frac{D_0}{E_0}}\right)\left(\frac{1 - \frac{D_{-1}}{E_{-1}}}{1 + \frac{D_{-1}}{E_{-1}}}\right) = \Phi_0 \cdot \Phi_{-1}$$

Thus, equations 3-40 and 3-41 Q.E.D.

APPENDIX D
EIGENMODE EQUATION FOR PLANAR WAVEGUIDES IN TM MODE

From equation 5-1 through 5-11 with boundary conditions, we obtain the following linear homogeneous matrix form:

$$\begin{bmatrix} 1 & -\cos(\sigma_0 \cdot d) & -\sin(\sigma_0 \cdot d) & 0 & 0 & 0 \\ \frac{q_0}{n_d^2} & -\frac{\sigma_0}{n_a^2}\sin(\sigma_0 \cdot d) & \frac{\sigma_0}{n_a^2}\cos(\sigma_0 \cdot d) & 0 & 0 & 0 \\ 0 & 1 & 0 & -\exp(p_0 \cdot t) & -\exp(-p_0 \cdot t) & 0 \\ 0 & 0 & \frac{\sigma_0}{n_a^2} & -\frac{p_0}{n_b^2}\exp(p_0 \cdot t) & \frac{p_0}{n_b^2}\exp(-p_0 \cdot t) & 0 \\ 0 & 0 & 0 & 1 & 1 & -1 \\ 0 & 0 & 0 & \frac{p_0}{n_b^2} & -\frac{p_0}{n_b^2} & -\frac{qc}{n_c^2} \end{bmatrix} \begin{bmatrix} A_0 \\ B_0 \\ C_0 \\ D_0 \\ E_0 \\ F_0 \end{bmatrix} = [C][X] = 0 \tag{D-1}$$

In equation D-1, $[X]$ is the magnetic field amplitude matrix. To have a non-trivial solution for the linear homogeneous matrix equation D-1, the determinant of the coefficient matrix $[C]_{6\times6}$ needs to be zero:

$$\begin{vmatrix} 1 & -\cos(\sigma_0 \cdot d) & -\sin(\sigma_0 \cdot d) & 0 & 0 & 0 \\ \frac{q_0}{n_d^2} & -\frac{\sigma_0}{n_a^2}\sin(\sigma_0 \cdot d) & \frac{\sigma_0}{n_a^2}\cos(\sigma_0 \cdot d) & 0 & 0 & 0 \\ 0 & 1 & 0 & -\exp(p_0 \cdot t) & -\exp(-p_0 \cdot t) & 0 \\ 0 & 0 & \frac{\sigma_0}{n_a^2} & -\frac{p_0}{n_b^2}\exp(p_0 \cdot t) & \frac{p_0}{n_b^2}\exp(-p_0 \cdot t) & 0 \\ 0 & 0 & 0 & 1 & 1 & -1 \\ 0 & 0 & 0 & \frac{p_0}{n_b^2} & -\frac{p_0}{n_b^2} & -\frac{qc_0}{n_c^2} \end{vmatrix} = 0 \tag{D-2}$$

APPENDIX E

EIGENMODE EQUATION FOR FIRST-ORDER DFB WAVEGUIDES IN TM MODE

From equation 5-1 through 5-11 with boundary conditions, we obtain a linear homogeneous matrix form. To have a non-trivial solution for the linear homogeneous matrix equation, the determinant of the coefficient matrix $[C]_{12\times 12}$ needs to be zero:

$$\begin{vmatrix}
1 & -\cos(\sigma_0\cdot d) & -\sin(\sigma_0\cdot d) & 0 & 0 & 0 & 0 & 0 & 0 & 0 & 0 & 0 \\
\frac{q_0}{\varepsilon_d} & -\frac{\sigma_0}{\varepsilon_a}\sin(\sigma_0\cdot d) & \frac{\sigma_0}{\varepsilon_a}\cos(\sigma_0\cdot d) & 0 & 0 & 0 & 0 & 0 & 0 & 0 & 0 & 0 \\
0 & 1 & 0 & -\exp(p_0\cdot t) & -\exp(-p_0\cdot t) & 0 & 0 & 0 & 0 & 0 & 0 & 0 \\
0 & 0 & \frac{\sigma_0}{\varepsilon_a} & -\frac{p_0}{\varepsilon_b}\exp(p_0\cdot t) & \frac{p_0}{\varepsilon_b}\exp(-p_0\cdot t) & 0 & 0 & 0 & 0 & 0 & 0 & 0 \\
0 & 0 & 0 & I_0(p_0a) & I_0(p_0a) & -I_0(qc_0\cdot a) & 0 & 0 & 0 & I_{-1}(p_{-1}a) & -I_{-1}(p_{-1}a) & -I_{-1}(qc_{-1}\cdot a) \\
0 & 0 & 0 & p_0'\cdot I_0(p_0a) & -p_0'\cdot I_0(p_0a) & -qc_0'\cdot I_0(qc_0\cdot a) & 0 & 0 & 0 & p_{-1}'\cdot I_{-1}(p_{-1}a) & p_{-1}'\cdot I_{-1}(p_{-1}a) & -qc_0'\cdot I_{-1}(qc_{-1}\cdot a) \\
0 & 0 & 0 & 0 & 0 & 0 & 1 & -\cos(\sigma_{-1}\cdot d) & -\sin(\sigma_{-1}\cdot d) & 0 & 0 & 0 \\
0 & 0 & 0 & 0 & 0 & 0 & \frac{q_{-1}}{\varepsilon_d} & -\frac{\sigma_{-1}}{\varepsilon_a}\sin(\sigma_{-1}\cdot d) & \frac{\sigma_{-1}}{\varepsilon_a}\cos(\sigma_{-1}\cdot d) & 0 & 0 & 0 \\
0 & 0 & 0 & 0 & 0 & 0 & 0 & 1 & 0 & -\exp(p_{-1}\cdot t) & -\exp(-p_{-1}\cdot t) & 0 \\
0 & 0 & 0 & 0 & 0 & 0 & 0 & 0 & \frac{\sigma_{-1}}{\varepsilon_a} & -\frac{p_{-1}}{\varepsilon_b}\exp(p_{-1}\cdot t) & \frac{p_{-1}}{\varepsilon_b}\exp(-p_{-1}\cdot t) & 0 \\
0 & 0 & 0 & I_1(p_0a) & -I_1(p_0a) & -I_1(qc_0\cdot a) & 0 & 0 & 0 & I_0(p_{-1}a) & I_0(p_{-1}a) & -I_0(qc_{-1}\cdot a) \\
0 & 0 & 0 & p_0'\cdot I_1(p_0a) & p_0'\cdot I_1(p_0a) & -qc_0'\cdot I_1(qc_0\cdot a) & 0 & 0 & 0 & p_{-1}'\cdot I_0(p_{-1}a) & -p_{-1}'\cdot I_0(p_{-1}a) & -qc_{-1}'\cdot I_0(qc_{-1}\cdot a)
\end{vmatrix} = 0$$

Where $p_0' = \frac{p_0}{\varepsilon_b}$, $p_{-1}' = \frac{p_{-1}}{\varepsilon_b}$, $qc_0' = \frac{qc_0'}{\varepsilon_c}$, $qc_{-1}' = \frac{qc_{-1}'}{\varepsilon_c}$, $\varepsilon_a = \varepsilon_0 n_a^2$, $\varepsilon_b = \varepsilon_0 n_b^2$, $\varepsilon_d = \varepsilon_0 \cdot n_d^2$, $\varepsilon_c = \varepsilon_0 \cdot n_c^2$.

APPENDIX F
COUPLING-COEFFICIENT SENSITIVIY TO GEOMETRIC PARAMETERS FOR WAVEGUIDES IN TM MODE

Coupling-coefficient sensitivity $\left(S_p\right)$ to geometric parameters (P) can be defined according to the slopes of curves plotted in the figures of coupling coefficient versus parameters:

$$S_p \propto \text{Slope} = \frac{\Delta\kappa_p}{\Delta P} \tag{F-1}$$

Table F-1. Coupling-coefficient sensitivity to geometric parameters

Parameter / Model	Groove depth (a)	Buffer thickness (t)	Active thickness (d)
	t=0.3, d=0.1 a<0.13 μm	ka=0.2,d=0.1 t<0.3 μm	ka=0.2,t=0.3 d<0.3 μm
TM-1 (ModB)	34	-5	-3.3
TM-1 (ModA)	22	-5	-3.1
TE-1, (ModA)	22	-8	-2.1
TE-1 (ModB)	19	-8	-1.9

All ratios in Table F-1 are in 10^6 [cm^{-2}]. The curves of coupling coefficient versus groove depth have the largest slopes than those of coupling coefficient versus layer thickness. Thus, the groove depth affects the coupling coefficient more than the layer thickness.

APPENDIX G

FIELD INTERACTION AT DIELECTRIC-METAL INTERFACE FOR PLANAR WAVEGUIDES IN TE AND TM MODES

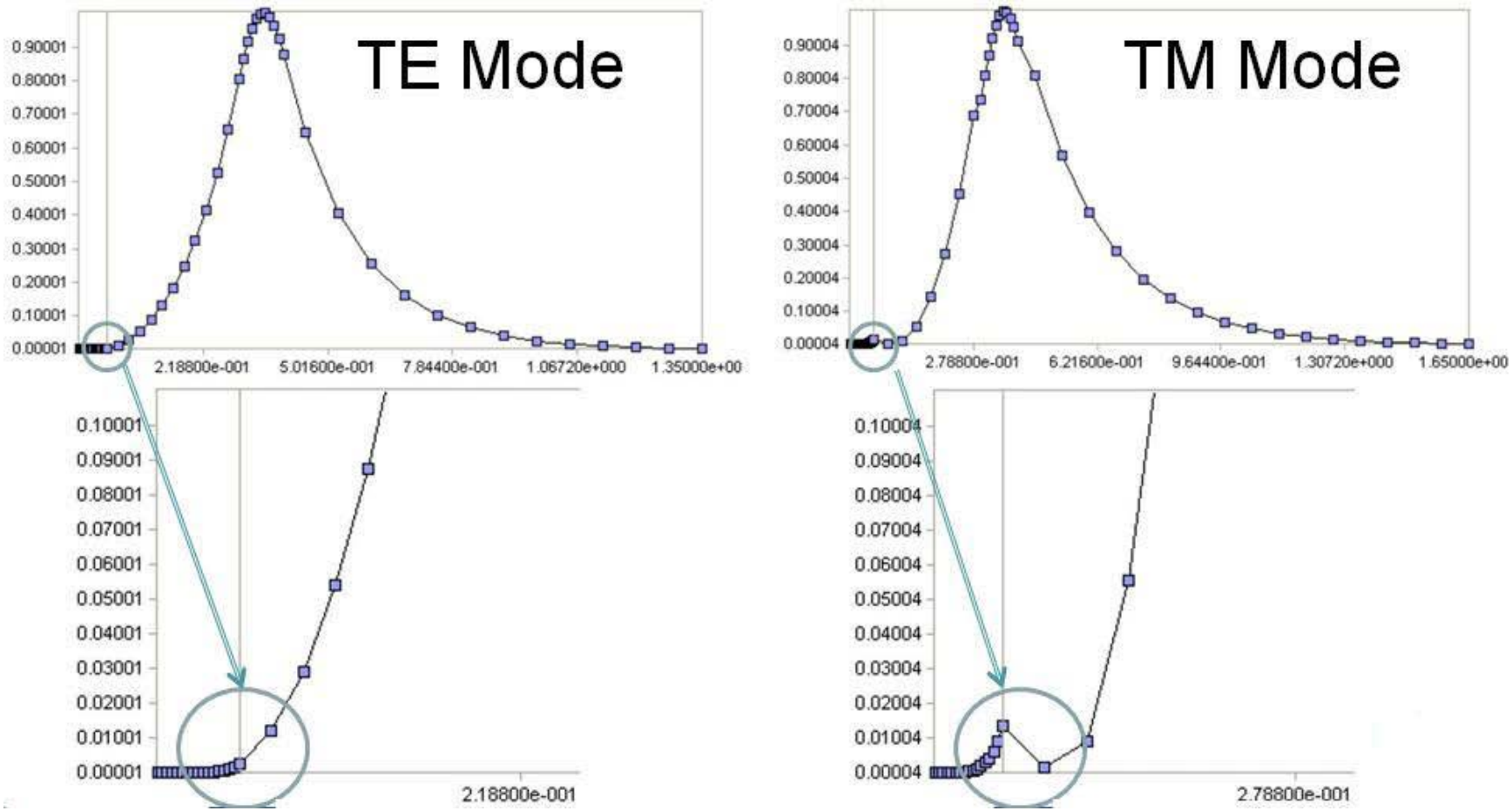

Figure G-1. Field interaction at the dielectric-metal interface in TE and TM modes. TM mode has larger interaction.

LIST OF REFERENCES

[1] R. N. Hall et al," Coherent light emission from GaAs junctions," *Phys. Rev. Lett.* vol. 9, pp. 366-368, 1962.

[2] R. N. Hall, "Injection lasers," *IEEE J. of Quantum Electron.*, vol. 23, no. 6, pp. 674-678, 1987.

[3] J. Faist et al, "Quantum cascade laser," *Science*, vol. 264, no. 5158, pp. 553-556, 1994.

[4] M. Pushkarsky,et al.," Sub-parts-per-billion level detection of using room-temperature quantum cascade lasers," *Proc. Natl. Acad. Sci. U.S.A.*, vol. 103, pp. 19630-19634, 2006.

[5] A. Lyakh et al., "Substrate-emitting distributed feedback quantum cascade laser," *App. Phys. Lett.*, 91, 181116, 2007.

[6] A. Lyakh, *High-power Bipolar and Unipolar Quantum Cascade Lasers*, Ph.D. Dissertation, University of Florida, 2007.

[7] D. Marcuse, *Theory of Dielectric Optical waveguides*. Second Edition. San Diego, CA: Academic Press, 1991.

[8] S. M. Sze, *Physics of Semiconductor Devices*. Second Edition. New York: John Wiley & Sons, 1981.

[9] B. G. Streetman and S. Banerjee, *Solid State Electronics Devices*. Upper Saddle River, NJ: Prentice Hall, 2000.

[10] M. Bass, et al. *Handbook of Optics*. New York: McGraw-Hill, 1995.

[11] K. Okamoto, *Fundamentals of Optical Waveguides*. Second Edition. San Diego, CA: Elsevier, 2006.

[12] N. Yu, "Near-field Imaging of quantum cascade laser Transverse Modes," *Optics Express*. vol. 15, no. 20, pp. 13227-13235, 2007.

[13] J. J. Wilson and J. Hawkes, *Optoelectronics: An Introduction*. Third Edition. New York: Prentice Hall, 1989.

[14] N. Nishihara et al., *Optical Integrated Circuits*. New York: McGraw-Hill, 1982.

[15] R. J. Noll and S. H. Macomber, "Analysis of grating surface emitting lasers," IEEE *J. of Quantum Electron.*, vol. 26, no. 3, pp.456-466, 1990.

[16] D. L. Lee, *Electromagnetic principles of Integrated Optics*. New York: John Wiley & Sons.1986.

[17] S.Fathololoumi et al.," Beam pattern investigation of terahertz quantum cascade lasers," *Progress In Electromagnetics Research Symposium*, Hangzhou, China, pp. 401-404, 2008.

[18] Y. C. Shen, "Detection and identification of explosives using terahertz pulsed spectroscopic imaging, *Appl. Phys. Lett*., vol. 86, 241116, 2005.

[19] K. Kawase et al., "Non-destructive terahertz pulsed imaging of illicit drugs using spectral fingerprints," *Optics. Express*, 11, 2549-2554, 2003.

[20] K. Iizuka, Elements of Photonics: for Fiber and Integrated Optics. New York: John Wiley & Sons, 2002.

[21] C. K. Kao, *Optical Fiber Systems: Technology, Design, and Application*. New York: McGraw-Hill, 1982.

[22] G. Gaussorgues, *Infrared Thermograph*. London, Great Britain: Chapman & Hall,1994.

[23] H. J. Luo, *Shiny Contact Distributed Feedback Semiconductor Lasers*. Ph.D. Dissertation, University of Florida, 1993.

[24] D. M. Bloom, *Linear Algebra and Geometry*. New York: Cambridge University Press, 1979.

[25] J. G. Broida and S. G. Williamson, *A comprehensive Introduction to Linear Algebra*. New York: Addison-Wesley, 1989.

[26] R. Barnett, *Analytic Trigonometry with Applications*. Third Edition. Belmont, CA: Wadsworth, 1984.

[27] H. Yonezu et al., "A $GaAs - Al_xGa_{1-x}As$ double heterostructure planar stripe laser," *Japanese J. of Appl. Phys*. vol. 12, pp1585-1587, 1973.

[28] L. A. Coldren and S. W. Corzine, *Diode Lasers and Photonics Integrated Circuits*. New York: John Wiley & Sons, 1995.

[29] W. Streifer et al., "Coupling coefficients for distributed feedbacks single- and double-heterostructure diode lasers," *IEEE J. Quantum Electron*., vol. 11, pp. 867-873, 1975.

[30] P. Correc, "Coupling coefficients for trapezoidal gratings," *IEEE J. Quantum Electron*., vol. 24, pp. 8-10, 1988.

[31] Y. Shani et al., " $Pb_{1-x}Sn_xSe / Pb_{1-x-y}Eu_ySn_xSe$ Corrugated diode laser," *IEEE J. Quantum Electron*., vol. 25, pp. 1828-1844, 1989.

[32] S. S. Li, *Semiconductor Physical Electronics*. New York: Plenum Press, 1993.

[33] C. Kittel, *Introduction to Solid State Physics*. Eighth Edition. Hoboken, NJ : John Wiley & Sons, 2005.

[34] A. Yariv. *Optical Electronics*. Third Edition. Orlando, FL: Holt, Rinehart and Winston, 1991.

[35] H. H. Yee, "Novel Self-consistent method for Determining optical coupling coefficients and grating losses of Distributed Bragg Reflector Lasers, *Opt. eng*. vol. 41, no. 5, pp1077-1083, 2002.

[36] D. Hanselman and B. Littlefield, "*Mastering MATLAB 6®: A Comprehensive Tutorial and Reference*. Upper Saddle River, NJ: Prentice Hall, 2007.

[37] R. J. Schilling and S. L. Harris, *Applied Numerical Methods for engineers Using MATLAB® and C*. Pacific Groove, CA: Brooks/Cole, 1999.

[38] F. T. Ulaby, *Fundamentals of Applied Electromagnetics*. Upper Saddle River, NJ: Prentice Hall, 1997.

[39] J D. Jackson, *Classical Electrodynamics*. Third Edition. New York: John Wiley & Sons, 1999.

[40] H. Kogelnik and C. V. Shank, "Coupled-wave theory of distributed feedback lasers," *J. Appli. Phy*., vol. 43, no. 4, pp.2327-2335, 1972.

[41] R. K. Wangsness, *Electromagnetic Fields*. New York: John Wiley & Sons. 1986.

BIOGRAPHICAL SKETCH

Meng-Mu Shih was born in Taiwan. He received Bachelor of Science (B.S.) and Master of Science (M.S.) degrees in mechanical engineering from National Taiwan University (NTU). He received two M.S. degrees: one in electrical engineering from the College of Engineering, and the other in management from the Warrington College of Business Administration, both at the University of Florida (UF). Later, he joined the Photonics Research Laboratory under Professor Zory, for working toward his Doctor of Philosophy (Ph. D.) degree. Mr. Shih has been partly funded by the Defense Advanced Research Projects Agency (DARPA) for quantum cascade lasers (QCLs). He has been involved in the modeling, design, physics, characterization and measurement of semiconductor lasers and light-emitting devices. He interests in areas including system modeling, product and design methodology, nanotechnology, electromagnetism, semiconductor devices, optics, photonics, optoelectronics, and optical distributed-feedback waveguides with corrugated metal gratings.